OPTICAL INTERACTIONS BETWEEN SINGLE EMITTERS AND NANOSTRUCTURES

by

Eyal Shafran

A dissertation submitted to the faculty of
The University of Utah
in partial fulfillment of the requirements for the degree of

Doctor of Philosophy

in

Physics

Department of Physics and Astronomy

The University of Utah

December 2011

The University of Utah Graduate School

STATEMENT OF DISSERTATION APPROVAL

The dissertation of **Eyal Shafran**

has been approved by the following supervisory committee members:

Jordan M. Gerton	, Chair	**07/13/2011** Date Approved
Mikhail Raikh	, Member	**07/13/2011** Date Approved
Andrey Rogachev	, Member	**07/13/2011** Date Approved
Michael Vershinin	, Member	**07/13/2011** Date Approved
Ling Zang	, Member	Date Approved

and by **David Kieda**, Chair of the Department of **Physics and Astronomy**

and by Charles A. Wight, Dean of The Graduate School.

ABSTRACT

This work studies the optical interactions between single emitters, mainly quantum dots (QD) and a sharp tip. The fluorescence intensity, quantum yield and angular emission of a single emitter can be strongly modified by near-field coupling with the sharp tip. Gold, silicon, and carbon nanotube (CNT) tips are employed in order to understand the physical mechanisms which are responsible for the various near-field effects. Each of these materials carries different properties, which modify the optical properties of QDs in unique ways.

In order to maximize the amount of information accessible by our near-field scanning microscope (NSOM), a novel near-field tomography technique is implemented. This technique facilitates the revelation of a number of interesting three-dimensional near-field features and is instrumental in the study of the different near-field mechanisms. The flexibility in the data acquisition (DAC) technique allows us to study the influence of fluorescence intermittency (blinking) in QDs on the near-field coupling with the probes. The fluorescence emission from states with high quantum yield is more sensitive to quenching due to energy transfer, while in the low-yield states, near-field signal enhancement is more pronounced. The emission fluctuations of the QDs are progressively suppressed upon approach of a gold tip due to strong near-field coupling of gold tips to the QDs. Moreover, the angular emission of QDs in proximity to gold tips is very sensitive to the exact tip-QD position but does not depend on the intrinsic quantum yield of the QD. Energy transfer dominates the interactions of single CNTs with the QDs. Precision measurements of the energy transfer exhibit unique features as a result of the one-dimensional nature of CNTs. In particular, the energy transfer efficiency saturates at $\sim$96% for all CNTs tried, even though the CNTs are expected to have a distribution of chiralities.

To my family - Jen and Ethan

CONTENTS

LIST OF FIGURES

LIST OF TABLES

ACKNOWLEDGMENTS

This work could not have been done without the help and support of many people. First of all, I would like to thank Jordan Gerton for his guidance, patience, and his persistently positive attitude. I realize that I am not always easy to work with, but Jordan has been able to get the best out of me by somehow tolerating my stubbornness and Israeli demeanor.

I would also like to thank the various lab members I got to work with over the years. Analia Dall'Asén, Anil Ghimire, Ben Martin, Carl Ebeling, Cassandra Hammons, Charles McGuire, Chun Mu, Jason Ho and Jessica Johnston - you have all made my life harder, but better. Seriously, thanks for making the lab a fun and happy working environment and for your feedback and insight into our research. A special thanks to Ben Mangum for taking me under his wing when I joined the lab. Our arguments about science, religion, and all of humanity's problems were my favorite part of every day. Much of this work in this dissertation was equally contributed by Ben.

Nobody can succeed without a loving and supportive home environment. Thanks to my parents, who initially created this for me and continue to show interest in my work and give a lot of support even from a great distance. Thanks to my lovely wife Jen who pretends to listen and care about my research and to my friend Idan who doesn't even pretend. There are too many people to name who have been supportive and who have had confidence in my abilities, even when I didn't, thanks for everything. Finally, I would like to thank "Blueberry" for giving me a very real deadline for finishing my dissertation.

CHAPTER 1

INTRODUCTION

As objects get smaller, microscopic behavior becomes more significant and quantum mechanical effects become more pronounced and dominant. Our ability to detect nanometer phenomena has increased dramatically with the invention of techniques such as electron microscopy, scanning probe microscopy (SPM), near-field scanning optical microscopy (NSOM), optical nanoscopy and many more. Today's technology allows us to fabricate and synthesize complex objects with nanometer precision that therefore possess different electronic, mechanical and optical properties than objects on the macroscale. As our technological abilities improve, so does our understanding of nanoscience, and new novel nanotechnology applications have already emerged with significant contributions to medicine, electronics, photovoltaics and microscopy [1–6].

Of particular interest is the light-matter interaction on the nanoscale. The optical properties of structures with much smaller dimensions than the wavelength of incident light (i.e., nanostructures) can be very different from bulk characteristics. Most importantly, these properties vary based on the exact shape, size and composition of the nanostructure, which allows the optical properties to be tuned by carefully engineering the structure. Furthermore, the interaction of nanostructures with additional materials, such as other nanostructures, fluorescence molecules and analyte solutions, can further change the interaction with light. For example, metallic nanoparticles predominantly scatter light at different wavelengths when they are isolated, aggregated or surrounded by an analyte. These unique scattering properties have already made an impact in biosensing applications, such as immunoassay detection and even the home pregnancy test [7]. Other applications of metallic nanoparticles in cutting-edge fields include improved photovoltaic devices [8] and the integration into nanoscale

electronics [9]. The ability to precisely engineer nanoshells - dielectric core metallic shell particles - has enabled the fine tuning of the absorption resonance of these particles to the infrared and might lead to a breakthrough in photothermal cancer therapy treatments and diagnostics [10].

In semiconductor nanoparticles, the spatial confinement of the charge carriers results in the modification of the energy levels of the nanocrystal. This quantum confinement effect leads to optical properties which can be tuned by the size of the nanocrystal [11]. If the quantum confinement occurs in all three spatial dimensions, the nanocrystal is referred to as a quantum dot (QD). Due to their broad absorption spectra, narrow emission band, high quantum yield and high photostability, semiconductor nanocrystals are desirable for light-emitting devices [12] and biological imaging applications [13]. They are also useful to various other applications including photovoltaics [14–16], thin layer field-effect transistors (FET) [6,17] and quantum dot lasers [18].

The capability to confine light to a subdiffraction volume by nanostructures with sharp edges such as lightning rods [19,20], optical antenna [21–23], and roughened surfaces [24–26] is particularly appealing for spectroscopic and fluorescence applications. When a molecule is placed in proximity to a nanostructure, near-field effects become prominent and the properties of the "coupled" system need to be considered. This allows the manipulation of light by means of enhanced excitation and emission [27,28], modified spectra [29], and control of the angular emission [23, 30]. For example, the Raman cross-section of molecules can be enhanced by many orders of magnitude near metal surfaces, which enables single molecule Raman spectroscopy measurements via surface enhanced Raman spectroscopy (SERS) [31] and tip-enhanced Raman spectroscopy (TERS) [32]. The confined fields near a sharp dielectric or metallic tip can also be used for high contrast optical microscopy with resolution which far surpasses conventional optical microscopy [33–36].

1.1 The diffraction limit

In conventional microscopy light is focused by a microscope objective lens onto/from a sample. The resolving power of an optical microscope depends on the ability of the lens to focus light to a tight spot. Due to the wave nature of light, the light diffracts as it encounters the lens, and as a result the light cannot be focused to an infinitely tight spot. This means that when an isolated, infinitesimally small object is imaged, the image will reflect the size of the laser spot and not the object. This phenomenon is often referred to as the *diffraction limit*.

The *Abbe limit* states that for light with wavelength λ, traveling in a medium with refractive index n, and going through a lens with a collection angle of θ, the smallest spot size is denoted by

$$d = \frac{\lambda}{2n \sin\theta} \tag{1.1}$$

The denominator can be defined by the numerical aperture of the lens NA=$n \sin\theta$. The NA of modern microscope objectives can be as high as NA=1.65; therefore, conventional optical microscopy cannot distinguish details in the specimen smaller than $\sim \lambda/2$. This optical phenomenon is a major hindrance in the study of nanoscience.

1.2 Heisenberg's uncertainty

One way the obtain better resolution than the diffraction limit is by using near-field optics. The improved resolution due to the detection of near-field radiation can be understood by examining the relationship between the diffraction limit and Heisenberg's uncertainty principle. A thorough discussion on the Heisenberg's uncertainty principle in near-field optics can be found in Ref. [37, 38]. The optical representation of the uncertainty principle can be written as follows [37]

$$\Delta x \Delta p_x \geq h \tag{1.2}$$

where Δx and Δp_x are the uncertainties in the position and momentum of a particle in one dimension, respectively, and h is the Planck constant. Full knowledge of the position of a particle and its exact momentum is forbidden by the uncertainty principle. It is clear from Eq. 1.2 that a better position accuracy can be obtained on

the expense of a large uncertainty in the momentum. Using the de Broglie relation $\mathbf{p} = \hbar\mathbf{k}$, where $\mathbf{k}$ is the wavevector of the particle, Eq. 1.2 can be rewritten as

$$\Delta x \Delta k_x \geq 2\pi. \tag{1.3}$$

In theory, if there was a way to extend the integrated wavevectors to infinity, there would be no limitation on the spatial resolution. However, in a classical microscope, only the radiating (i.e., far-field) components are detected, which possess a limit on the spread of wavevectors Δk_x collected. If the light is collected or focused by a microscope objective lens with numerical aperture of NA, only the spatial frequencies between $|k_x| = 0$ and $|k_x| = n \sin\theta(\omega/c)$, where ω is the angular frequency and c is the velocity of the photons, will be collected by the lens. If we insert the expression for the spread of wavevectors $\Delta k_x = 2n \sin\theta(\omega/c)$ into Eq. 1.3 and use the dispersion relation for photons $\omega/c = (2\pi/\lambda)$, we recover a similar expression to the diffraction limit

$$\Delta x \geq \frac{\lambda}{2n \sin\theta}. \tag{1.4}$$

Even if the lens was able to collect over all angles, i.e., $\sin\theta = 1$ and $k_{max} = n\omega/c$, the maximum collected wavevector is still limited by the fact that only the propagating far-field components of the radiation reach the objective lens. Therefore, the spatial resolution is limited by the inability to detect the nonradiating components of the light.

The detection of evanescent components (i.e., waves with an exponentially decaying intensity) can achieve better resolution than the diffraction limit without violating the uncertainty principle. Let us consider light which has wavevector components along the x and z directions. We find that

$$k_x^2 + k_z^2 = (\omega/c)^2 \tag{1.5}$$

If we consider the light along the z-direction to have an imaginary wavevector k_z (i.e., $k_z = i|k_z|$), the wavevector along the x-axis takes the following form: $k_x^2 = (\omega/c)^2 - k_z^2 = (\omega/c)^2 + |k_z|^2$. Therefore, the range of collected wavevectors is extended, and thus, the spatial resolution in the x-axis is improved in comparison with the

diffraction limit. If we define k_z as imaginary however, the propagation term in the z-direction becomes $e^{ik_z z} = e^{-|k_z|z}$ and the radiation decays exponentially, as expected from evanescent light. The problem then becomes the ability to detect such strongly localized decaying light. To do so, one must bring an object with subwavelength features into the near-field radiation zone as discussed in the next section. However, such close "invasion" leads to the coupling of the object with the sample, which can result in undesired or misunderstood outcomes. This complicates matters but also opens up the possibility to control and manipulate light by careful design and understanding of near-field phenomena.

1.3 Detecting evanescent waves

Generally speaking, near-field components are accessible experimentally by either having a near-field illumination and/or near-field detection scheme. In a near-field illumination scheme, such as an apertureless NSOM, a scatterer smaller than the wavelength of light is brought into a subwavelength separation distance from a sample. In such a case, the evanescent or near-field components of the scattered light interact with the sample, rather than only the propagating or far-field components. By scanning a sample relative to a scatterer and collecting the light emitted by or transmitted through the sample, an image could thus be built up that would not be subject to the limits imposed by diffraction of the far-field components. Figure 1.1 illustrates the implementation of apertureless NSOM.

Another realization of near-field illumination can be achieved by aperture type NSOM. In this scheme, the scattering particle is replaced with a subwavelength aperture in a thin metal plate or film. Very close to the aperture, confined optical fields reflect the shape of the aperture itself, rather than the far-field diffraction pattern. The light transmitted through the aperture would excite optical processes (e.g., fluorescence, Rayleigh scattering, Raman scattering, etc.) in a subdiffraction volume, and the resulting optical signal would be collected with a lens (e.g., microscope objective) and finally detected in the far field with a light sensitive detector. Although a subwavelength aperture will transmit merely a fraction of the incident

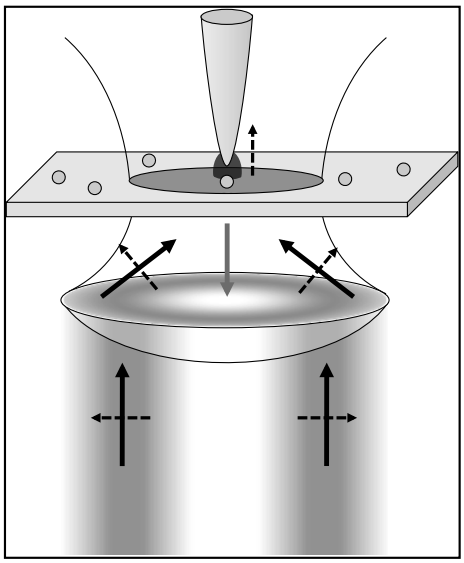

Figure 1.1. Apertureless NSOM. A sharp probe of an atomic force microscope is illuminated with a diffraction limited spot. Upon the right excitation conditions, the excitation light is strongly localized at the apex of the probe. When the probe is brought in proximity to a fluorescent sample, the localized near-field components near the apex of the probe interact with sample. The emitted light from the sample is then collected from below by a microscope objective.

light, only this transmitted light will excite the sample, so background signals are low.

In a near-field detection scheme, the detector must be on a subwavelength distance from the sample. Although possible, this is a much less common approach in near-field microscopy and is described in more detail elsewhere [39].

1.4 Outline

In this work an apertureless NSOM is used to study optical interactions between single emitters and various types of materials. The detected signal from fluorescence samples, mainly semiconductor quantum dots, can be affected by the detection efficiency of the microscope, the coupling of the excitation light to the near-field probe, and finally the coupling of the emitter to the near-field probe. The physical mechanisms, which modify the total measured fluorescence signal, are reviewed in Chapter 2. The experimental details concerning the integration of an atomic force

microscope (AFM) with an optical setup are discussed in Chapter 3. The strength of our measurements lie in our unique data acquisition (DAC) and analysis techniques; therefore, the basic DAC and analysis are also summarized in this chapter.

Chapters 4-7 are a summary of the experimental results. Since near-field microscopy is a relatively new field, new acquisition and detection techniques help reveal new physics. The extension of our detection abilities from 2D images to a complete 3D map of near-field interactions is explained in Chapter 4. This technique has been used in the rest of the projects as well. In Chapter 5, the balance between competing near-field mechanisms, which can result in signal enhancement and/or signal reduction (quenching), is studied by utilizing photoluminescence blinking in semiconductor QDs. By measuring the near-field signal as the QDs undergoes different quantum yield states, we were able to isolate the contribution of enhancement and quenching for various AFM tips materials. Chapter 6 is focused on the energy transfer between isolated QDs and single carbon nanotubes (CNT). Finally, the change in angular emission of QDs in proximity to commercial metal tips is examined in Chapter 7.

1.5 References

[1] S. Tans, A. Verschueren, and C. Dekker, Nature **393**, 49 (1998).

[2] W. L. Barnes, A. Dereux, and T. W. Ebbesen, Nature **424**, 824 (2003).

[3] E. Serrano, G. Rus, and J. Garcia-Martinez, Renewable & Sustainable Energy Reviews **13**, 2373 (2009).

[4] M. Stockman, Physics Today **64**, 39 (2011).

[5] M. Ferrari, Nature Reviews Cancer **5**, 161 (2005).

[6] D. V. Talapin, J.-S. Lee, M. V. Kovalenko, and E. V. Shevchenko, Chemical Reviews **110**, 389 (2010).

[7] T. Endo et al., Analytical Chemistry **78**, 6465 (2006).

[8] H. A. Atwater and A. Polman, Nature Materials **9**, 205 (2010).

[9] E. Ozbay, Science **311**, 189 (2006).

[10] S. Lal, S. E. Clare, and N. J. Halas, Accounts of Chemical Research **41**, 1842 (2008).

[11] D. E. Gomez, M. Califano, and P. Mulvaney, Physical Chemistry Chemical Physics **8**, 4989 (2006).

[12] V. L. Colvin, M. C. Schlamp, and A. P. Alivisatos, Nature **370**, 354 (1994).

[13] I. L. Medintz, H. T. Uyeda, E. R. Goldman, and H. Mattoussi, Nature Materials **4**, 435 (2005).

[14] P. V. Kamat, Journal of Physical Chemistry C **111**, 2834 (2007).

[15] P. V. Kamat, Journal of Physical Chemistry C **112**, 18737 (2008).

[16] R. Schaller, M. Sykora, J. Pietryga, and V. Klimov, Nano Letters **6**, 424 (2006).

[17] D. V. Talapin and C. B. Murray, Science **310**, 86 (2005).

[18] V. I. Klimov et al., Science **290**, 314 (2000).

[19] L. Novotny, Applied Physics Letters **69**, 3806 (1996).

[20] J. L. Bohn, D. J. Nesbitt, and A. Gallagher, Journal of the Optical Society of America A **18**, 2998 (2001).

[21] P. Mhlschlegel, H. J. Eisler, O. J. F. Martin, B. Hecht, and D. W. Pohl, Science **308**, 1607 (2005).

[22] J. N. Farahani, D. W. Pohl, H. J. Eisler, and B. Hecht, Physical Review Letters **95**, 4 (2005).

[23] T. H. Taminiau, F. D. Stefani, F. B. Segerink, and N. F. Van Hulst, Nature Photonics **2**, 234 (2008).

[24] M. Fleischmann, P. J. Hendra, and A. J. McQuillan, Chemical Physics Letters **26**, 163 (1974).

[25] D. L. Jeanmaire and R. P. VanDuyne, Journal of Electroanalytical Chemistry **84**, 1 (1977).

[26] M. G. Albrecht and J. A. Creighton, Journal of the American Chemical Society **99**, 5215 (1977).

[27] P. Anger, P. Bharadwaj, and L. Novotny, Physical Review Letters **96** (2006).

[28] A. Kinkhabwala et al., Nature Photonics **3**, 654 (2009).

[29] M. Ringler, A. Schwemer, M. Wunderlich, and A. Nichtl, Physical Review Letters **100** (2008).

[30] A. G. Curto et al., Science **329**, 930 (2010).

[31] K. Kneipp et al., Physical Review Letters **78**, 1667 (1997).

[32] B. Pettinger, B. Ren, G. Picardi, R. Schuster, and G. Ertl, Physical Review Letters **92** (2004).

[33] H. G. Frey, S. Witt, K. Felderer, and R. Guckenberger, Physical Review Letters **93** (2004).

[34] V. V. Protasenko, A. Gallagher, and D. J. Nesbitt, Optics Communications **233**, 45 (2004).

[35] J. M. Gerton, L. A. Wade, G. A. Lessard, Z. Ma, and S. R. Quake, Physical Review Letters **93** (2004).

[36] Z. Y. Ma, J. M. Gerton, L. A. Wade, and S. R. Quake, Physical Review Letters **97** (2006).

[37] J. M. Vigoureux and D. Courjon, Applied Optics **31**, 3170 (1992).

[38] J. Greffet and R. Carminati, Progress in Surface Science **56**, 133 (1997).

[39] L. Novotny and B. Hecht, *Principles of Nano-Optics*, Cambridge University Press, Cambridge, 2006.

CHAPTER 2

OPTICAL SIGNAL DUE TO NEAR-FIELD INTERACTIONS

A near-field scanning optical microscope combines the principles of optical microscopy and atomic force microscopy. In apertureless NSOM, a diffraction-limited illumination source, usually a focused laser, is used to polarize the tip of the scanning probe. When the probe is brought in the proximity of a sample, the local environment of the sample is perturbed, which results in the modification of the excitation rate and the emission rate of the sample. In general, the near-field component is the result of a competition between tip-induced enhancement of the optical field and various tip-induced suppression mechanisms. This chapter discusses five major issues: material properties of the tip and sample, interaction of the excitation with the tip, interaction of the emission with the tip, system's detection efficiency and the total change to the measured signal. The focus is on the fluorescence samples although near-field microscopy is not limited just to the detection of fluorescence.

The detected signal in our setup is typically the fluorescence emission rate modulated by the collection efficiency of the optical system. Below saturation (i.e., in the linear scattering regime) of the sample, the total detected signal can be written as:

$$S = C(r)\Gamma_{exc}(r)q(r) \tag{2.1}$$

where r is the tip-sample distance, $C(r)$ is the collection efficiency of our system, $\Gamma_{\mathrm{exc}}(r)$ is the excitation rate and $q(r)$ is the quantum yield of the sample. Each of the above parameters can change upon bringing a nanostructure in proximity to the sample.

In Sec. 2.1, some general properties of materials that pertain to optical interactions are reviewed. The discussion covers two types of materials: metals and

dielectrics. Section 2.2 focuses on the interaction of the excitation light with the near-field probe. This interaction generally leads to field enhancement at the apex of the tip as a result of lightning-rod and plasmon effects and results in the modification of the excitation rate $\Gamma_{\text{exc}}(r)$. The emission properties of a single emitter in both homogeneous and inhomogeneous environments are reviewed in Sec. 2.3. In particular, this section focuses on the changes in radiative and non-radiative decay rates of an emitter due to the environment which lead to a change in the emitter's quantum yield $q(r)$. Although the angular emission pattern of a dipole is also related to the properties of an emitter and its environment, this effect is discussed in a separate section since it can change the effective detection efficiency of the system $C(r)$. Finally, the experimentally measured fluorescence signal, as written in Eq. 2.1, is revisited in more details in Sec. 2.5.

This chapter is intended to provide some general theoretical background for the experiments discussed in the remainder of the dissertation. By the end of the chapter, the reader should be familiar with the general considerations that determine the measured fluorescence signal from a single emitter in proximity to a near-field probe. A thorough review of nano-optics and nanoscale optical interactions can be found in Ref. [1]. Several subsections in this chapter follow closely some sections from a recent book chapter we prepared [2].

2.1 Material properties

In order to understand the interaction of light with matter at the nanoscale, we must first understand the properties of materials at different wavelengths. The response of a material to an alternating field can be described by a complex dielectric function (electric permittivity)

$$\epsilon(\omega) = \epsilon'(\omega) + i\epsilon''(\omega) \tag{2.2}$$

The dielectric function strongly depends on the oscillation frequency of the field, ω. For example, metallic materials generally have $\epsilon'(\omega) < 0$ when ω is small and therefore are highly reflective in this regime. In contrast, when ω is large, $\epsilon'(\omega) > 0$ and the metal is mostly transparent. The imaginary part of the dielectric function is

associated with the Ohmic losses in the material, and resistive heating [3]. By using Ohm's law and Maxwell's equations, the complex dielectric function can be denoted by

$$\epsilon(\omega) = \epsilon'(\omega) - i\frac{\sigma}{\epsilon_0 \omega} \tag{2.3}$$

where σ is the AC conductivity of the material and ϵ_0 is the permittivity in vacuum. Therefore, the imaginary part of the dielectric function is related to the AC conductivity of the material.

2.1.1 Metals

Metals are good electric conductors because they have a large density of quasi-free electrons in the conduction band. The Drude-Sommerfield model [1,4,5] approximates these conduction electrons as a free-electron gas and provides an explanation for many observed features such as charge transport and optical measurements in metals. Within this model, it is assumed that the free electron response to an external driving field (e.g., a light field) is the dominant effect and that the contribution of the valence electrons can therefore be neglected. The dielectric function calculated from this model is then

$$\epsilon_{\mathrm{D}}(\omega) = 1 - \frac{\omega_p^2}{\omega^2 + \beta^2} + i\frac{\beta\omega_p^2}{\omega(\omega^2 + \beta^2)}. \tag{2.4}$$

Here $\beta = v_F/l$ is a damping term that arises from scattering of the electrons where v_F is the Fermi velocity and l is the mean free path of the electrons. The plasma frequency is defined by $\omega_p = \sqrt{ne^2/(m_e\epsilon_0)}$ where n is the free-electron density and e and m_e are the electron charge and effective mass, respectively.

The Drude-Sommerfield model successfully describes the dielectric function of metals in the infrared spectrum. At optical frequencies, $\omega >> \beta$, and the Drude-Sommerfield model is reduced to $\epsilon_{\mathrm{D}}(\omega) = 1 - \frac{\omega_p^2}{\omega^2}$. However, at higher energies, the incident light can excite valence electrons into the conduction band; when this occurs, interband transitions become significant and must also be taken into account. For example, in the visible range, most metals exhibit a resonance behavior in the

imaginary part of the dielectric function, which can only be explained by the inclusion of the interband transitions. The interband transitions can be most easily accounted for using a semiclassical model where the electrons bound to the lattice sites (i.e., the lower-energy valence electrons) are considered to be classical oscillators with resonance frequencies given by the quantum-mechanical transition frequencies. An external driving field near these frequencies can promote the valence electrons into the conduction band, where they will then contribute to the electronic and optical response, and thus the dielectric function. The dielectric function due to tightly bound electrons does predict a resonance behavior in ϵ'' [6, 7]. Therefore, the dielectric function of metal is better described by a combination of the Drude-Sommerfield model, which accounts for free-electrons, and an interband term $\epsilon(\omega) = \epsilon_{\mathrm{D}}(\omega) + \epsilon_{\mathrm{IB}}(\omega)$ [1, 8–10].

As the spatial dimensions of a metal become similar to the mean free path of the electrons, scattering of electrons from the particle surface changes the dielectric function due to the increase in damping (i.e., increase in β). For example, the mean free path of gold is $l \sim 38$ nm. Thus, any geometry with dimensions of several tens of nm or smaller will exhibit more damping than bulk gold. For this reason, in the nanoscale regime, the dielectric function is also size dependent. A surface scattering correction term can be analytically calculated for spheres, but for more complex geometries, it is difficult to extract the appropriate damping coefficient [9]. Figure 2.1 compares experimentally measured dielectric function values for gold (solid blue line) taken from Ref. [11] to the the Drude-Sommerfield model (green dotted line). The plasma frequency and the damping coefficient used for calculating the Drude response were $\omega_p = 2.165 \cdot 10^{15}$ Hz and $\beta = 17.64 \cdot 10^{12}$ Hz [12], respectively. As mentioned above, at longer wavelengths, the experimental results and the model agree well. At shorter wavelengths, the Drude-Sommerfield model fails to reproduce the measured results, particularly the resonances observed in $\epsilon''(\omega)$.

Most metals have a negative real part of the dielectric function in the visible range and an imaginary part that is comparable in magnitude to the real part (Fig. 2.1 and Appendix B). The wavevector can be related to the dielectric function by

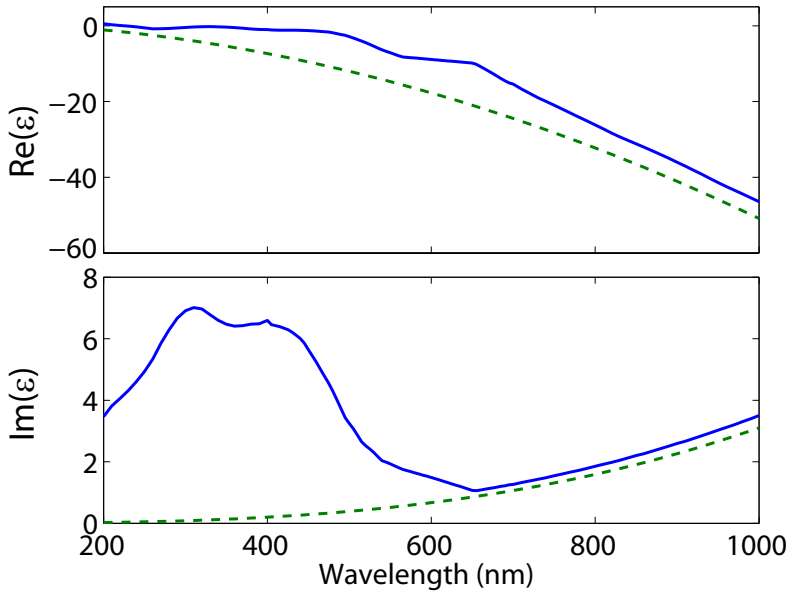

Figure 2.1. Dielectric function of bulk gold. Measured data (solid blue line) and the Drude-Sommerfield model (dotted green line). Dielectric function values are found in [11].

$k = (\omega/c)\sqrt{\mu\epsilon}$, where μ is the magnetic permeability. Therefore, if the dielectric function has an imaginary component, so does the wavevector k. As a result, the electromagnetic fields are attenuated as they propagate in the material: the electrons in the metal move to screen the applied field, thus decreasing the electric and magnetic fields as the light penetrates the metal. The exponential decay of the electromagnetic fields into the material has a characteristic decay length called *skin depth*:

$$\delta = \frac{\lambda}{4\pi\sqrt{\epsilon''}} \tag{2.5}$$

where λ is the wavelength of the incident light. For example, gold has a skin depth of $\delta \sim 31.5$ nm at $\lambda = 550$ nm. This is crucial for nanoscale optics because the size of nanoparticles may be on the same order of magnitude as the skin depth (at optical frequencies).

2.1.2 Dielectrics

Dielectrics have a very different response to an electromagnetic field compared to metals. For dielectrics, the main response to the alternating electric field is the

result of bound electrons. The AC conductivity in dielectrics is usually very small, indicating a minute amount of resistive losses in the material. Although silicon is a semiconductor, it has very small AC conductivity at optical frequencies and thus behaves largely as a dielectric. Silicon is a widely used material for near-field applications due to the large $\epsilon'(\omega)$ and small $\epsilon''(\omega)$ (relative to metal).

The measured dielectric function for silicon can be seen in Fig. 2.2. In the UV range, the real part (solid blue line) has a dispersion lineshape and the imaginary part (dotted green line) has a strong resonance peak. In the visible spectral range, the dielectric function does not change much. Typically, commercial silicon probes are doped. The type and concentration of dopant can influence the dielectric properties of silicon. However, the doping concentration and type of the dopants is different for each manufacturer and therefore the results shown here are only in qualitative agreement with that expected for silicon probes.

Other dielectric materials typically do not have an imaginary component in the

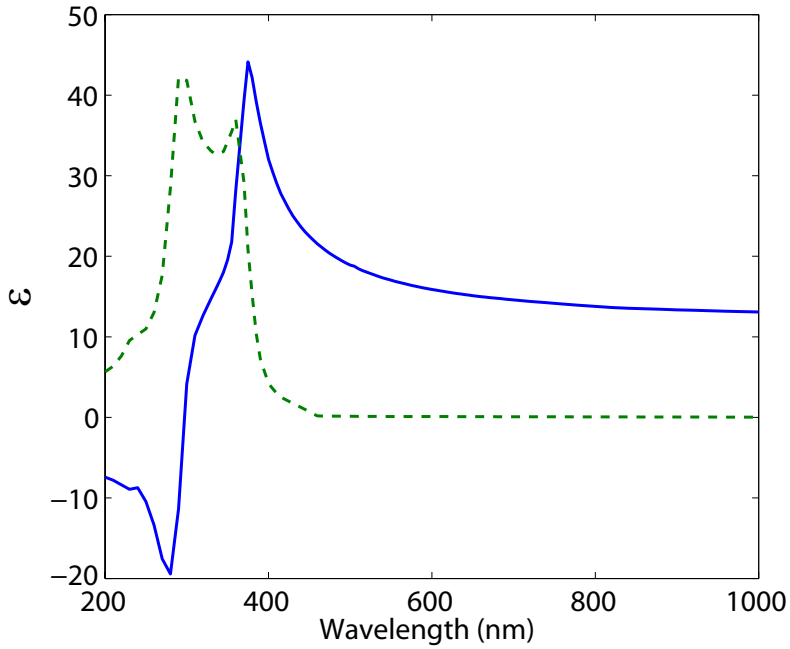

Figure 2.2. Dielectric function of doped silicon. In the optical range, the real part (solid blue line) is high while the imaginary part is fairly low (dotted green line). Data points taken from Ref. [13].

dielectric function, but their real part is substantially smaller than that of silicon (Appendix B).

2.2 Field enhancement

The working principle of a near-field microscope is usually to use a probe to enhance the local field in a nanometer-scale region to produce high-resolution images. The interaction between the excitation light and the near-field probe leads to the polarization of the probe, which can result in a locally confined spot with a much larger (local) amplitude than the incident light. Essentially, much like an antenna, the probe is used in order to concentrate the light source. The general demand for most near-field experiments is to increase the local intensity $I(r, r_0)$ compared with the far-field intensity $I_0(r_0)$ as the tip approaches the sample. Here, r_0 signifies the position of the emitter and r is the distance between the emitter and the probe. It is useful to define an *enhancement factor*, which describes the ratio between the local intensity and the far-field excitation intensity

$$\kappa(r) \equiv \frac{I(r, r_0)}{I_0(r_0)}. \tag{2.6}$$

If there is no tip-induced change in the absorption cross-section of the sample, the intensity is related to the excitation rate:

$$\frac{I(r, r_0)}{I_0(r_0)} = \frac{\Gamma_{\text{exc}}(r)}{\Gamma^0_{\text{exc}}} \tag{2.7}$$

where Γ^0_{exc} is the far-field excitation rate (i.e., when the tip is far away). Note that the enhancement factor, κ, depends on the tip-sample separation distance and is an indicator of how much intensity is gained by bringing the probe close to the sample. To optimize the near-field contrast, κ should be as large as possible, and to optimize resolution, κ should decay over as short a range as possible.

This section will discuss field-enhancement mechanisms and their dependence on different types of near-field probes. The most important field-enhancement effects are the lightning-rod effect and localized surface plasmon resonances. These two mechanisms are strongly dependent on the precise geometry of the near-field probe

and on the tip material, the excitation wavelength and the light's polarization with respect to the tip.

2.2.1 Lightning-rod effect

In the most general sense, field enhancement is the result of a discontinuity in the perpendicular (to the interface) component of the electric field amplitude on either side of an interface with different dielectric constants, as required by Maxwell's equations. To understand the basic mechanism of field enhancement, we first consider the simple example of a dielectric sphere in a uniform static electric field. In this case, the applied electric field causes the electrons and ions to migrate toward opposite ends of the sphere, thus polarizing the sphere. This creates an internal field inside the sphere resulting in a total electric field outside the sphere which is a superposition of both the applied and induced fields. If the sphere's size is much smaller than the wavelength, retardation effects can be neglected and a quasi-static approximation is justified even in the case of an oscillating electromagnetic field. The electric field inside and outside the sphere can be obtained by applying Maxwell's equations at the boundary of the sphere. In particular, the tangential component of the electric field and the normal component of the displacement field must be continuous at the boundary. In this case, the electric field can be expressed analytically:

$$\vec{E}_{\text{out}}(r,\theta) = E_0 \cos\theta \left[1 + 2\frac{\epsilon_r - 1}{\epsilon_r + 2}\frac{R^3}{r^3}\right]\hat{r} + E_0 \sin\theta \left[-1 + \frac{\epsilon_r - 1}{\epsilon_r + 2}\frac{R^3}{r^3}\right]\hat{\theta} \tag{2.8}$$

$$\vec{E}_{\text{in}}(r,\theta) = E_0 \left(\frac{3}{\epsilon_r + 2}\right)\left[\cos\theta\hat{r} - \sin\theta\hat{\theta}\right] = E_0 \left(\frac{3}{\epsilon_r + 2}\right)\hat{z} \tag{2.9}$$

where $\vec{E}_0 = |\mathbf{E_0}|\hat{z}$ is the applied field, R is the radius of the sphere and $\epsilon_r = \epsilon_{\text{dielectric}}/\epsilon_{\text{medium}}$ is the relative permittivity between the dielectric material and the surrounding material. Inside the sphere, the electric field is uniform and is in the same direction as the applied field. Outside the sphere, the field is a superposition of the applied field with the field of an electric dipole.

The field intensity for a 10 nm radius silicon sphere is plotted in Fig. 2.3. At the poles along the direction of the polarization, the intensity is enhanced whereas

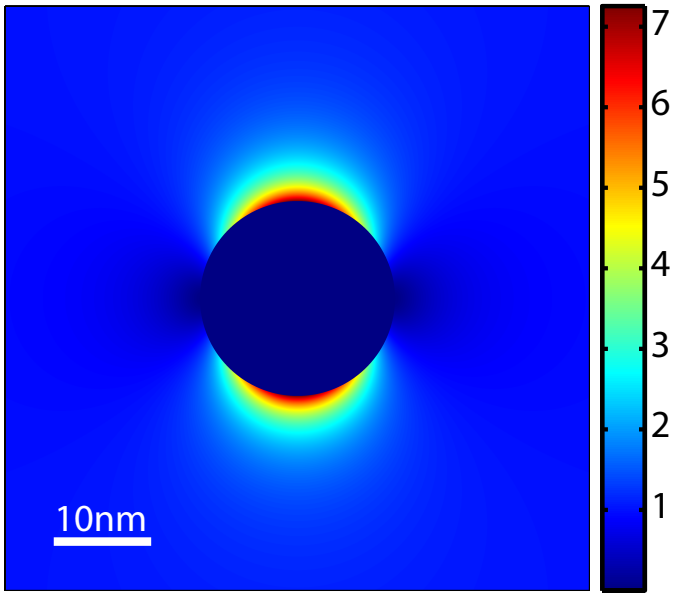

Figure 2.3. Dielectric sphere in a uniform electric field. The color scale illustrates the field intensity ($I \propto |\mathbf{E}|^2$). A 2D slice through the center of the sphere shows that the sphere causes a redistribution of the field, where it is strongest along the direction of the polarization (in this case the z-axis). The dielectric function used in this case is $\epsilon_{\mathrm{Si}} = 17.6 + i0.1$ for silicon at $\lambda = 532$nm.

the intensity is reduced near the equatorial plane. The maximum enhancement is achieved at the surface ($r = R$) and does not depend on the sphere size.

$$E_{\max} = E_0 \left(1 + 2\frac{\epsilon_r - 1}{\epsilon_r + 2}\right) \tag{2.10}$$

For dielectric materials, the maximum field enhancement is $E_{\max} = 3$ for $\epsilon_r \to \infty$ which results in an intensity enhancement of $I_{\max} = 9$.

For nonspherical geometries, the enhancement effect is amplified in regions of high curvature where the field line density is largest. This redistribution of the electric field is known as the *lightning-rod effect*, where fields are enhanced most strongly at the regions of highest curvature. For example, Bohn et al. [14] have shown that as the long axis of a prolate spheroid approaches infinity, the intensity enhancement adopts the analytic form:

$$E_{\max} = E_0 \epsilon_r. \tag{2.11}$$

Due to the high curvature at the ends (tips) of such a spheroid, the maximum field enhancement is no longer independent of ϵ_r and thus can be much greater than in the case of a sphere.

The lightning-rod effect can be very strong for any geometric shapes with sharp edges. Therefore, an AFM tip, which has a very sharp apex, is well designed to utilize the enhancement from the lighting-rod effect. Figure 2.4 illustrates the strong intensity enhancement at the apex of an AFM tip placed in an uniform static electric field. The intensity enhancement is much greater than that of the Si sphere (Fig. 2.3).

2.2.2 Localized surface plasmon resonance

A further contribution to the field enhancement can occur due to plasmon resonances in the material. For example, the solution for the electric field near a metallic sphere placed in a uniform electric field is similar to Eq. 2.8 as long as the diameter

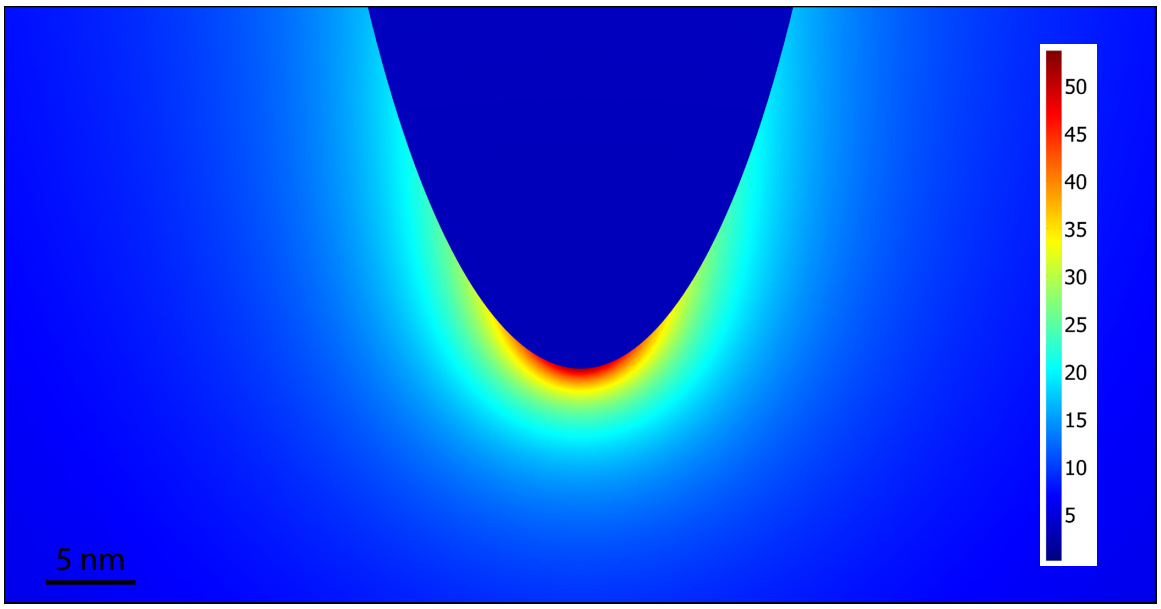

Figure 2.4. 3D electrostatic simulation of a near-field probe made out of silicon in a uniform static electric field. The color scale illustrates the magnitude of the field (i.e., $|\mathbf{E}|$). Only a small portion of the simulation area is shown here to emphasize the field enhancement near the apex of the tip.

of the sphere is much smaller than the skin depth (Eq. 2.5). If the sphere is small enough, light is not attenuated much as it travels through the sphere, and the field inside the sphere can be approximated to be uniform, similar to the dielectric case. However, since for most metals $\epsilon''(\omega) < 0$ at optical frequencies, the denominator in Eq. 2.10 vanishes when $\Re(\epsilon_r) = -2$ and as a result, the field enhancement diverges. This is called *Localized Surface Plasmon Resonance* (LSPR) because it results from collective oscillations of the charge carriers within the metal nanoparticle - in essence, nonpropagating (standing wave) oscillation of charges confined to a highly localized region.

LSPR can generate enormous field enhancement. The strength of the resonance depends sensitively on material, excitation wavelength, and geometry of the illuminated nanostructure. Moreover, given a certain geometry, the nanostructure size also matters. If the nanostructure is larger than the skin depth, the inner electrons will be shielded, and thus will not participate in the resonant oscillations, resulting in reduced enhancement. For smaller particles with large surface area-to-volume ratios, electron collisions with the surface become a large source of plasmon damping, thus reducing plasmonic field enhancement [9].

Figure 2.5 illustrates the importance of size, shape and composition in the light-scattering properties of metallic nanoparticles. The scattering for these particles is much stronger for incident wavelengths at the plasmon resonance, and therefore the scattering color is an indication of the plasmon resonance wavelength. Silver spheres scatter predominantly at different wavelengths as a function of sphere size, with a redshifted plasmon resonance for larger sphere diameters. For silver nanoprisims, the plasmon resonance is even more redshifted. The LSPR phenomenon is often used to create huge field enhancements for Surface Enhanced Raman Spectroscopy (SERS) [15, 16]. It is also possible to fabricate an AFM tip with a metallic sphere at its apex. In fact, these tips have proven to have very large signal enhancement factors [3, 17, 18]. The correlation between sphere size and signal enhancement for gold has been studied experimentally [3, 19].

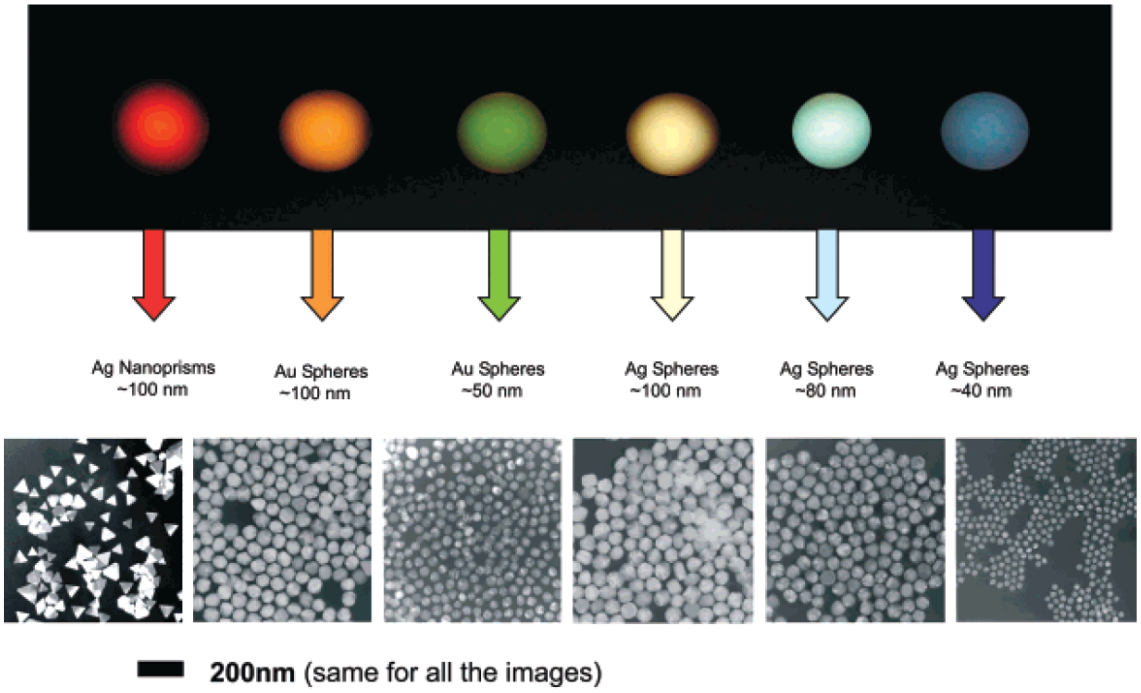

Figure 2.5. Localized Surface Plasmon Resonance in different nanostructures. The color of the scattered light depend on the nanosructure's size, shape and composition. Reprinted with permission from [20]. Copyright 2005 American Chemical Society.

2.2.3 Optical antenna

The combination of the lightning-rod effect and plasmon resonance have led researchers to design nanostructures with strong, shape-specific resonances in order to drastically enhance the optical field. This is, in fact, a description of an *optical antenna*, which like their radio or microwave analogs, can be used to convert free propagating electromagnetic waves into localized fields and vice versa. Many different optical antenna geometries have been theoretically proposed, and recently due to improvements in fabrication abilities, many have now been experimentally demonstrated [21–24]. An example of an asymmetrical bowtie antenna, which was fabricated in James Schuck's group, can be seen in Fig. 2.6. Optical antenna theory differs from antenna design in the radio and microwave spectral regions because at optical frequencies the skin depth is of the same order of magnitude as the antenna's dimensions [25]. Further information about optical antenna can be found in Ref.

[26, 27].

2.2.4 Interference effects

Another important effect that can influence the local field intensity, and thus κ, is interference of the direct excitation field with that scattered by the probe. The total excitation field , $E(r, r_0)$, at the location of a particular feature of the sample, r_0, is the superposition of the incident light and the scattered light. The resulting interference pattern strongly depends on illumination conditions, the shape and material of the probe, the position of the probe relative to the sample feature, r, and the polarization of the incident field with respect to the probe. Destructive interference can result in an enhancement factor κ smaller than unity, and constructive interference results in $\kappa > 1$.

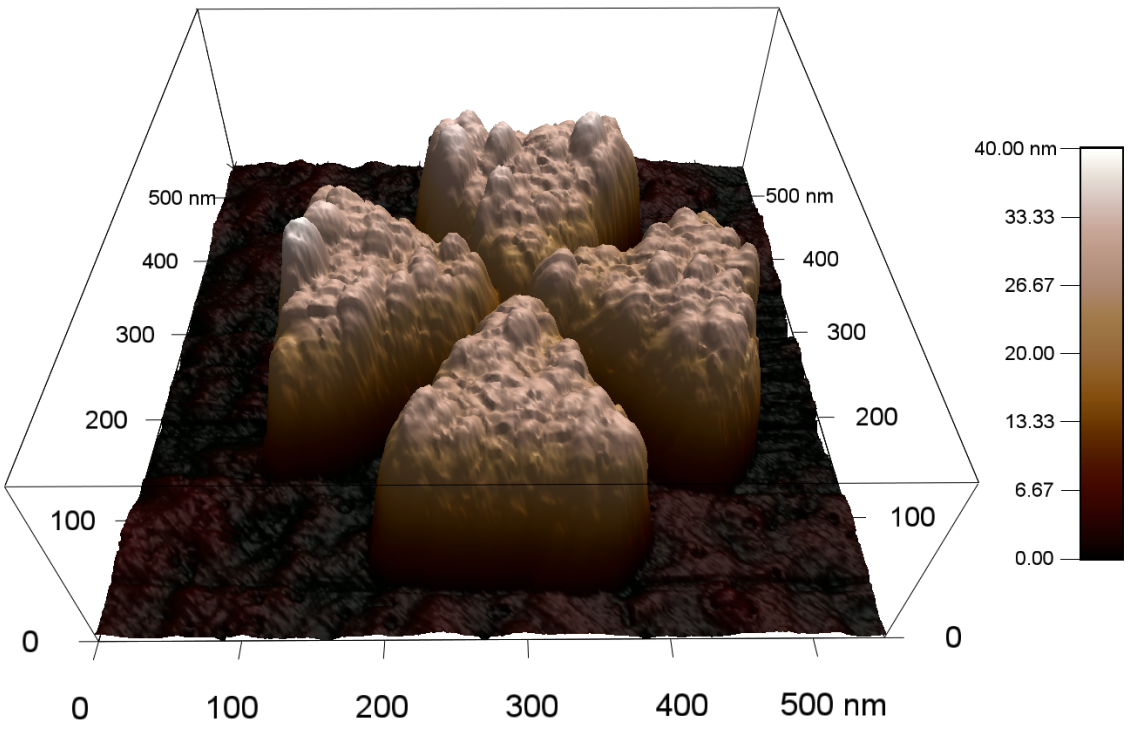

Figure 2.6. An example of an optical antenna. The antenna was fabricated in James Schuck's group and was scanned under our AFM. This unique antenna design enables spectral filtering and steering of optical fields [28, 29].

For elongated geometries like an AFM probe, light polarized parallel to the long axis of the tip (vertical polarization) leads to much stronger scattering than light polarized perpendicular to the tip (horizontal polarization). This correlates to the fact that vertical polarization produces a much larger field enhancement. Therefore, interference effects are stronger for vertically polarized excitation [30]. It has been shown that Total Internal Reflection (TIR) illumination creates parabolic shaped interference patterns that persist up to several wavelengths in the vicinity of the tip, and whose shape is due to shadowing of the incident field behind the tip. The direction of the shadow depends on the prorogation direction of the light [31]. Reduction in the measured signal due to destructive interference of the excitation field at tip-sample separation distances of roughly a wavelength has been observed for gold spheres [17]. The interference pattern depends on the particular tip geometry, as different shapes will cause different scattering [32]. Furthermore, the material of the tip also plays a crucial role because the phase shift of the scattered light with respect to the direct light depends on the reflection coefficient of the specific material [6, 7]. While the interference effects are secondary in importance and are typically much weaker than any field enhancement, they should not be overlooked.

2.2.5 AFM tips

For most probe geometries employed in near-field microscopy, an analytical solution for the field enhancement cannot be obtained. Furthermore, the long axis of a typical near-field probe is much larger than an optical wavelength; thus, a full electrodynamic approach must be used. More precise predictions of the field enhancement for realistic probe geometries, such as a cone or pyramid, can be obtained by solving Maxwell's equations using numerical simulations. Such calculations have predicted field enhancement values as high as 3,000 for metallic tips and 225 for dielectric tips [14, 33]. However, such large enhancement factors have never been observed experimentally. One possible reason for this is that the actual measured signal includes a few different effects that are difficult to deconvolve and some of which contribute to signal reduction (e.g., quenching). Another possible reason is

that $\epsilon(\omega)$ for geometries such as an AFM tip might deviate significantly from bulk values due to electron scattering on the surface and local defects [34].

An AFM geometry is not ideal for exploiting LSPR. The long axis of the AFM tip is a few orders of magnitude larger than the skin depth of any metal at optical frequencies and therefore the majority of electrons will be shielded from the field effect. On the other hand, due to the sharp edge of the AFM tip and its elongated geometry, enhancement due to lightning-rod effect is very strong. Numerical simulation for metallic geometries which resemble an AFM geometry, predict higher enhancement factors for closed geometries compared with an open geometry [35] indicating the importance of LSPR.

It is difficult to experimentally measure or extract the field enhancement factor. However, signal enhancement from metallic spheres [3, 17–19, 36] has been shown to be higher compared with commercial AFM tips with elongated geometry [32, 37–40]. This suggests that the field enhancement is stronger for metallic spheres than for commercial AFM probes.

2.3 Single emitters

Optical interactions of an emitter with a material are determined by both the properties of the emitter and the domain in which its located. In the first section, some general properties of materials, mainly the response of the material to an electric field, were discussed. These properties play an important role in determining the optical properties such as the quantum yield and angular emission of an emitter. In this section, the properties of single emitters in a homogeneous environment and the changes induced by an inhomogenous environment will be reviewed.

2.3.1 Dipole emission

In the classical sense, a two-level molecule can be described by an electric dipole moment oscillating at the emission frequency. If the dipole moment of the molecule is denoted by $\vec{p}$, then the electric and magnetic field generated by the dipole in a homogeneous environment are [6]

$$\mathbf{E} = \frac{e^{ikr}}{4\pi\epsilon_0}\left\{\frac{k^2}{r}\left(\mathbf{n}\times\mathbf{p}\right)\times\mathbf{n} + \left[3\mathbf{n}\left(\mathbf{n}\cdot\mathbf{p}\right) - \mathbf{p}\right]\left(\frac{1}{r^3} - \frac{ik}{r^2}\right)\right\} \tag{2.12}$$

$$\mathbf{H} = \frac{ck^2}{4\pi}\left(\mathbf{n}\times\mathbf{p}\right)\frac{e^{ikr}}{r}\left(1 - \frac{1}{ikr}\right) \tag{2.13}$$

where $\mathbf{n}$ is a unit vector, k is the wavevector, ϵ_0 is the permittivity in vacuum and r is the distance from the dipole. If we assume that the dipole is oriented in the z-axis, as illustrated in Fig. 2.7, and write the expressions for $\mathbf{E}$ and $\mathbf{H}$ in spherical coordinates, we have:

$$\begin{aligned} E_r &= \frac{e^{ikr}}{2\pi\epsilon_0\epsilon}\cos\theta\left(\frac{1}{r^3} + \frac{ik}{r^2}\right)|\mathbf{p}| \\ E_\theta &= \frac{e^{ikr}}{4\pi\epsilon_0\epsilon}\sin\theta\left(\frac{1}{r^3} + \frac{ik}{r^2} - \frac{k^2}{r}\right)|\mathbf{p}| \\ H_\phi &= \frac{e^{ikr}}{4\pi\epsilon_0\epsilon}\sin\theta\left(\frac{ik}{r^2} - \frac{k^2}{r}\right)|\mathbf{p}| \end{aligned} \tag{2.14}$$

where ϵ is the permitivitty of the medium.

The fields behave quite differently close to the dipole (i.e., in the near-field) and far away from it (far-field). In the near-field zone, where $kr << 1$, all the terms, but the $1/r^3$ term, can be neglected. The contribution of the propagating term e^{ikr} is small and the electric field has components in both radial and transverse directions.

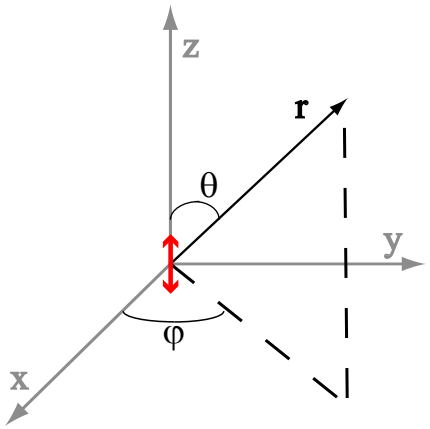

Figure 2.7. Dipole orientation. A dipole oriented in the z axis, i.e., $\mathbf{p} = |\mathbf{p}|\hat{z}$, in spherical coordinates.

The magnetic field in this region is much smaller than the electric field and therefore can be neglected.

On the other hand, in the far-field region, i.e., $kr >> 1$, the term $1/r$ is dominant. Therefore, only the transverse electric field component exists with a magnetic field perpendicular to both the electric field and the propagation direction. Furthermore, the radiation pattern in this region is quite different from the near-field zone.

Figure 2.8 illustrates the emission intensity pattern by a dipole oriented along the z-axis. Three different values of kr were chosen (kr $= 0.01, 2, 400$) to illustrate the field intensity pattern in the near-field, intermediate field and the far-field, respectively. Close to the dipole (2.8a), the field intensity is distributed in all directions with a higher intensity along the dipole's axis. In the far-field field (2.8c), the dipole does not radiate along its axis at all. The pattern in the intermediate region is highly affected by the choice of kr.

Only the far-field term contributes to the total energy transport. The Poynting vector, including only the far-field radiation, is

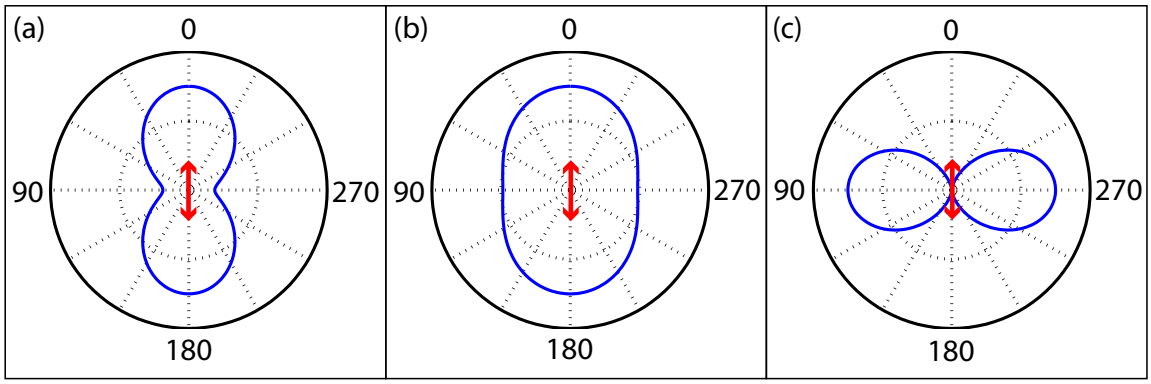

Figure 2.8. Dipole radiation pattern. The dipole radiation pattern for different kr values. Panel (a),(b) and (c) illustrate the intensity radiation pattern of a dipole in the near-field ($kr = 0.01$), intermediate field ($kr = 2$), and far-field ($kr = 400$), respectively. The dipole's direction is illustrated in red. In the near-field, the dipole radiates in all directions whereas in the far-field, the dipole does not radiate along its axis. The magnitude of the intensity is much stronger close to the dipole and is not illustrated in this figure.

$$\mathbf{S}(t) = \mathbf{E}(t) \times \mathbf{H}(t) = \frac{1}{16\pi^2\epsilon_0\epsilon} \frac{\sin^2\theta}{r^2} \frac{n^3\omega^4}{c^3} \hat{r} \tag{2.15}$$

The time-averaged power radiated by an electric dipole can be determined by integrating the Poynting vector over a spherical surface [7], which yields the following value

$$\bar{P}_0 = \frac{ck^4}{12\pi\epsilon_0} |\mathbf{p}|^2 \tag{2.16}$$

2.3.2 Spontaneous decay

Spontaneous emission from a quantum emitter depends in part on the intrinsic properties of the emitter and, in part, on the environment which surrounds the emitter. Purcell [41] discovered that by placing an atom in a resonant cavity, the emission rate of the atom can be modified. This discovery led to the realization that the surrounding environment can strongly affect the spontaneous decay rates of molecules.

To calculate the spontaneous decay rate of a two level quantum emitter, one is required to use quantum electrodynamics (QED). From the Fermi golden rule the following spontaneous decay rate can be obtained [1]:

$$\Gamma = \frac{2\omega}{3\hbar\epsilon_0} |\mathbf{p}|^2 \rho_\mu(\mathbf{r_0}, \omega) \tag{2.17}$$

where $\mathbf{r_0}$ denotes the position of the emitter, ω is the transition frequency and $\rho_\mu(\mathbf{r_0}, \omega)$ is the electromagnetic *local density of states*. An emitter in the excited state can go back to the ground state via a few mechanisms: emission of a photon, internal nonradiative relaxation processes, or by virtual energy transfer to the environment. The first mechanism is radiative and is characterized by the radiative rate (Γ_r) while the last two are nonradiative and denoted by a nonradiative rate (Γ_{nr}). The total decay rate is always a sum of the two effects, i.e., $\Gamma = \Gamma_r + \Gamma_{nr}$. The spontaneous decay of an emitter is typically characterized by intrinsic radiative and nonradiative rates. Once the emitter is placed in an inhomogeneous environment, both the intrinsic radiative and nonradiative rates may be modified.

Often, the emitter's spontaneous decay rate in an inhomogeneous environment (Γ) is compared to the rate in a homogeneous environment (Γ_0). For weak coupling

between the emitter and the environment, the results obtained for Γ/Γ_0 using QED and classical theory have been shown to be the same [1].

In the classical picture, the spontaneous emission from a dipole in a homogeneous environment can be described by a simple harmonic oscillator [42]

$$\ddot{p} + \Gamma_0 \dot{p} + \omega^2 p = 0 \tag{2.18}$$

where ω is the oscillation frequency and Γ_0 is the damping rate. The energy of the oscillator decays exponentially with a characteristic time of τ_0, where $\tau_0 = 1/\Gamma_0$ is the *fluorescence lifetime* of the molecule and is defined as the inverse of the spontaneous decay rate.

In an inhomogeneous environment, some of the emitted light is scattered back to the molecule and acts as a driving force on the molecule [42, 43]. Equation 2.19 can be modified to account for the driving force

$$\ddot{p} + \Gamma_0 \dot{p} + \omega^2 p = \frac{q^2}{m} E_s(r_0) \tag{2.19}$$

where m and q are the effective mass and the electric charge of the molecule and $E_s(r_0)$ is the scattered electric field at the position of the molecule. Assuming $\Gamma << \omega$ and weak interaction with the scattered field, the solution to Eq. 2.19 follows

$$\frac{\Gamma}{\Gamma_0} = 1 + q_0 \frac{6\pi\epsilon_0}{|\mathbf{p}|^2} \frac{1}{k^3} E_s(r_0) \tag{2.20}$$

where q_0 is the intrinsic quantum efficiency of the emitter and k is the wavevector.

The problem of calculating the modification to the molecule's spontaneous decay rate is now reduced to finding the electric field reflected from the environment. This is not an easy task and can only be done analytically for very specific cases [42, 44], that will be discussed in the following section.

2.3.3 Energy dissipation in lossy material

The energy of an emitter in the excited state can be dissipated without the emission of a photon, or in other words, through nonradiative processes. Some processes are intrinsic to the emitter, for example, energy loss due to vibrations or Auger recombination in nanocrystal quantum dots [45]. Other processes, such as

energy transfer to the environment or to other molecules, are also nonradiative and strongly depend on the surrounding environment.

A lossy material placed close to a fluorescence molecule may open up additional channels for photo-excited fluorophores to relax back to the electronic ground state nonradiatively, thereby quenching the fluorescence. In this process, it is thought that energy is transferred from fluorophore to environment via exchange of a virtual photon, which in turn causes electron movement in/on the lossy material. The electrons then dissipate the energy rapidly in the form of resistive heating within the lossy material.

In near-field microscopy, as a near-field probe approaches a fluorescent sample, the local nonradiative relaxation rate may increase and as a result lead to suppression of the detected emission [44, 46]. This fluorescence quenching may be accompanied by a change in the radiative rate, where both the radiative and nonradiative rates depend on the orientation of the molecule transition dipole moment relative to the probe geometry [44, 47]. If the losses are due to Ohmic losses, the nonradiative decay rate can be determined by [3, 48]

$$\Gamma'_{nr}(\mathbf{r}) = \frac{1}{\hbar\omega}\frac{1}{2}\int_V Re\left\{\mathbf{j}^*(\mathbf{r})\cdot\mathbf{E}(\mathbf{r})\right\} d\mathbf{r}^3 \tag{2.21}$$

where V denotes the volume of the lossy material, $\mathbf{j}(\mathbf{r})$ is the current density and $\mathbf{E}(\mathbf{r})$ is the electric field emitted by the molecule. The current density can be expressed in terms of the electric field and the imaginary part of the dielectric function

$$\mathbf{j}(\mathbf{r}) = \epsilon_0\omega\epsilon''\mathbf{E}(\mathbf{r}) \tag{2.22}$$

Using equations 2.21 and 2.22, it is apparent that the nonradiative decay rate will be much higher for materials with a high imaginary part of the dielectric function. For this reason, metals usually induce a high nonradiative rate, while dielectrics do not. Furthermore, the nonradiative decay rate will be much higher when the lossy material is close to the molecule where the emitted electric field is stronger. Since the dielectric function of a material is wavelength dependent, the fluorescence quenching efficiency depends on the emission wavelength of the fluorophore. The maximum nonradiative decay rate for metals is at the plasmon resonance frequency where ϵ'' is the highest.

If the geometry and the dielectric function of the lossy material are known, it is possible to calculate the nonradiative decay rate analytically [42, 44] or by numerical simulations [3, 48]; this will be discussed further in the next section.

2.3.4 Energy transfer between molecules

Förster resonance energy transfer (FRET) describes the energy exchange between two molecules and is also a form of nonradiative decay. Within this model, a fluorescence molecule in the excited state (donor) may relax back to its ground state by transferring energy to a nearby molecule (acceptor). In order for the molecules to transfer energy, the emission spectrum from the donor must overlap with the absorption spectrum of the acceptor. This is depicted in Fig. 2.9a, where the emission from a green fluorescent protein (GFP) overlaps with the obsorption of a yellow fluorescent protein (YFP). The overlap opens up an energy transfer channel from the donor to the emitter with an energy transfer rate of Γ_{et}. Typically, excitation of a fluorescence molecule is followed by thermal vibrations, which cause a small loss in energy. Once some of the acceptor's energy is lost, there is no longer an overlap in energy between the two molecules and the acceptor can not transfer energy back to the donor. If the rate of vibrational energy dissipation in the acceptor (Γ_{vib}) is much faster than the energy transfer rate from the donor to the acceptor, i.e., $\Gamma_{vib} >> \Gamma_{et}$, the coupling between the molecules is called *weak coupling*.

Figure 2.9b illustrates the FRET cycle. First, the donor molecule is excited by an external source and relaxes via vibrations to a lower band in the excited state. The excited molecule can go back to the ground state either via emission of a photon, internal nonradiative relaxation, or by transferring energy to a nearby acceptor molecule. The FRET process usually ends with the emission of a photon from the acceptor or via nonradiative relaxation of the acceptor to its ground state.

Förster calculated the energy transfer rate from the donor to the acceptor in a weak coupling regime based on classical considerations. However, similar equations are derived from a quantum mechanics stand point [49]. The energy transfer rate found by Förster is:

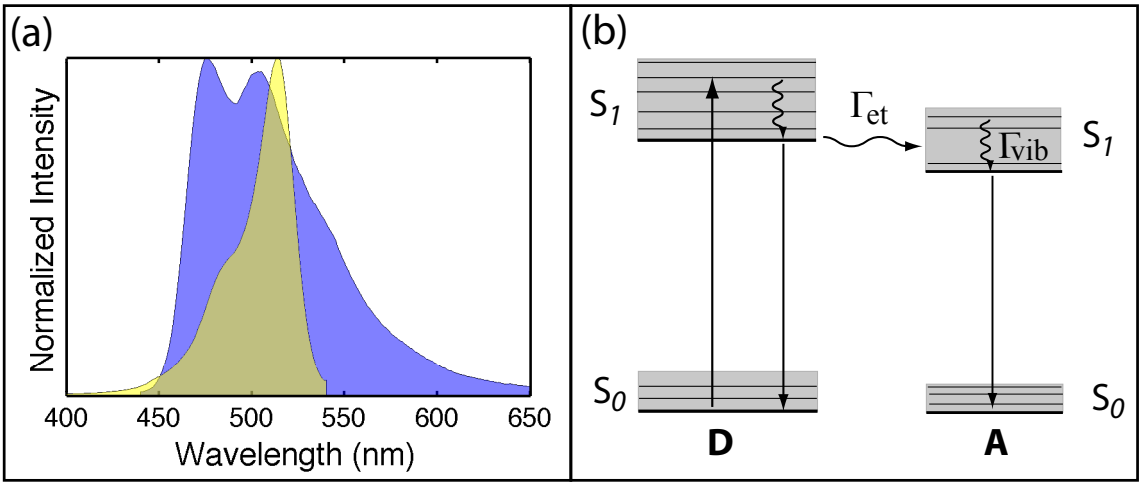

Figure 2.9. Förster resonance energy transfer. Panel (a) is the emission of GFP (blue) and absorption of YFP (yellow). Panel (b) shows the cycle of the FRET process. The donor molecule is excited from the ground state to an excited state. If an acceptor molecule is nearby the donor, an addional energy channel between the two is opened.

$$\frac{\Gamma_{et}}{\Gamma_0} = \left(\frac{R_0}{r}\right)^6 \tag{2.23}$$

where r is the distance between the molecules and R_0 is the Förster radius. The Förster radius can be calculated by [50]

$$R_0^6 = q_0 \frac{9000 \cdot \ln(10)\kappa^2}{128\pi^5 N n^4} J(\lambda) \tag{2.24}$$

where q_0 is the intrinsic quantum yield of the donor, N is Avogadro's number, n is the refractive index of the medium and $J(\lambda)$ is the spectral overlap integral which is defined as follows:

$$J(\lambda) = \int_0^\infty f_D(\lambda)\epsilon_A(\lambda)\lambda^4 d\lambda \tag{2.25}$$

where $f_D(\lambda)$ is the emission spectrum of the donor with total intensity normalized to unity and $\epsilon_A(\lambda)$ is the absorption spectrum of the acceptor. The factor κ depends on the dipole's orientation and is denoted by

$$\kappa^2 = \left[\mathbf{n}_A \cdot \mathbf{n}_D - 3\left(\mathbf{n}_R \cdot \mathbf{n}_D\right)\left(\mathbf{n}_R \cdot \mathbf{n}_A\right)\right]^2 \tag{2.26}$$

where $\mathbf{n}_D$ and $\mathbf{n}_A$ are the transition dipole orientation of the donor and acceptor respectively, and $\mathbf{n}_R$ is the direction of the vector between the acceptor and donor. The energy transfer efficiency between the molecules can be calculated by

$$E = \frac{\Gamma_{et}}{\Gamma_{et} + \Gamma_0} = \frac{1}{1 + (r/R_0)^6} \tag{2.27}$$

Therefore, the Förster radius indicates the distance between the molecules where the energy transfer efficiency drops to 1/2 of the peak value. The stronger the molecules are coupled together, the longer that distance. For FRET between single molecules, the Förster radius is typically between $3-6$ nm depending on the specific combination of donor and acceptor molecules.

2.3.5 Quantum yield

The quantum yield of an emitter changes in an inhomogeneous environment due to changes in the radiative and nonradiative rates. These changes lead to a quantum yield which is different than the intrinsic one. One must take into account that the modification in the rates depends on the exact position of an object, which introduces the inhomogeneity, relative to the emitter. The intrinsic quantum yield can be described by

$$q_0 = \frac{\Gamma_r}{\Gamma_0} = \frac{\Gamma_r}{\Gamma_r + \Gamma_{nr}} = \Gamma_r \tau_0 \tag{2.28}$$

where Γ_r is the intrinsic radiative rate of the molecule, Γ_{nr} in the intrinsic nonradiative rate, Γ_0 is the total intrinsic decay rate and τ_0 is the fluorescenece lifetime. The quantum yield due to an interaction with a nearby object can be described by introducing additional nonradiative (Γ'_{nr}) and radiative decay (Γ'_r) rates to the intrinsic rates [50].

$$\Gamma_r \rightarrow \Gamma_r + \Gamma'_r(z) \tag{2.29}$$

$$\Gamma_{nr} \rightarrow \Gamma_{nr} + \Gamma'_{nr}(z) \tag{2.30}$$

If the above substitutions into Eq. 2.28 are made, the apparent quantum yield takes the following form

$$q(r) = \frac{\Gamma_r + \Gamma'_r(r)}{\Gamma_r + \Gamma_{nr} + \Gamma'_r(r) + \Gamma'_{nr}(r)} = \frac{\Gamma_r + \Gamma'_r(r)}{\Gamma_0 + \Gamma'(r)} = \left[\Gamma_r + \Gamma'_r(r)\right] \tau(r) \tag{2.31}$$

where we define $\tau(r) \equiv [\Gamma_0 + \Gamma']^{-1}$ as the fluorescence lifetime in the presence of a proximate object and $\Gamma' \equiv \Gamma'_r + \Gamma'_{nr}$ as the *modified relaxation* rate.

Chance, Prock and Sibley calculated the decay rate Γ of a single molecule in the proximity of a reflecting mirror [42]. The electric field of a single molecule is found using Eq. 2.12 and the total electric field in space can be calculated by taking into account reflections from the mirror. The presence of the mirror modifies both the radiative and nonradiative decay rates, which can be found separately. Figure 2.10 summarizes the results for the decay rates and the quantum yield for a dipole perpendicular to the interface of the mirror, as a function of the distance from the mirror. In this case, the mirror is made out of gold, the emission wavelength is $\lambda = 605$ nm and the intrinsic quantum yield of the molecule is unity. The radiative rate changes most dramatically on a wavelength length scale. The nonradiative rate monotonically increases as the mirror gets close to the molecule. At short distances, $\Gamma'_{nr} \propto z^{-3}$ as can be calculated from Eq. 2.21 for this geometry. At these distances, the nonradiative rate dominates, as is apparent from the reduction of the quantum yield. The same calculation can be performed for a dipole oriented parallel to the mirror interface and yields very different results from the one shown here.

For a dipole placed near a small metal sphere, Carminati et al. [44] calculated the modification to the decay rates and field enhancement assuming only dipole-dipole interactions. Anger et al. [3] calculated the same thing for a single emitter oriented in the z-axis by means of a numerical simulation. The results of the different approaches for the quantum yield and the field enhancement are shown in Fig. 2.11a. While the dipole approximation and the numerical simulation yield similar results for the field enhancement from a gold sphere, the dipole approximation underestimates the quantum yield by a cosiderable amount. The total emission rate for spheres of different sizes is shown in Fig. 2.11b. There is an obvious competition between field enhancement and quantum yield (which leads to emission reduction in this case).

Issa et al. [48] modeled the changes in the rates of an emitter close to an object geometry that resembles an AFM tip. Interestingly, their work suggests that even in the absence of damping (i.e., $\epsilon''(\omega) = 0$), a fluorophore can couple to a metal tip via intermediate range ($10 - 50$nm) excitation of surface plasmon traveling waves, which for an open-geometry tip (e.g., metal coated cone or pyramid) results in a reduction

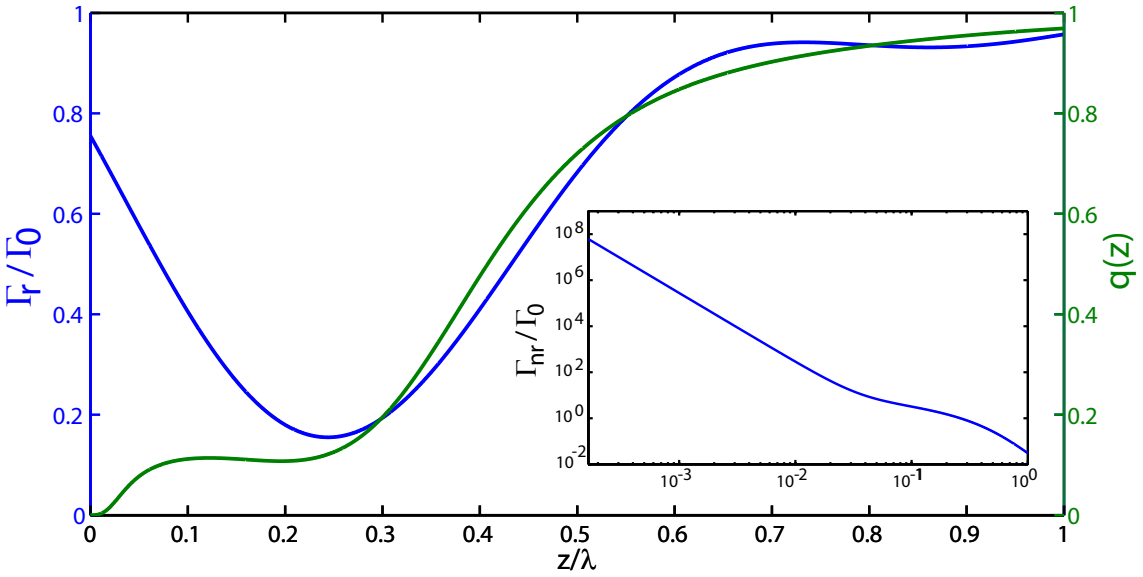

Figure 2.10. Dipole emitter near a reflecting mirror. The decay rates for a perpendicular dipole as a function of distance from a gold mirror. The blue line in the main figure (inset) indicates the changes in the radiative (nonradiative) rate of the emitter. These changes lead to a variation in the quantum yield (green line). The intrinsic quantum yield is assumed to be unity and the emission wavelength is 605 nm.

of the quantum yield and the fluorescence signal.

By using pulsed lasers and time-correlated single photon counting (TCSPC), it is possible to experimentally measure the fluorescence lifetime of a single emitter. The lifetime measurements can even be extended to produce a tip-sample distance dependent lifetime data [51, 52]. However, since the radiative decay rate cannot be measured directly, it can be quite challenging to measure the quantum yield or even the intrinsic quantum yield of single fluorophores.

2.4 Collection efficiency and angular emission

The collection efficiency of the system is determined by a few factors: the amount of light collected by the microscope objective relative to the total light emitted, the optical signal losses due to optical components, and the detection efficiency of the photon detector. The last two are constant for a specific emission wavelength.

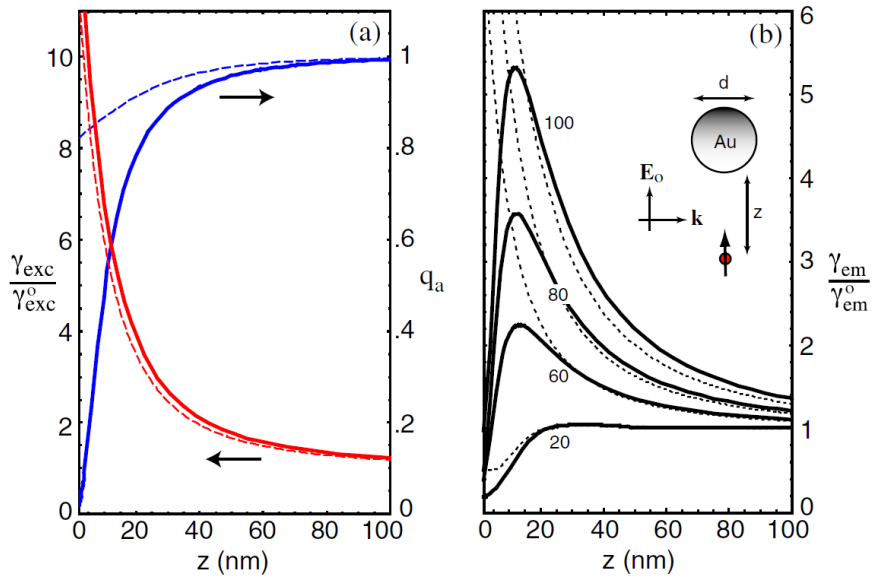

Figure 2.11. Single molecule emission next to a gold sphere. Panel (a) plots the increase in excitation rate due to enhancement (red) and the decrease in quantum yield (blue). The solid lines where calculated using numerical simulation while the dotted lines are the analytic results usint the dipole approximation taken from Ref. [44]. Panel (b) shows the total emission rate for different sphere sizes. The emission rate is determined by the product of the excitation rate and the quantum yield. The dipole orientation of the molecule is in the z-axis and its intrinsic quantum yield is unity. Reprinted figure with permission from [3]. Copyright (2006) by the American Physical Society.

However, the percentage of light collected by the objective depends on the angular emission of the emitter which in turn depends on the orientation of the emission dipole and the environment.

It is useful to define the angular directivity of the emitted light which reflects on the directionality of the emitted power:

$$D(\varphi,\theta) = \frac{4\pi P(\varphi,\theta)}{\int P(\varphi,\theta)d\Omega} \tag{2.32}$$

where $P(\varphi,\theta)$ is the radiated power and φ and θ are the same angles defined in Fig. 2.7. For isotropic emission $D(\varphi,\theta) = 1$, while for a radiating dipole, the directivity is similar to the far-field emission pattern from Fig. 2.8 with a maximum directivity of $D_{max} = 1.5$.

The environment of the emitter plays a crucial role in the angular directivity of an emitter. When an emitter is placed close to an interface between two mediums with a different dielectric function, most of the emission will be radiated into the medium with the higher dielectric function. In a typical experiment a dipole is located right above a glass-air interface. In these cases, about 85% of the light is radiated into the glass; this can be determined analytically [42]. The introduction of the glass also causes a change in the angular emission pattern as depicted in Fig. 2.12. Futhermore, if a near-field probe is nearby the molecule, the radiation pattern can change even further, thus modifying the amount of light radiated into the glass medium.

In an experiment, the only detected light is that which radiates into the microscope objective. The collection efficiency of the objective can be obtained by

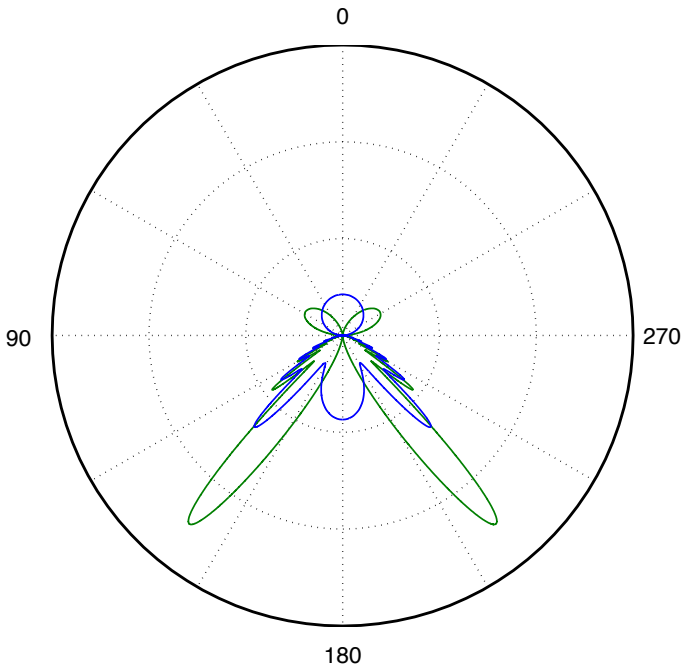

Figure 2.12. Electric dipole near a glass-air interface. A dipole placed 1 nm above a glass interface with perpendicular orientation (with respect to the interface) depicted in green and parallel orientation in blue. The radiation pattern depends on the orientation of the molecule, and in both cases, the majority of the (propagating) radiation is emitted into the glass medium (lower half).

$$\eta_{coll} = \frac{1}{4\pi} \int_0^{2\pi} \int_0^{\theta_{NA}} D(\varphi, \theta) \sin(\theta) d\theta d\varphi \tag{2.33}$$

where θ_{NA} is the maximum collection angle of the objective. The higher the numerical aperture of the microscope objective (which means larger θ_{NA}), the better the collection efficiency will be.

Significant changes in the angular emission of a single molecule may occur due to strong near-field coupling with an optical antenna [21, 24, 54, 55], which can lead to different collection efficiencies. Taminiau et al. [53] calculated the collection efficiency of different microscope objectives when a molecule is placed close to an optical antenna. Their results are shown in Fig. 2.13 for horizontally and vertically oriented dipoles and for two different microscope objectives. The dipole was placed 10 nm below an aluminum antenna and the collection efficiency was calculated as the antenna

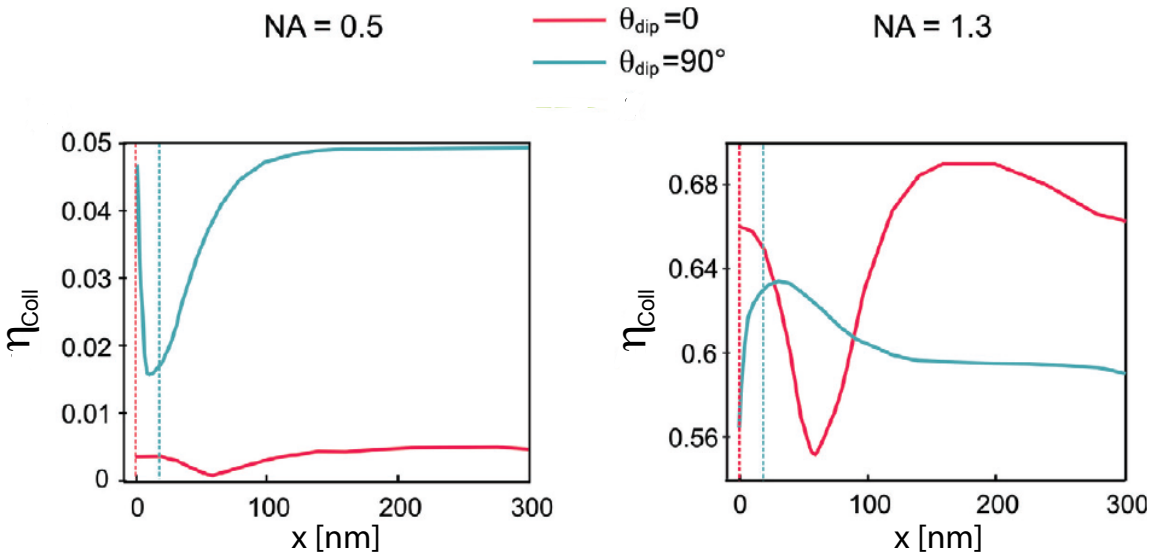

Figure 2.13. Microscope objective collection efficiency of single molecule emission next to an optical antenna. The collection efficiency for the low NA is very low and also depends on the orientation of the molecule. For the high NA, the relative changes in the collection efficiency as a function of lateral distance from the antenna are reduced. Furthermore, the collection efficiency for different dipole orientations is much closer. Reprinted figure with permission from [53].

moves in the lateral direction. While the detection efficiency of the high NA objective exhibits relatively small changes between the different dipole orientations as a function of distance from the antenna, the low NA objective exhibits quite large changes.

The total collection efficiency of the system is:

$$C(r) = \xi \eta_{coll}(r) \tag{2.34}$$

where the collection efficiency of the objective now depends on the distance of the sample from the near-field probe and ξ is the collection efficiency of the detection path, including losses in the optical components and the quantum efficiency of the photon detector.

2.5 The measured signal

In this section, the experimentally measured signal is derived using the parameters defined in the previous sections.

For light focused by a microscope objective, assuming one fluorophore in the focal area and excitation intensities far from saturation, the detected far-field emission count rate can be denoted by

$$S_{ff} = C_0 \Gamma^0_{exc} q_0 = C_0 I_0(r_0) \sigma_0 \left(\frac{\lambda}{hc}\right) q_0 \tag{2.35}$$

where C_0 is the collection efficiency of the system, σ_0 is the absorption cross-section of the molecule and $\frac{hc}{\lambda}$ is the energy of a detected photon.

For a molecule in the proximity of an object, the emission count rate can be quite different from Eq. 2.35. The intensity I_0 at the molecule position can either increase or decrease depending on the illumination conditions, the distance of the molecule from the near-field object, and the shape and geometry of the object. The radiative rate Γ_r can alter due to a change in the local density of states (i.e., the Purcell effect). At short distances, the object may introduce additional nonradiative channels, thus, increasing the nonradiative relaxation rate. Finally, the collection efficiency of the system can vary due to the presence of the object. One can denote the signal in the near-field as

$$S_{nf} = C(r) \Gamma_{exc}(r) q(r) = C(r) I(r, r_0) \sigma_0 \left(\frac{\lambda}{hc}\right) q(r) \tag{2.36}$$

It is often useful to normalize the near-field signal (Eq. 2.36) to the far-field signal (Eq. 2.35). In such a case, the normalized signal can be denoted by

$$S_{\text{norm}} = \kappa(r)\frac{q(r)}{q_0}\frac{C(r)}{C_0} \tag{2.37}$$

If the collection efficiency is similar in the far-field and near-field ($C(r) \sim C_0$), which is true for high numerical aperture objectives, the normalized signal takes an even simpler form

$$S_{\text{norm}} = \kappa(r)\frac{q(r)}{q_0} \tag{2.38}$$

Since the fluorescence lifetime is a measurable quantity, it is useful to rewrite Eq. 2.38 in terms of the tip-induced fluorescence lifetime and the intrinsic fluorescence lifetime. Using equations 2.28 and 2.31 the normalized fluorescence signal can be denoted by:

$$S_{\text{norm}} = \kappa(r)\left(1 + \Gamma_r'/\Gamma_r\right)\frac{\tau}{\tau_0} \tag{2.39}$$

The goal of this chapter was to examine equations 2.36, 2.38 and 2.39 and to understand how these equations determine the experimentally measured signal. Therefore, it is also essential to comprehend the mechanisms which impact and alter these equations.

2.6 References

[1] L. Novotny and B. Hecht, *Principles of Nano-Optics*, Cambridge University Press, Cambridge, 2006.

[2] B. D. Mangum, E. Shafran, J. Johnston, and J. M. Gerton, Near-field scanning optical microscopy, in *Optical Techniques for Solid-State Materials Characterization*, edited by R. P. Prasankumar and A. J. Taylor, CRC Press, 2011.

[3] P. Anger, P. Bharadwaj, and L. Novotny, Physical Review Letters **96** (2006).

[4] P. Drude, Annalen der Physik **306**, 566 (1900).

[5] A. Sommerfeld and H. Bethe, *Elektronentheorie der Metalle*, Springer, Verlag, 1967.

[6] J. D. Jackson, *Classical Electrodynamics*, John Wiley and Sons, Hoboken, third edition, 1999.

[7] M. Born and E. Wolf, *Principles of Optics: Electromagnetic Theory of Propagation, Interference and Diffraction of Light*, Cambridge University Press, New York, seventh edition, 2002.

[8] N. W. Ashcroft and N. D. Mermin, *Solid State Physics*, Saunders College, Philadelphia, 1976.

[9] S. Link and M. A. El-Sayed, Journal of Physical Chemistry B **103**, 4212 (1999).

[10] C. Kittel, *Introduction to Solid State Physics*, John Wiley & Sons, Hoboken, N.J., eighth edition, 2005.

[11] L. G. Schulz, Journal of the Optical Society of America **44**, 357 (1954).

[12] N. K. Grady, N. J. Halas, and P. Nordlander, Chemical Physics Letters **399**, 167 (2004).

[13] S. Adachi, Physical Review B **38**, 12966 (1988).

[14] J. L. Bohn, D. J. Nesbitt, and A. Gallagher, Journal of the Optical Society of America A **18**, 2998 (2001).

[15] K. Kneipp et al., Physical Review Letters **78**, 1667 (1997).

[16] K. A. Willets and R. P. Van Duyne, Annual Review of Physical Chemistry **58**, 267 (2007).

[17] S. Khn, U. Hkanson, L. Rogobete, and V. Sandoghdar, Physical Review Letters **97**, 017402 (2006).

[18] P. Bharadwaj and L. Novotny, Journal of Physical Chemistry C **114**, 7444 (2010).

[19] H. Eghlidi, K. G. Lee, X. W. Chen, S. Gotzinger, and V. Sandoghdar, Nano Letters **9**, 4007 (2009).

[20] N. L. Rosi and C. A. Mirkin, Chemical Reviews **105**, 1547 (2005).

[21] A. G. Curto et al., Science **329**, 930 (2010).

[22] J. N. Farahani, D. W. Pohl, H. J. Eisler, and B. Hecht, Physical Review Letters **95**, 4 (2005).

[23] T. H. Taminiau, R. J. Moerland, F. B. Segerink, L. Kuipers, and N. F. van Hulst, Nano Letters **7**, 28 (2007).

[24] T. H. Taminiau, F. D. Stefani, F. B. Segerink, and N. F. Van Hulst, Nature Photonics **2**, 234 (2008).

[25] L. Novotny, Physical Review Letters **98**, 266802 (2007).

[26] P. Bharadwaj, B. Deutsch, and L. Novotny, Advances in Optics and Photonics **1**, 438 (2009).

[27] L. Novotny and N. van Hulst, Nature Photonics **5**, 83 (2011).

[28] Z. Zhang et al., Nano Letters **9**, 4505 (2009).

[29] A. McLeod et al., Physical Review Letters **106** (2011).

[30] F. H'Dhili, R. Bachelot, A. Rumyantseva, G. Lerondel, and P. Royer, Journal of Microscopy **209**, 214 (2003).

[31] H. Hamann, M. Kuno, A. Gallagher, and D. J. Nesbitt, Journal of Chemical Physics **114**, 8596 (2001).

[32] S. Kuhn and V. Sandoghdar, Applied Physics B **84**, 211 (2006).

[33] L. Novotny, R. X. Bian, and X. S. Xie, Physical Review Letters **79**, 645 (1997).

[34] L. Novotny and S. J. Stranick, Annual Review of Physical Chemistry **57**, 303 (2006).

[35] J. T. Krug, E. J. Sanchez, and X. S. Xie, Journal of Chemical Physics **116**, 10895 (2002).

[36] P. Bharadwaj and L. Novotny, Optics Express **15**, 14266 (2007).

[37] B. Mangum, E. Shafran, C. Mu, and J. Gerton, Nano Letters **9**, 3440 (2009).

[38] F. Huang, F. Festy, and D. Richards, Applied Physical Letters **87**, 183101 (2005).

[39] A. Kramer, W. Trabesinger, B. Hecht, and U. Wild, Applied Physical Letters **80**, 1652 (2002).

[40] W. Trabesinger, A. Kramer, M. Kreiter, B. Hecht, and U. P. Wild, Applied Physics Letters **81**, 2118 (2002).

[41] E. M. Purcell, Physical Review **69**, 681 (1946).

[42] R. R. Chance, A. Prock, and S. R., Advances in Chemical Physics **37**, 1 (1978).

[43] H. Kuhn, Journal of Chemical Physics **53**, 101 (1970).

[44] R. Carminati, J. J. Greffet, C. Henkel, and J. M. Vigoureux, Optics Communications **261**, 368 (2006).

[45] M. Nirmal et al., Nature **383**, 802 (1996).

[46] L. Novotny, Applied Physics Letters **69**, 3806 (1996).

[47] S. Vukovic, S. Corni, and B. Mennucci, The Journal of Physical Chemistry C **113**, 121 (2008).

[48] N. A. Issa and R. Guckenberger, Optics Express **15**, 12131 (2007).

[49] R. M. Clegg, Fluorescence resonance energy transfer, in *Fluorescence Imaging Spectroscopy and Microscopy*, edited by X. F. Wang and B. Herman, John Wiley & Sons, New York, 1996.

[50] J. R. Lakowicz, *Principles of Fluorescence Spectroscopy*, Springer, New York, third edition, 2006.

[51] E. Yoskovitz, D. Oron, I. Shweky, and U. Banin, The Journal of Physical Chemistry C **112**, 16306 (2008).

[52] E. Yoskovitz, G. Menagen, A. Sitt, E. Lachman, and U. Banin, Nano Letters **10**, 3068 (2010).

[53] T. H. Taminiau, F. D. Stefani, and N. F. Van Hulst, New Journal of Physics **10** (2008).

[54] H. Gersen et al., Physical Review Letters **85**, 5312 (2000).

[55] R. J. Moerland, T. H. Taminiau, L. Novotny, N. F. Van Hulst, and L. Kuipers, Nano Letters **8**, 606 (2008).

CHAPTER 3

EXPERIMENTAL SETUP

The use of our near-field microscope requires expertise in several different areas and involves many experimental details. First, the user must be an expert in the operation of the Atomic Force Microscope (AFM). Second, there are various ways in which the optical setup can can be configured, each of which can alter the physics of the near-field interaction. Finally, the optical data are acquired by home-written software designed for maximum capability and flexibility in both hardware and software and there are a number of different data analysis techniques which have evolved over the years. Thus, the user must understand the operation of the data acquisition software and hardware, and recognize the advantages and limitations of the postanalysis algorithms.

In this chapter, the basic layout of the near-field microscope is described and the different illumination schemes are summarized. The basic physics of an AFM microscope is also examined by modeling the AFM as a simple harmonic oscillator. The operation of the AFM probe, which is relevant to the data acquisition and analysis, is reviewed. The last section of the chapter focuses on the basic techniques used to produce a near-field optical signal and the advantages of using single-photon sensitive detection. The subsequent chapters review the experimental results using the single photon sensitive detection scheme; most of these results would not be possible without our unique data acquisition scheme. Since much of my effort has been focused on setting up the data acquisition and postprocessing software, I will touch briefly on the capabilities of the technique in this chapter.

The main intent of this chapter is to introduce the reader to some of the technical details and considerations along with some basic theoretical concepts important to

the experimental setup. For a person familiar with Near-field Scanning Optical Microscopy (NSOM), this chapter should provide a review of important experimental considerations. For a person who is new to NSOM, this chapter along with Ref. [1] and the AFM manual should provide a good technical background.

3.1 Basic setup

Our near-field scanning optical microscope is comprised of two essential parts: an Atomic Force Microscope (AFM) and an inverted confocal microscope. Figure 3.1 depicts the basic layout of the setup. A laser is coupled to an optical fiber via a fiber coupler. The output of the coupler is magnified to the desired size by a simple two lens beam expander. The expanded beam goes through a half wave plate which enables control of the polarization. Typically one of following three focused illumination types is used: evanescent, radial, or Gaussian. Each has its own advantages and disadvantages as will be discussed in Sec. 3.2. For radial and evanescent illumination, the beam is sent through a beam mask. The excitation beam is then reflected by a dichroic mirror onto a scanning mirror. Excitation light is then focused by a high numerical objective (NA = 1.4) onto the sample surface. Emitted light is collected by the same objective and directed onto an avalanche photodiode (APD) via the scanning mirror, a steering mirror and a focusing lens. The 1:1 telescope and scanning mirror de-scan scheme to ensure alignment with the APD during movement of the scanning mirror. To ensure that only the emission light is detected, an emission filter is positioned right before the APD and the focusing lens to reject scattered light wavelengths.

The AFM sits on top of the inverted confocal setup. For regular imaging the sample is scanned laterally via a piezo actuator while the AFM head and the microscope objective are stationary. In order to achieve a near-field signal, the AFM tip must be aligned within the laser's focal spot. The scanning mirror plays an important role since it allows movement of the excitation beam independently from the AFM and is therefore used for tip-laser alignment.

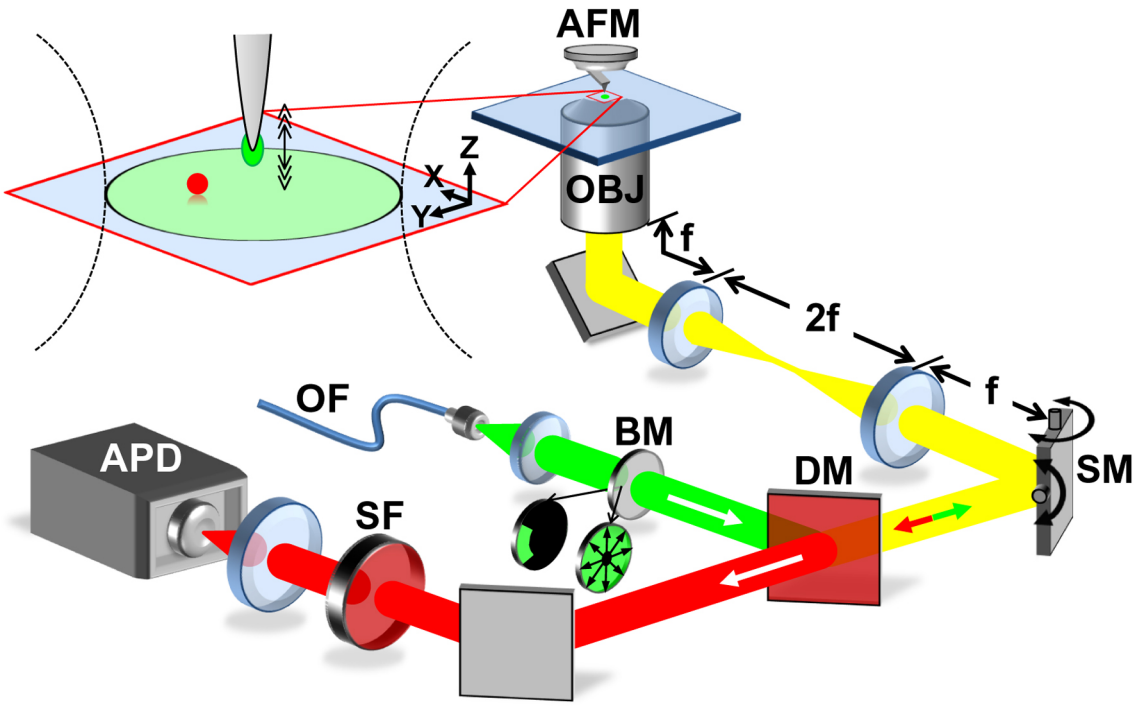

Figure 3.1. Schematic of experiment. A laser beam is directed through a beam mask (BM), producing either a radially polarized laser beam or a 60° section (wedge) of an annular beam. A microscope objective (OBJ: NA = 1.4) focuses the laser beam and collects emitted fluorescence, which is focused onto an avalanche photodiode (APD). The laser focus is positioned onto an AFM tip using a scanning mirror (SM). The sample is raster-scanned laterally, where by convention the X-axis corresponds to the fast-scan direction. The inset shows the tip-sample interaction region in more detail. Other important components include an optical fiber (OF), a dichroic mirror (DM), and a spectral filter (SF). Reprinted with permission from [2]. Copyright 2009 American Chemical Society.

3.2 Types of illumination

The excitation light plays a crucial role in near-field microscopy. Most important is the ability to control the polarization of the light at the laser focus; light polarized along the axis of the AFM tip typically results in strong field enhancement at the tip apex while light polarized perpendicular to the tip axis does not (and might even result in a reduction in the field intensity). Other parameters, such as the beam waist and the point spread function (PSF) at and above the sample, can also alter the resulting near-field optical signal. In our experiments we typically use one of

three types of illumination conditions: Gaussian excitation, radially polarized light and total internal reflection (TIR) that results in an evanescent illumination.

3.2.1 Gaussian illumination

The output of a laser beam is typically specified by a TEM_{mn} mode, where TEM stands for Transverse Electric and Magnetic. The lowest mode, TEM_{00}, results in a Gaussian beam profile. Moreover, the output light is typically strongly polarized along a particular axis (i.e., linearly polarized). This illumination mode is the most commonly used type of excitation in microscopy and most commercial lasers operate in this mode. Therefore, to achieve this type of illumination condition is rather straightforward.

In our setup, a TEM_{00} laser light is coupled to a polarization maintaining single mode optical fiber which preserves the polarization of the Gaussian light. After the light is focused by the objective, this illumination scheme results in horizontally polarized light at the center of the focus (Fig. 3.2a). Adjacent to the center of the focus, the light polarization is no longer perfectly horizontal. Following Ref. [3], for a linearly polarized Gaussian beam focused by a high numerical aperture lens, the different electric field components at the focal spot can be found. Figure 3.3 shows the

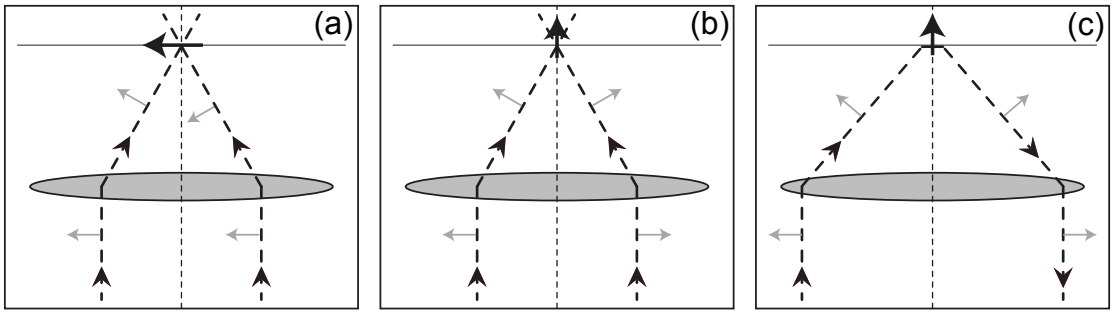

Figure 3.2. Illustration of the different illumination conditions. (a) Gaussian illumination results in horizontal polarization at the focus. (b) Radially polarized light yields vertical polarization at the focus. (c) By letting in only critical rays from one side, TIR yields an evanescent wave, which can also result in vertical polarization. Notice that in (c), the incoming light is illustrated on the left side and the reflected light is on the right.

results of the intensities for the different field components (i.e., $|E_x|^2$, $|E_y|^2$, $|E_z|^2$). For this calculation, it is assumed that the beam waist perfectly fills the back aperture of an objective with NA = 1.4, $n = 1.518$ (immersion oil/glass) and the incident light is polarized along the x axis. Notice that the field component that corresponds to the initial polarization of the light is much stronger than the other components (256 and 8 times greater than the y and z components, respectively). Therefore, for a sample which does not have a particular dipole orientation (e.g., a collection of randomly oriented molecules), the far-field emission will look similar to $|E_x|^2$ which has a slightly elongated Gaussian profile in the direction of the polarization [3–5]. The measured beam profile for 20nm fluorescence beads can be seen in Fig. 3.4a. The characteristic decay length of the light intensity above the sample (i.e., Rayleigh length) is typically a few μm.

Although this is the easiest illumination condition to achieve, it is rarely used because the horizontal polarization at the focus does not result in any field enhancement at the apex of the tip.

3.2.2 Radial illumination

One way to achieve vertical polarization at the focus is to use a radially polarized light. Radially polarized light is a superposition of TEM_{10} laser mode with the same

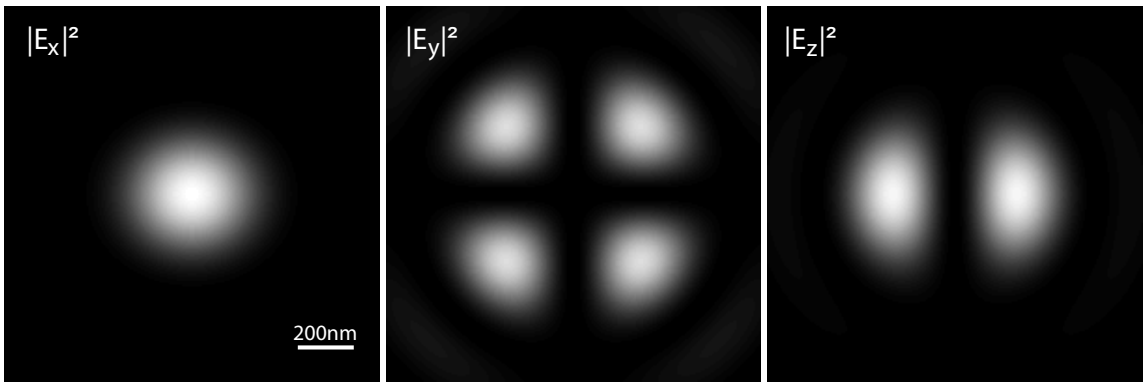

Figure 3.3. Gaussian beam at the focus. The intensity of the different electric field components is plotted. The intensity scale for the $\hat{y}$ and $\hat{z}$ components were magnified by 256 and 8, respectively. The incident polarization before focusing is along $\hat{x}$.

mode rotated by 90° [5]. When a radial excitation profile is focused by the objective, the horizontal components of the electric field will cancel each other out to some degree, thus creating light with mostly vertical polarization (Fig. 3.2b). To the side of the focus, the strength of the horizontal components increases and the strength of the vertically polarized light components is reduced. The actual field components for radially polarized light can also be computed using Ref. [3] (Appendix D). The vertical-polarization part of beam profile at the focus for this mode is well described by a Gaussian (Fig. 3.4b). In fact, the focal spot is tighter for radial excitation by nearly 40% in comparison to the Gaussian excitation [5, 6].

In practice, the radially polarized light is created through a commercial device (Arcoptix) using twisted nematic crystals. The output signal from the crystal can be spatially filtered by passing the beam through a pinhole which results in a high quality radially polarized light.

3.2.3 TIR illumination

When a light beam is incident on an interface between two different mediums, the reflected and transmitted light behaves according to Snell's law. Above some critical incident angle, the light is totally internally reflected at the incident medium and strongly decays above the interface. It is therefore important to consider the size of a beam waist before it enters the objective. The combination of a high numerical aperture objective ($NA = 1.4$) with a glass/air interface at the sample results in some TIR light. Using Snell's law:

$$n_1 \sin\theta_1 = n_2 \sin\theta_2 \tag{3.1}$$

At the critical angle the equation reduces to

$$\sin\theta_c = \frac{n_2}{n_1} \tag{3.2}$$

The diameter of the back aperture of the microscope objective is given by [8]

$$D = \frac{2\mathrm{NA} f_{TL}}{M_{ag}} \tag{3.3}$$

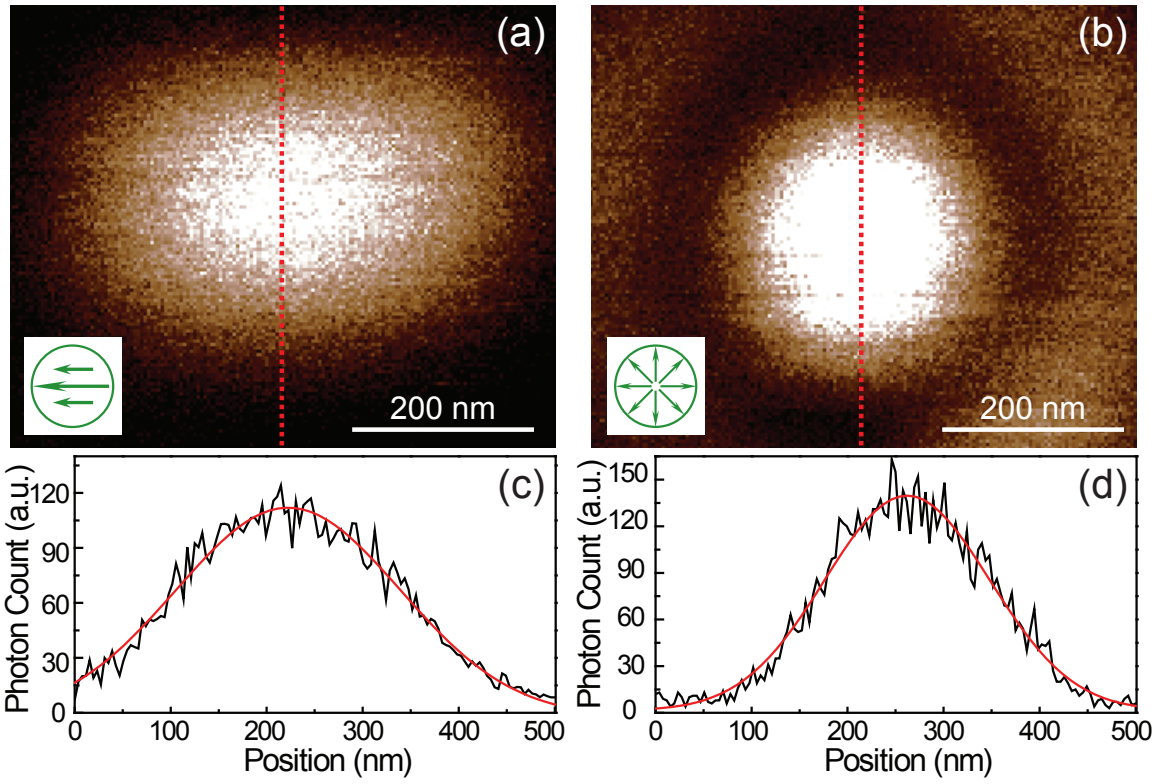

Figure 3.4. Beam profiles at the focus. Far-field scanned images of fluorescence beads. (a) The Gaussian beam focuses to a Gaussian profile. The light focuses to a larger spot at the polarization axis. (b) Radial polarization results in a symmetric focal spot. The beam focus is slightly tighter than the Gaussian beam. Reprinted with permission from [7] (© 2008 IEEE).

where f_{TL} is the focal length of the tube lens and M_{ag} is the magnification of the microscope's objective. The diameter at the critical angle can be obtained using equations 3.2, 3.3 and the relation NA $= n_1 \sin\theta$ to give:

$$D_c = \frac{2n_2 f_{TL}}{M_{ag}} \tag{3.4}$$

For a Nikon objective with $M_{ag} = 100$, NA=1.4, $n_1 = 1.518$, $n_2 = 1$ and $f_{TL} = 200$ mm, the back aperture and the critical diameter are 5.6 mm and 4 mm, respectively. Thus, the parts of a beam with a diameter larger than D_c will be totally internally reflected. The critical angle can be calculated via Eq. 3.2 to be $\theta_c = 41.8°$.

The incident light can be described by a plane wave: $\vec{E} = \vec{E}_1 e^{i(\vec{k}_1 \cdot \vec{r} - \omega t)}$. The

electric field can be separated to s-polarized (parallel to the interface) and p-polarized (perpendicular to the interface) components

$$\vec{E}_1 = \vec{E}_1^{(s)} + \vec{E}_1^{(p)} \tag{3.5}$$

When light hits an interface at an angle larger than the critical angle, the z component of the wavevector $\vec{k}$ becomes imaginary. Figure 3.5a illustrates a case of a plane wave impinging on a flat interface with an incidence above the critical angle ($\theta_1 > \theta_c$). The transmitted electric field in this case can be expressed as [3]:

$$\vec{E}_2 = \begin{bmatrix} -iE_1^{(p)} t^p(\theta_1) \left(k_2 z_0\right)^{-1} \\ E_1^{(s)} t^p(\theta_1) \\ E_1^{(p)} t^p(\theta_1) \left(k_2 z_0\right)^{-1} \sqrt{1 + \left(k_2 z_0\right)^2} \end{bmatrix} e^{i \sin\theta_1 k_1 x} e^{-z/z_0} \tag{3.6}$$

where t^p is the Fresnel coefficient for p-polarized light, k_1 is the wavevector in the incident medium, $\tilde{n} = \frac{\sqrt{\epsilon_1 \mu_1}}{\sqrt{\epsilon_2 \mu_2}}$ is the relative index of refraction with ϵ_1 and ϵ_2 being the permittivity of the incident and transmitted medium, respectively. The magnetic permeability is assumed to be unity for both mediums. The decay length z_0 is defined by

$$z_0(\theta_1) \equiv \frac{1}{k_2 \sqrt{\tilde{n}^2 \sin^2\theta_1 - 1}} \tag{3.7}$$

where k_2 is the wavevector in the transmitted medium.

Two important observations can be made from this derivation. First, an exponentially decaying (evanescent) electric field is established above the interface, which results in a tightly confined excitation. For the case of a glass/air interface ($\epsilon_1 = 2.25$, $\epsilon_2 = 1$) and an incidence angle of $\theta_1 = 45°$ the decay length is: $z_0 = \frac{\lambda}{2.22}$. For Gaussian and radial illumination, the intensity of the excitation light decays on a typical length scale of about a few μm above the focus (i.e., Rayleigh range). In comparison, the intensity of the laser in the case of evanescent illumination decays to $1/e$ after a few hunderd nm (assuming visible illumination wavelength). Second, the light polarization above the interface is easy to manipulate via the incident light polarization. If the incident light is s-polarized (i.e., $E_1^{(p)} = 0$), then the x and z components of the transmitted electric field disappear (Eq. 3.6), thus, creating s-polarized light above the interface. If the incident light is p-polarized,

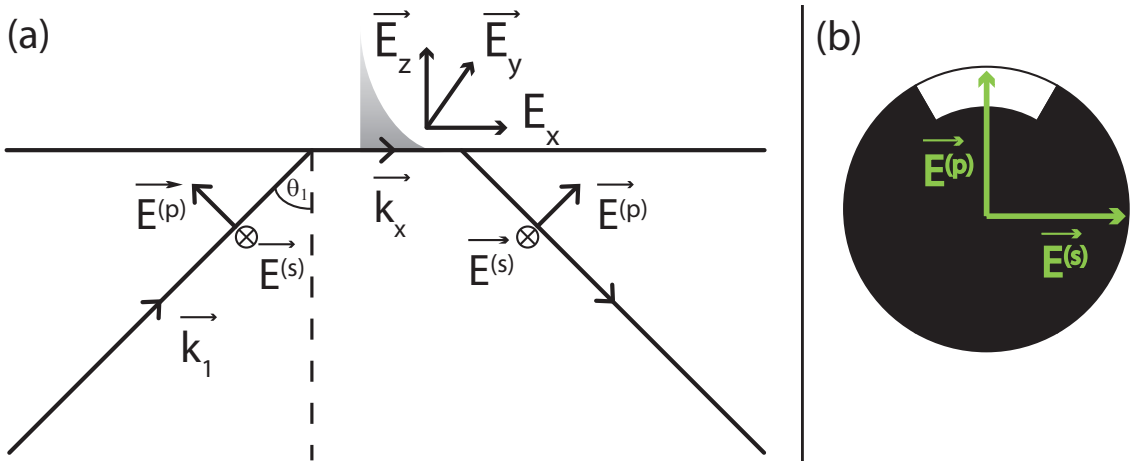

Figure 3.5. Total internal reflection. (a) An incident light above the critical angle results in total internal reflection. Above the interface the light decays exponentially along the z axis. This is called an evanescent field. (b) An illustration of the beam mask which is being used to create the TIR illumination. The polarization of the incidence field determines the polarization of the light at the focus.

the light above the interface will have both s-polarized and p-polarized components with the p-polarized component always being stronger. Notice that the decay length, the amplitude, and the ratio between the different amplitude components of the transmitted field depend on the incident angle θ_1. For a case of NA=1.4, a glass/air interface and a beam waist similar or larger in size than the back aperture, there will be a distribution of incidence angles between $41.8° < \theta_1 < 69.0°$.

To create an evanescent illumination we use a Gaussian beam and an opaque (metal) screen with a wedge-shaped window. This mask blocks all the light except the supercritical rays, namely those light rays that enter the back aperture of the microscope objective at a diameter smaller than D_c. The wedge-shaped mask is illustrated in Fig. 3.5b. The green arrows in Fig. 3.5b represent the polarization of the incident light. The 60° opening ensures that the oppositely directed vertical vector components originating from opposing sides of the beam do not cancel each other at the focus. An example of such a case is illustrated in Fig. 3.2a where the vertical component of the light coming from the left and the right cancel the vertical component at the focus. The wedge shape also suppresses the horizontal components

passing through the wedge. A bigger opening angle results in more s-polarized light.

3.2.4 How to choose the illumination condition

The ideal choice of an illumination condition depends on the particular experiment. Gaussian illumination can be used if vertical polarization is not a necessity (for example see Chap. 6). The main advantage of the Gaussian illumination is that it is easy to set up. For any other experiment, either radial polarization or TIR illumination should be used. The TIR scheme enables fast switching between horizontal to vertical polarization and vice versa. On top of that, the beam size in the case of TIR is elongated along one dimension, which makes it is easier to align the tip into the laser spot. The evanescent wave resulting from the TIR configuration, decays quickly above the sample surface. Therefore, scattering of excitation from the tip will be reduced in comparison to Gaussian and radial polarization. The reduced scattering also results in interference effects (Sec. 2.2.4) which are confined to short tip-sample vertical distance. This results in easier determination of where the far-field region starts (i.e., where the tip has no effect on the signal). On the other hand, when measuring high density samples, a larger laser spot will result in increased background and therefore reduced contrast [9]. In such a case, it is advantageous to use radial polarization due to the reduced laser spot at the focus. Radial polarization should also be used when imaging thick samples. The fast decay of the TIR illumination above the sample will result in excitation of only the lower part of the sample. Table 3.1 summarizes the conditions in which each illumination configuration should be used.

Table 3.1. How to choose the illumination condition.

Illumination condition:	When to use:
Gaussian	No need for vertical polarization.
Radial	High density sample and/or thick sample.
TIR	All other.

3.3 Atomic Force Microscope (AFM)

In NSOM, the ability to scan a surface accurately with minimal damage to the sample is highly desired, while the main physical quantity of interest is the optical scattering signal. In order to prevent near-field optical artifacts or misinterpreted data, it is important to understand the advantages and limitations of different scanning techniques.

The AFM used in our lab is a commercial microscope (Asylum Research), which comes with its own software (Igor Pro). The AFM consists of a few important parts: a very precise piezo actuated scanning stage, AFM head, AFM control box and a cantilever with a sharp probe at its end. The scanning stage is used to scan the sample laterally (i.e., $X-Y$). The cantilever is attached to the AFM head which controls the vertical motion of the tip. The AFM head itself consists of a few mechanical and optical components which keep the tip moving in the desired motion while scanning the surface. All the signals end up in the AFM control box where the signals are filtered and recorded on the computer. Access to real time signals is available through the control box. The most important signal regarding the optical measurements is the deflection signal which provides information on the vertical motion of the tip (see Appendix E).

Typically the scanning techniques used in AFM can be separated into an intermittent mode (tapping) and a contact mode, although in our lab we exclusively use *tapping* mode. In this mode, the tip oscillates vertically and only intermittently touches the sample. Tapping mode holds a few main advantages over contact mode: it reduces damage to the sample because the contact is only intermittent, large amplitude oscillation are sometime desired to achieve higher optical contrast [9] and it allows us to obtain vertical tip-sample distance dependent statistics in an elegant way. During a typical near-field experiment, the sample can either be raster scanned or the $X-Y$ scan can be halted while the tip maintains its vertical Z oscillations above a specific chosen location in the sample.

3.3.1 Simple Harmonic Oscillator (SHO)

As mentioned above, the probe will oscillate in a typical distance-control system. The AFM's driving signal is harmonic, and for the most part, so is the actual motion of the tip (especially when imaging in air). It is therefore beneficial to model the oscillations of the tip as a Simple Harmonic Oscillator (SHO) [10]. This simple, approximated model gives valuable insight into the physics involved. Within this model, the motion of the tip can be approximated by the following equation:

$$m\ddot{z} + \kappa z + \frac{m\omega_0}{Q}\dot{z} = F_{ts} + \kappa A_d \cos(\omega t) \tag{3.8}$$

where κ is the spring constant of the AFM cantilever, m is the mass of the cantilever, ω_0 is the resonance frequency, Q is the quality factor of the oscillator, F_{ts} is the net tip-sample force, A_d and ω are the amplitude and the angular frequency of the driving force and z is the distance between the tip and the sample. The tip-sample forces are usually approximated to first order, and their contribution can be included as an effective spring constant

$$\kappa_{\text{eff}} = \kappa - \frac{\partial F_{ts}}{\partial z} \tag{3.9}$$

The resonance frequency of the probe then becomes $\omega_e = \sqrt{\frac{\kappa_{\text{eff}}}{m}}$. By assuming a solution of the form: $z(\omega) = A(\omega)\cos(\omega t + \phi(\omega))$, the steady state amplitude and phase can be easily found:

$$A(\omega) = \frac{A_d\omega^2}{\sqrt{(\omega_e^2 - \omega^2)^2 + \frac{\omega^2\omega_e^2}{Q^2}}} \tag{3.10}$$

$$\tan(\phi) = \frac{\omega_e\omega}{Q(\omega_e^2 - \omega^2)} \tag{3.11}$$

These simple solutions are fundamental for the understanding of the operation of the AFM tip. Any changes in the gradient in the tip-sample interaction forces $\frac{\partial F_{ts}}{\partial z}$ lead to a change in the effective spring constant (Eq. 3.9) therefore shifting the actual resonance frequency of the tip, ω_e. This in turn leads to variations in both the amplitude and the phase. Therefore, any of the three values, ω_e ,$A(\omega)$,$\phi(\omega)$, can be used as a feedback loop.

In our setup, the feedback loop detects changes in the oscillation amplitude and reacts by changing the position of the tip above the sample to ensure constant amplitude throughout a scan. Important physical information can be extracted from these three channels, and all three data sets should be recorded during an experiment.

3.3.2 Repulsive vs. attractive imaging

Tip-sample forces are also essential for understanding the different operating modes. The Leonard-Jones potential qualitatively describes the repulsion between the sample and tip at short distances and their mutual attraction at longer distances via van der Waals forces. In tapping mode, the AFM can be operated in two different tip-sample interaction regimes called repulsive and attractive modes. The main difference between the two is that the cantilever is given enough energy to overcome the attractive tip-sample forces in the repulsive mode but not in the attractive mode. As a consequence, the cantilever will touch the sample in the repulsive mode but typically stay a few nm away from the sample in attractive mode.

It is very important to know which force regime is dominant for any particular experiment. Figure 3.6 is an illustration of the amplitude and phase (Eq. 3.10 and Eq. 3.11) signals for realistic tip parameters. In this example, the tip's operating frequency is set to be at ω_0 (vertical black line). This is the tip's natural resonance in the absence of any tip-sample interactions (i.e., $F_{ts} = 0$). This is a realistic scenario when the tip is sufficiently far from the surface. The amplitude and phase for this case are plotted in black. As the tip is lowered to the surface, if the repulsive forces are dominant, the effective resonance frequency ω_e becomes larger, effectively shifting both the amplitude and the phase to the right (dotted red line). As a consequence, the phase drops below 90° and the cantilever is driven at a frequency ω below the new resonance frequency, ω_0'. These are indicators of operating in the repulsive regime. In the attractive regime, ω is above the resonance ω_0' and ϕ is larger than 90° as demonstrated by the blue lines. Therefore, we can determine which forces are more dominant during a measurement by inspecting the direction of the phase shift.

The user does have some control of the imaging mode. Operating at lower oscillation amplitudes and using stiffer tips with bigger radii can increase the success

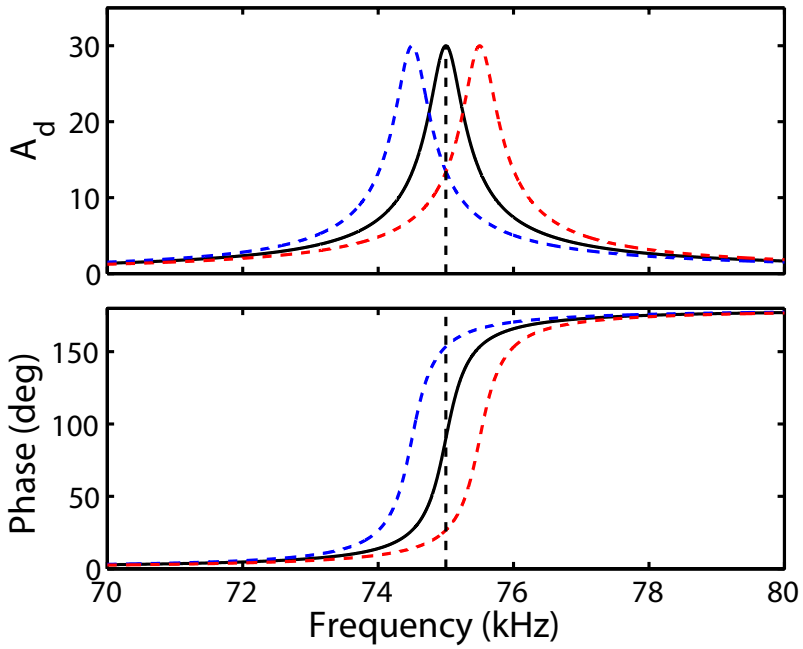

Figure 3.6. AFM amplitude and phase signals. The black curves are the amplitude (a) and phase (b) signals plotted for typical tip values following equations 3.10 and 3.11. The dotted black line depicts the resonance frequency for no tip-sample interactions. Attractive tip-sample interactions result in lower effective resonance frequency (dotted blue curves) while repulsive interactions have a higher effective resonance (dotted red curves).

of operating in attractive mode. This mode is indeed best for minimizing shear forces on the sample. However, the repulsive mode yields better topography tracking. In addition, in order to demodulate the signal into the far-field, as discussed in Ref. [9], it is sometimes necessary to operate in repulsive mode.

3.3.3 Making carbon nanotubes tips

CNTs are grown on oxidized silicon substrates using methane-based chemical vapor deposition (CVD) and ferric nitrate catalyst nanoparticles (Appendix G). The growth recipe adopted has been shown to produce mostly single-wall CNTs of both semiconducting and metallic chiralities [11, 12]. Following growth, CNT substrates are imaged with the AFM using gold-coated probes, and vertically oriented CNT whiskers can be lifted off the substrate by adhering to the sidewalls of the AFM probe. The mechanistic details of the pickup process are not fully understood, although

experimental and theoretical studies suggest that relatively large diameter CNTs (3 - 5 nm) are more likely to attach due to the increased CNT-probe interfacial area [12, 13].

The two main indicators that a CNT has been picked up by the tip are a change in the topography image resolution while scanning (Fig. 3.7a) and a phase change (Fig. 3.7b). Long CNTs have a tendency to buckle under large compression and also exhibit large vibration at the distal end. Thus, a change in the scanning resolution can either be for the better (if a short CNT was picked up) or worse. As mentioned above, the phase signal reflects on the tip-sample interaction forces. Once the CNT has been picked up, the tip-sample interactions are drastically modified leading to a substantial shift in the phase. The large shift in the phase is an excellent contrast mechanism and it is usually easier to detect CNT pickup using the phase image. To reduce the chances of multiple CNT pickup, the scan needs to be stopped as soon as a CNT has been picked up.

Following pickup, the CNT length is measured by pressing the CNT against a smooth Si substrate while measuring the deflection of the AFM cantilever (force curve). When the distal end of the CNT touches the substrate, the cantilever initially begins to deflect. As more force is applied, the CNT will elastically buckle and the cantilever deflection relaxes somewhat resulting in a kink in the approach curve.

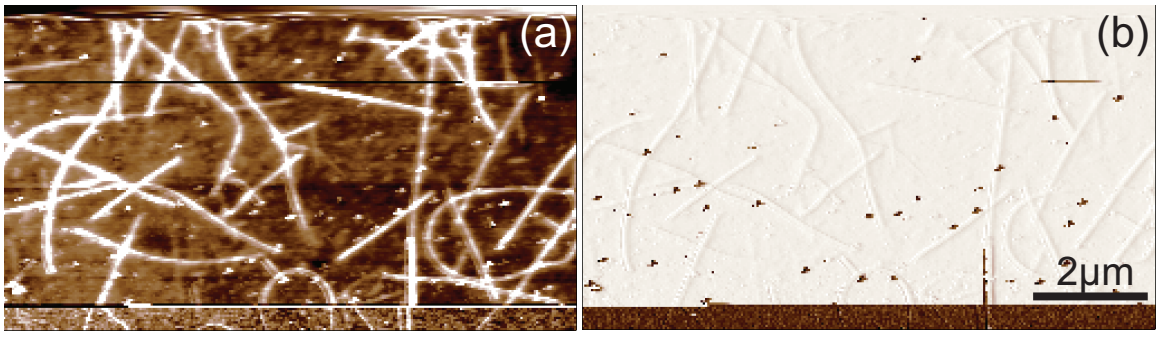

Figure 3.7. AFM scan of a CNT wafer. (a) Height topography. (b) Phase signal. Once a CNT has been picked up, as can be seen at the bottom of the images, both the height and phase images change. Reprinted with permission from [7] (© 2008 IEEE).

Depending on its length, a number of additional kinks are possible until finally the apex of the AFM probe comes into contact with the substrate after which a linear deflection of the cantilever is observed as the tip is further pressed into the substrate. The measured distance between the first kink and the linear onset gives the CNT length. Figure 3.8b is an example of two AFM force curves for a long (red curve) and short (blue curve) CNT. In theory, the length of the CNT can be determined by SEM imaging (Fig. 3.8a). However, this is a time consuming process and can also leave carbon deposits on the CNT.

When initially attached, CNTs are generally too long to possess sufficient axial stiffness for use in AFM imaging and thus they must be shortened to <200 nm. This is achieved by application of short ($\sim$10 μs) voltage pulses of 10 V amplitude between the AFM probe and a conductive substrate. These pulses induce electrochemical etching of the distal end of the CNT, which leads to shortening in quasi-controllable steps of 10-15 nm and removes any fullerene or catalyst cap.

3.4 Producing a near-field signal

To record the measured signal we utilize a single-photon detection technique. Every photon that is detected contains several pieces of information. Most impor-

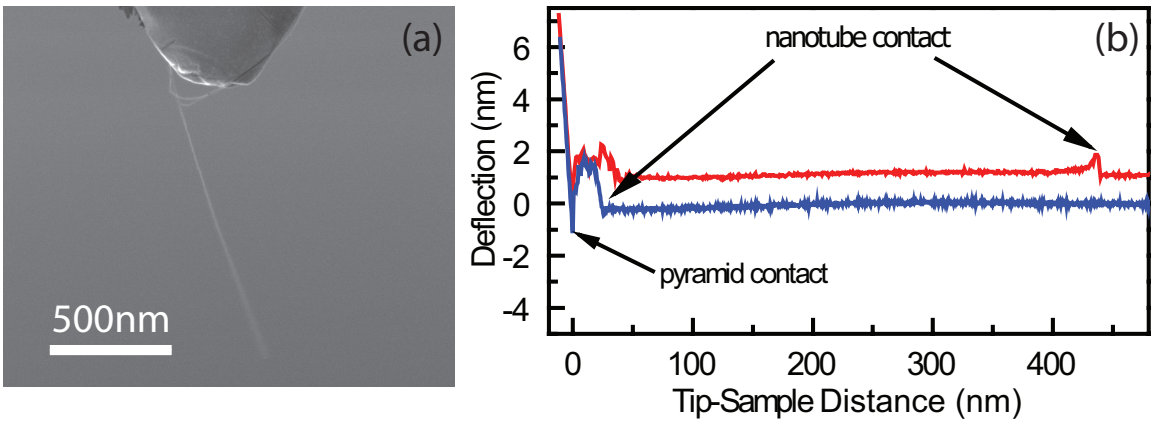

Figure 3.8. SEM image of CNT tip and Force curves to determine the length. (a) An SEM image of a CNT tip. After pickup the CNT are generally too long to be used and need to be shortened. (b) Force curves determine the CNT length before (red) and after shortening (blue). Reprinted with permission from [7] (© 2008 IEEE).

tantly, the position of the AFM tip is calculated at the time of emission of each photon collected. All of the information is stored on the computer which enables application of any algorithm on the data and therefore this technique allows for maximum flexibility in the post-analysis. This detection method is based on the technique used by Gerton et al. [14] with the addition of a few new features.

3.4.1 Approach curve

The most basic form of near-field data taken in our lab is called an *approach curve* where the sample's movement in the lateral $X-Y$ plane is halted and the tip oscillates vertically above the sample. To record the signal from the AFM, the deflection signal (Appendix E) is first converted from an analog signal to a TTL-compatible signal by a simple electronic circuit (Appendix F). The resulting TTL signal is then used to generate time stamps using a Data Acquisition Card (DAC) by a technique called period measurements or edge detection. The tip-ocsillation TTL signal will be referred to as the "tapping" signal. The APD generates a TTL pulse for each photon detected which is also time stamped by the same DAC used to record the tapping signal. It is important that the two signals (tapping and photon) are recorded by the same card to insure synchronization in time. A time delay (Δ) between the arrival time of each photon and the preceding probe-oscillation time stamp is computed and converted to a phase delay in the post analysis. The data acquisition procedure is illustrated in Fig. 3.9.

The phase delay values are tabulated into a histogram of phase delays as shown in Fig. 3.10a. The phase corresponding to minimal tip-sample distance (Δ_0) can be found if some knowledge about the near-field signal exists *a priori*. For example, silicon tips typically enhance the signal and therefore Δ_0 should be located at the center of the enhancement peak (dashed gray line in Fig. 3.10a). The phase delays are converted into a tip-sample distance z by assuming harmonic probe oscillation $z = A\,[1 - \cos(\Delta - \Delta_0)]$ where A is the tip's oscillation amplitude (not peak to peak amplitude!). This analysis yields a tip-sample distance dependent signal which we refer to as an *approach curve* (Fig. 3.10b). This is the basic data acquisition technique

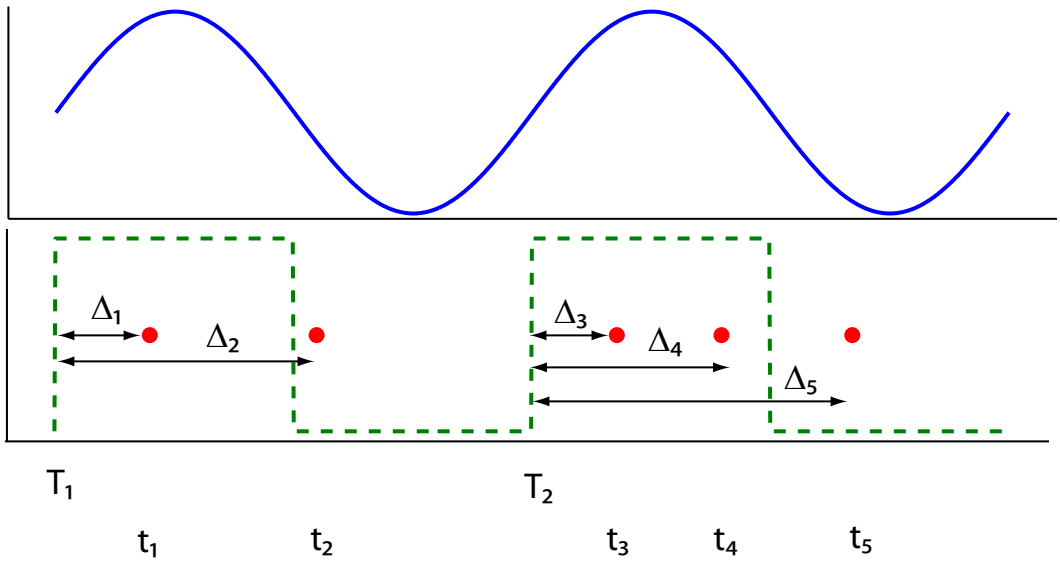

Figure 3.9. Data acquisition procedure. The deflection signal from the AFM (blue line) is converted to a digital signal (dashed green line) which is then time stamped (depicted by T_i). Each photon (red circles) is also time stamped (t_i). For each photon recorded, a phase delay between the photon arrival time and the preceding tapping signal is computed in the post analysis. Thus, for each photon we now have an absolute arrival time and a phase delay which will later be converted to tip's height.

used in our lab and is implemented in almost every type of experiment.

In the case of anharmonic tip oscillations (typical for water scanning), instead of converting the deflection signal into a TTL, the deflection signal can be recorded by an analog to digital converter with a high sampling rate (1MHz). It is then possible to correlate the height of the tip with the photon time stamp by directly comparing the deflection signal (blue curve in Fig. 3.9) with the time stamp of each photon (red circles in Fig. 3.9).

3.4.2 Single Photon Near-Field Tomography (SP-NFT)

The approach curve can be easily extended to a full 3D tomography map of probe-sample interactions [2]. In this acquisition mode, the sample is raster scanned in the $X-Y$ plane while the tip oscillates vertically. Every time the sample scanner advances a line, a signal marker is generated and time stamped by the same DAC used to record the approach curve. This enables us to correlate each approach curve with

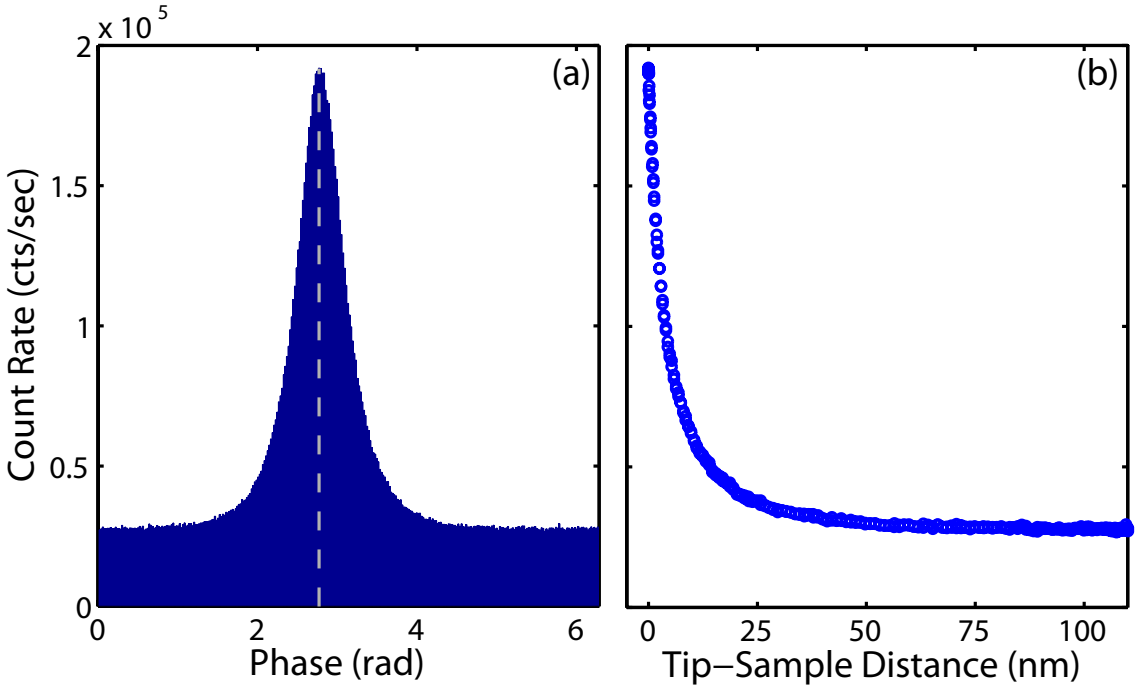

Figure 3.10. Phase histogram. (a) The phase delays (Δ_i) are accumulated into a histogram. Each phase reflects a different tip-sample separation distance. (b) Once the minimal tip-sample distance is found (dashed gray line), i.e., Δ_0, the phase histogram can be transformed to a distance dependent curve by assuming harmonic tip oscillation.

the $X - Y$ position of the scanning stage. This results in a two-dimensional array of vertical approach curves, representing a three-dimensional map of the near-field coupling between the tip and the sample. The topography, which is stored by the AFM software, can be overlaid with the optical image to give a complete picture of the probe-sample interactions. This should be done carefully as one needs to ensure that the topography and optical images are time-correlated with each other. This can be done because the photon data are recorded twice: once with the AFM software and once with the DAC card. Therefore, by correlating the two photon channels, one can correlate the optical data recorded by the SP-NFT method with any of the channels recorded by the AFM.

3.4.3 Fluorescence lifetime data

All the analysis mentioned above can be done in addition to tip-sample distance dependent lifetime measurements [15, 16] by using standard time-correlated single-photon counting (TCSPC) hardware and a pulsed laser. In this method, like before, the probe oscillation needs to be converted into a digital wave. An explanation of how the TCSPC hardware works can be found in the TSCPC card manual. Briefly, the edge separation time (τ_i) between an input channel (photon signal) and a sync channel (corresponding to the laser pulse) is recorded by the TCSPC card. This is done by triggering a time measurement that begins when a photon arrives and stops when the next sync signal arrives. The TCSPC card we use in the lab (picoQuant TimeHarp 200) can record data in a Time-Tagged Time Resolved Measurement (TTTR) mode. In this mode, each photon's fluorescence lifetime (τ_i) and absolute arrival time (t_i) are recorded. The tapping signal and the line markers can be recorded and time stamped as external markers on the card. Therefore, we have all the information that was available to us in the previous measurement techniques with the addition of time resolved fluorescence lifetime data for each photon.

Table 3.2 summarizes the information which is contained for each photon detected. To create an actual tip-sample distance dependent lifetime curve, the data are first analyzed into a phase histogram. The time resolved fluorescence lifetime data points within a bin are converted into a histogram of number of photon arrivals per lifetime bin as can be seen in Fig. 3.11a. This histogram represents the probability of fluorescence lifetime decay for a particular tip-sample distance. A single characteristic decay time is obtained by fitting the measured probability function with an expected probability distribution. Typically the data are fitted to

$$P(\tau) = Ae^{-\tau/\tau_0} \tag{3.12}$$

where A is the amplitude and should correspond to the number of photon arrivals at $\tau = 0$ and τ_0 is the characteristic decay time. The process described above is repeated for all the phase histogram bins. In Fig. 3.11a three different bins are shown, which correspond to different tip-sample distances. The results of τ_0 as a function of tip-sample distance are shown in Fig. 3.11b.

Table 3.2. Information contained in each photon. Each photon contains an absolute arrival time, fluorescence lifetime and phase delay which can converted to tip-sample separation distance.

Photon #	Absolute time	Fluorescence lifetime	Phase delay	Tip-sample Distance
1	t_1	τ_1	Δ_1	z_1
2	t_2	τ_2	Δ_2	z_2
N	t_N	τ_N	Δ_N	z_N

The black curve in Fig. 3.11a is the experimentally measured Instrument Response Function (IRF). The IRF is a reflection of the timing uncertainty of the TCSPC measurements. The most critical component for IRF broadening is the photon detector (in our case the APD). The other important sources are the pulse width of the excitation source and timing jitter in the electronics of the TCSPC. The IRF puts a limitation on the lifetimes that can be recorded by the setup. If the lifetimes recorded are much larger than the IRF, the error introduced to the data is negligible.

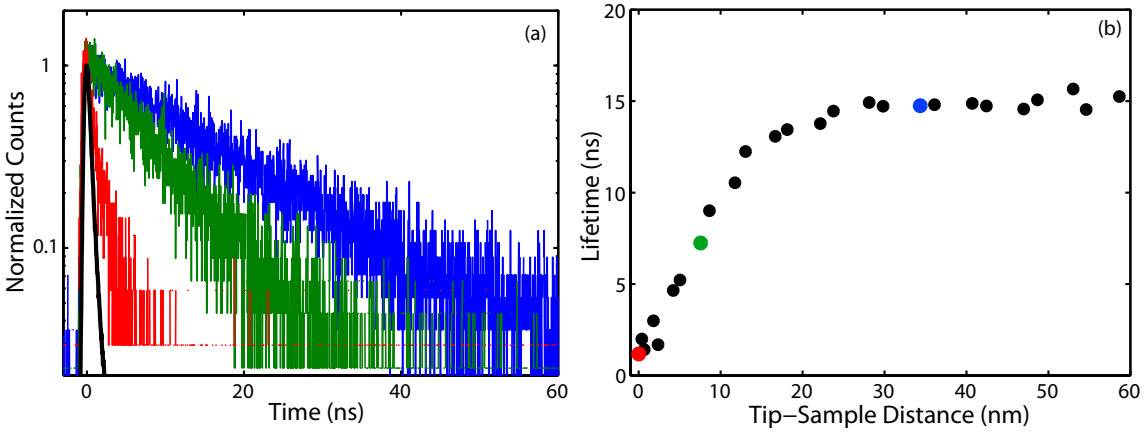

Figure 3.11. Creating a tip-sample distance dependent lifetime curve. (a) The three different curves (blue, green and red) represent the probability of fluorescence lifetime decay for different tip-sample distances ($z = 34\text{nm}, 7\text{nm}, 0\text{nm}$ respectively). The black line is the measured IRF. (b) Measured fluorescence lifetime as a function of tip-sample distance. The colored points correspond to the probability distributions in panel (a).

On the other hand, once the measured lifetime starts being comparable to the IRF, the error in the data is too big and iterative convolution is usually used to separate the two.

3.5 References

[1] B. D. Mangum, *Exploring the limits of near-field fluorescence microscopy: Toward molecular-scale imaging of biological systems*, PhD thesis, University of Utah, 2010.

[2] B. Mangum, E. Shafran, C. Mu, and J. Gerton, Nano Letters **9**, 3440 (2009).

[3] L. Novotny and B. Hecht, *Principles of Nano-Optics*, University Press, Cambridge, 2006.

[4] M. Born and E. Wolf, *Principles of Optics: Electromagnetic Theory of Propagation, Interference and Diffraction of Light*, Cambridge University Press, New York, seventh edition, 2002.

[5] S. Quabis, R. Dorn, M. Eberler, O. Glckl, and G. Leuchs, Optics Communications **179**, 1 (2000).

[6] R. Dorn, S. Quabis, and G. Leuchs, Physical Review Letters **91**, 233901 (2003).

[7] C. Mu, B. D. Mangum, C. Xie, and J. M. Gerton, IEEE Journal of Selected Topics in Quantum Electronics **14**, 206 (2008).

[8] G. H. Seward, *Optical Design of Microscopes*, SPIE, Bellingham, Washington, 2010.

[9] B. D. Mangum, C. Mu, and J. M. Gerton, Optics Express **16**, 6183 (2008).

[10] R. Garcia and R. Perez, Surface Science Reports **47**, 197 (2002).

[11] J. H. Hafner, C. Cheung, T. H. Oosterkamp, and C. M. Lieber, The Journal of Physical Chemistry B **105**, 743 (2001).

[12] L. Wade, I. Shapiro, Z. Ma, S. Quake, and C. P. Collier, Nano Letters **4**, 725 (2004).

[13] S. Solares, Y. Matsuda, and W. Goddard, The Journal of Physical Chemistry B **109**, 16658 (2005).

[14] J. M. Gerton, L. A. Wade, G. A. Lessard, Z. Ma, and S. R. Quake, Physical Review Letters **93** (2004).

[15] Y. Ebenstein, E. Yoskovitz, R. Costi, A. Aharoni, and U. Banin, Journal of Physical Chemistry A **110**, 8297 (2006).

[16] E. Yoskovitz, G. Menagen, A. Sitt, E. Lachman, and U. Banin, Nano Letters **10**, 3068 (2010).

CHAPTER 4

THREE-DIMENSIONAL MAPPING OF NEAR-FIELD INTERACTIONS VIA SINGLE-PHOTON TOMOGRAPHY

In scanning probe applications, such as Atomic Force Microscopy (AFM) and Near-field Scanning Optical Microscopy (NSOM), a sharp probe is used to scan a surface. Typically, the resulting data in such applications are limited to 2D information. When the scanning probe is operated in tapping mode, the tip rapidly oscillates vertically above the surface during the lateral surface scan. The probe-sample interaction is 3D, but the results are mapped to 2D surface images. In NSOM applications, the vertical interactions can extend to wavelengths distance, and carry important information.

In this chapter, we show that the 3D information, which is naturally encoded in NSOM imaging in tapping mode, can be extracted from the data. The 3D information enables us to study the complete probe-sample interaction map. This work was published in Nano Letters, volume 9, pages 3440-3446 (2009). The entire paper is presented in this chapter. Section headings were added to the text and the figures from the supplementary information have been inserted into the main text for improved clarity.

4.1 Abstract

We demonstrate a near-field tomography method for investigating the coupling between a nanoscopic probe and a fluorescent sample. By correlating the arrival of single fluorescence photons with the lateral and vertical position of an oscillating tip, a complete three-dimensional analysis of the near-field coupling is achieved.

The technique is used to reveal a number of interesting three-dimensional near-field features and to improve image contrast in tip-enhanced fluorescence microscopy.

4.2 Introduction

Light-matter interactions are of fundamental importance for a host of nanoscale phenomena and emerging nanotechnology applications. Such interactions can be altered by proximate surfaces, particularly near nanostructures with sharp facets such as lightning rods [2, 3], optical antennae [4–6], and roughened surfaces [7–9]. For example, in surface-enhanced Raman spectroscopy (SERS) the optical scattering cross-section is enhanced for molecules near "hot spots" on a nanostructured surface, leading to an increase in the molecular detection efficiency [10]. The enhanced near-field at the end of a sharp tip can also be used for high contrast optical microscopy/spectroscopy of molecules on a surface with spatial resolution down to the nanometer scale [11–13]. Recently, a large amount of effort has been dedicated to optimizing the size and shape of optical nano-antennae to enhance light-matter interactions, thereby altering the direction and rate of a dipole's radiated emission [4–6, 14].

Within the context of apertureless near-field scanning optical microscopy (ANSOM), the optical signal is generally proportional to a dipole's excitation rate, which in the linear regime is in turn proportional to the local light intensity [14]. In ANSOM, the tip can enhance the optical intensity via both the lightning-rod effect [3, 15] and plasmon resonances [4–6, 14], and can also induce an interference pattern from the superposition of the excitation light and the light scattered off the tip [12, 16–18]. These two effects act independently to create a three-dimensional intensity pattern that contains fluctuations on a number of length scales ranging from nanometers to roughly the wavelength. Additionally, a proximate tip can also suppress a dipole's spontaneous emission rate via nonradiative energy transfer (fluorescence quenching) [19–25]. The quenching efficiency depends sensitively on the probe material, being highest for metals. All three tip-induced effects, field enhancement, optical interference, and fluorescence quenching, are exquisitely sensitive to tip geometry.

The interplay of the complex intensity pattern and the quenching distribution yields an optical image with rich, three-dimensional structure whose precise shape is due to the particular tip-sample coupling mechanisms at play for the given experimental conditions [26]. In this letter, we present the first method that can produce a three-dimensional, subnanometer precision map of the optical signal resulting from these tip-sample interactions.

A three-dimensional theoretical model of the interplay between the complex tip-modified intensity pattern and the fluorescence quenching distribution is quite difficult to generate, and is left to the future. Rather, in this work we use the three-dimensional structure of the resulting optical signal to demonstrate the capabilities of our tomographical reconstruction technique. In particular, we reveal this intricate pattern by scanning 20-nm diameter dye-doped latex spheres through the region near the apex of an illuminated atomic force microscope (AFM) tip. These spheres contain several tens of individual dye molecules (up to $\sim$200) with random orientations, thus mitigating effects related to the direction of the emission dipole moment. Using these spheres, the topographical signal is easily and accurately registered with the optical image. The resulting composite images reveal three-dimensional features of the tip-sample coupling mechanisms in extraordinary detail. This work differs from previous reports in that it reveals the full three-dimensional structure of the net tip-sample coupling map, rather than simple one-dimensional approach curves [18, 23, 24, 27] or two-dimensional maps that obscure structure in the third (vertical) dimension [12, 13, 18, 21, 24, 28, 29].

4.3 Method

Our method is based on scanning near-field optical microscopy (SNOM), or more particularly, tip-enhanced fluorescence microscopy (TEFM) [28, 30, 31]. In this technique, a focused laser beam illuminates an nm-scale AFM tip composed of either metal (typically gold) or silicon, which is brought into close proximity with the sample of interest (Fig. 4.1). The fluorescence rate is monitored with an avalanche photodiode (APD) as the sample is scanned laterally relative to the tip position. Significantly,

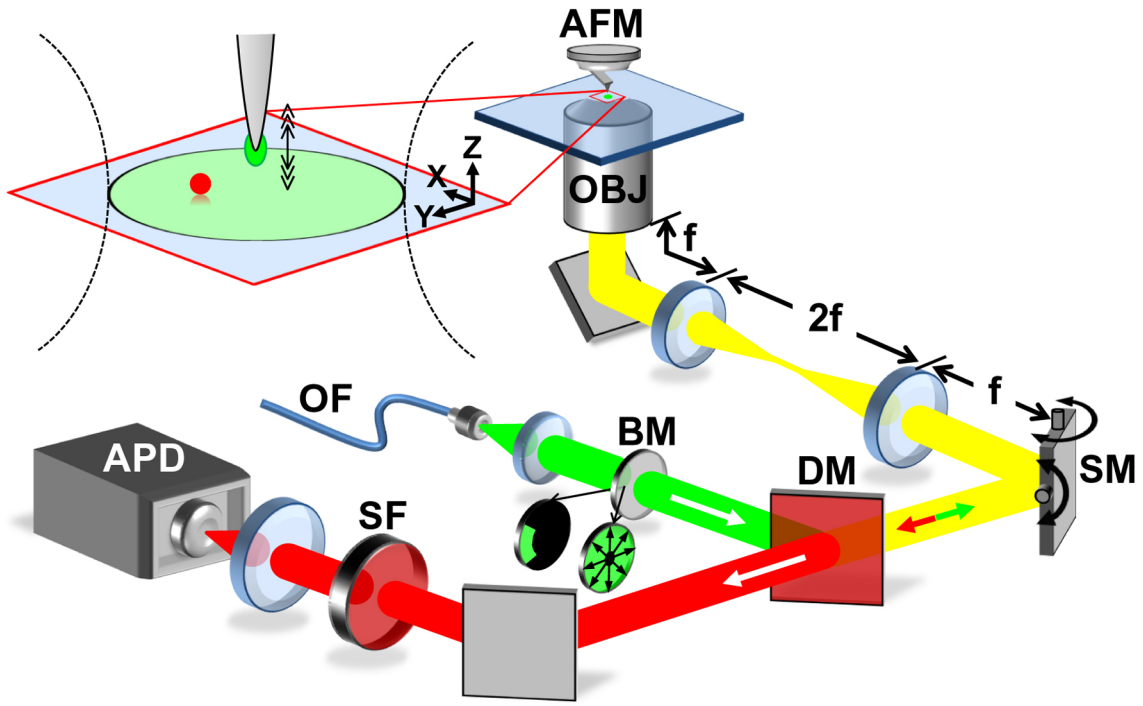

Figure 4.1. Schematic of experiment. A laser beam is directed through a beam mask (BM), producing either a radially polarized laser beam or a 60° section (wedge) of an annular beam. A microscope objective (OBJ: NA = 1.4) focuses the laser beam and collects emitted fluorescence, which is focused onto an avalanche photodiode (APD). The laser focus is positioned onto an AFM tip (oscillation amplitude: 10 - 500 nm) using a scanning mirror (SM). The sample is raster-scanned laterally, where by convention the X-axis corresponds to the fast-scan direction. The inset shows the tip-sample interaction region in more detail. Other important components include an optical fiber (OF), a dichroic mirror (DM), and a spectral filter (SF).

large amplitude (> 10 nm) vertical oscillations in the tip-sample distance are obtained in intermittent-contact (tapping) mode by driving the cantilever on resonance via a piezoelectric transducer. As described below, these oscillations provide the means to map the tip-sample coupling in the vertical (Z) direction, i.e., transverse to the sample plane. Any method of tip-sample distance control that can be made to induce significant vertical oscillations of the tip, including all types of both cantilever and tuning-fork based SNOM techniques [29], can be employed to produce the desired three-dimensional map.

Our TEFM system utilizes a commercial AFM (Asylum Research) sitting atop a

custom optical setup. A green He-Ne laser ($\lambda = 543$ nm) is used for excitation and the laser beam is directed through either a radial polarization converter (Arcoptix) or through a focused-TIRF (total internal reflection fluorescence) arrangement. The radially polarized beam produces longitudinal polarization (along the tip axis) at the sample interface. In focused-TIRF, all but a small wedge of supercritical rays are blocked in the infinity space behind the microscope objective, producing an evanescent field above the interface within a near diffraction limited spot ($\approx 1.5\ \mu$m $\times$ $0.5\ \mu$m). The polarization of the annular beam can be adjusted to produce longitudinal or transverse polarization at the interface. The laser beam is focused through a high numerical aperture objective (NA = 1.4) and fluorescence signals are collected through the same objective and detected by an APD (Perkin Elmer). The laser focus is aligned onto an AFM probe; when the excitation polarization is longitudinal, an enhancement in the optical intensity is expected at the tip apex due to a nonresonant lightning-rod effect (i.e., far from any plasmon resonance). Topographical and photon sum signals are recorded simultaneously via the AFM controller and displayed in real time. The APD signal can also be analyzed in real time using a commercial lock-in amplifier (Stanford Research Systems) [28, 31]. These real time signals are primarily used for aligning the tip and laser and to produce one- and two-dimensional maps of the near-field coupling between the tip and sample.

To obtain three-dimensional maps, a pair of data acquisition cards (NI PCI-6251, NI USB-6210) is used to sample (at 80 MHz frequency) and record the arrival time of each detected photon, and to generate time stamps for each tip oscillation and AFM line marker. The tip oscillation time stamps are obtained by transforming the AFM deflection signal into a square wave that triggers a time measurement at a particular phase of each oscillation cycle. After acquiring these data channels, the tip oscillation phase corresponding to each photon arrival is computed and recorded to a computer disk. If the cantilever oscillation is harmonic, the photon phase delays can be correlated with the height of the tip above the sample after calibrating the tip oscillation amplitude. Alternatively, if the cantilever oscillations are anharmonic, the AFM deflection signal can be recorded by an analog-to-digital card at a predefined

sample rate, enabling real time measurement of the precise cantilever trajectory. In either case, the fluorescence rate can be correlated with the lateral position of the probe using the AFM line markers.

As the sample is rastered, histograms of photon phase delays are accumulated and parsed into the assigned lateral $(x-y)$ pixels. This results in a two-dimensional array of vertical approach curves, which represents a three-dimensional map of the near-field coupling between the tip and sample. The photon sum for each three-dimensional pixel (voxel) is normalized to its corresponding acquisition time. Thus, the value of a given voxel within the three-dimensional image space corresponds to the fluorescence count *rate* at that particular coordinate $(x,\ y,\ z)$. Since the photon count rates are stored as a three-dimensional array, the data can be sectioned arbitrarily. This method for producing three-dimensional tomographical reconstructions relies upon the phase-correlation of single photons, and we therefore call it single photon near-field tomography, or SP-NFT. It is important to note that the SP-NFT data are not a direct map of the near-field optical intensity pattern, but rather the signal that results from the interplay of all tip-sample interactions.

4.4 Results

Figure 4.2 shows an X-Z slice generated by graphically displaying a linear array of vertical approach curves at a particular value of y (the slow scan axis). Here, the near-field coupling between a 20-nm diameter fluorescent sphere and a gold tip is measured along a Y-section that cuts through the topographical center of the sphere. When the tip is sufficiently far from the sample ($z \sim \infty$) such that no tip-sample coupling occurs, voxel values reflect the laser-induced far-field fluorescence rate, $S_{z\sim\infty} \approx S_{ff}$. Thus, a precise measure of the *local* far-field contribution to the fluorescence rate is obtained at each lateral position by averaging the values of a number of voxels corresponding to large tip heights. At small tip-sample separations, the fluorescence signal contains contributions from both far-field and near-field interactions $S_{z\sim0} \approx S_{nf}+S_{ff}$. The tip-induced modification to the fluorescence rate is then easily isolated by subtracting the local far-field rate, as shown in Fig. 4.2(e). This subtraction dynamically accounts for

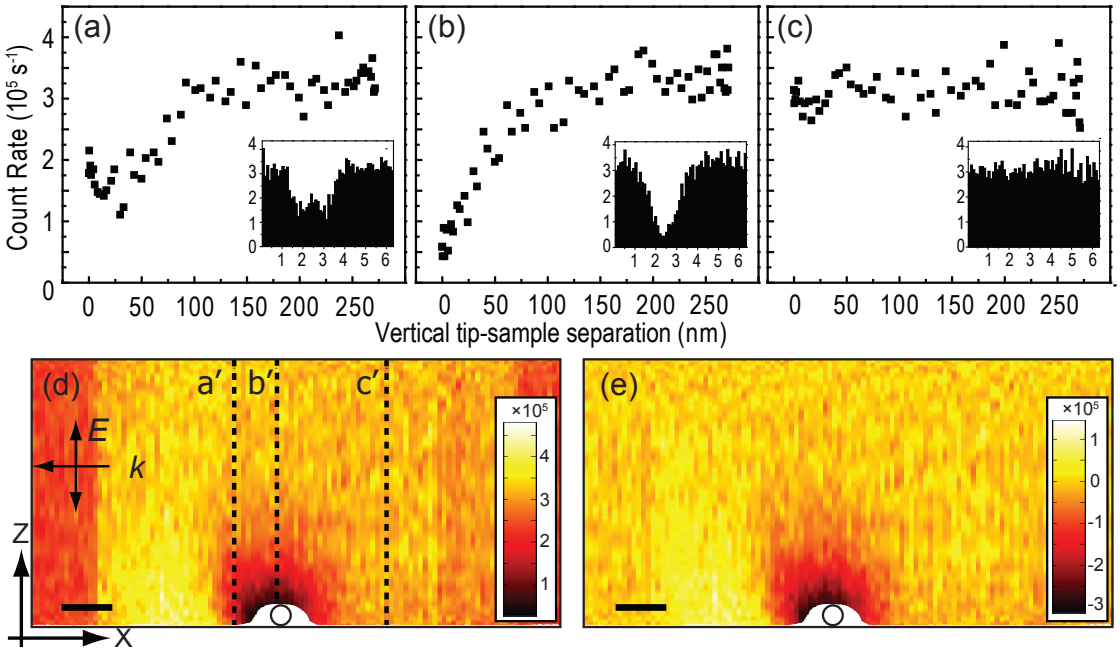

Figure 4.2. Tomographical reconstruction of a 20-nm diameter fluorescent sphere. The vertical approach curves and associated phase histograms shown in panels (a) - (c) correspond to the lateral positions indicated by the dashed lines a′, b′, and c′ in panel (d). The lower image panels are total (d) and far-field subtracted (e) X-Z sections where each column of pixels corresponds to a vertical approach curve. In all panels, the detected photon counts have been normalized to the relevant acquisition time to generate photon count *rates*. For these data, focused-TIRF illumination was used (Fig. 4.1) to produce an evanescent field with polarization parallel to the long axis of a gold-coated tip. The scale bars correspond to 50 nm.

spatial variations and temporal fluctuations in the laser intensity and also for single-molecule blinking or slow photobleaching of a multichromophoric sample. To further elucidate three-dimensional variations of the tip-sample coupling, the fluorescence data can be superimposed onto the topographical data. This is shown in Fig. 4.2(d) and (e) as the white cutout region at the bottom of the image panels; the actual size of the fluorescent sphere is indicated by the circular outline in that region. Duplicity in the fluorescence signal acquired with the data acquisition card and the AFM controller accounts for any electronic delays between the two, ensuring that the *topography* signal is properly registered with the SP-NFT image.

Figure 4.2 reveals a number of interesting effects that would be difficult to cap-

ture accurately with either a two-dimensional lateral image or a one-dimensional approach curve. First, there is a three-dimensional "halo" of reduced fluorescence signal extending ∼100 nm from the surface of the sphere. In this region there is no observable enhancement in the fluorescence signal even though the axial polarization of the excitation field should lead to an enhancement in the optical intensity at the tip. For metal tips with a closed geometry, such as a sphere or prolate spheroid, the lightning rod effect and surface plasmon resonances can augment each other leading to exceedingly large field enhancement factors near the plasmon resonance frequency. However, for metal tips with an open geometry, such as commercial AFM probes, surface plasmons will be strongly dissipated [15, 18, 24, 26]. Furthermore, elongated tip geometries lead to a large red shift in the plasmon resonance spectrum. These two factors act to suppress plasmon-based field enhancement in this experiment, which used commercial gold-coated AFM tips and a green excitation wavelength (543 nm).

Ohmic dissipation mechanisms are responsible for strong quenching of fluorescence by metal tips, and reduce the optical signal in direct competition with field enhancement [20, 21]. This tug-of-war has been observed in recent one-dimensional approach curve measurements using spherical gold tips [23, 25]. In those studies, the closed spherical geometry led to clear field enhancement, which was mitigated by quenching only at very short range. For tips with open geometries, the balance between field enhancement and fluorescence quenching is pushed toward weaker enhancement and stronger quenching [32]. In this work, commercial gold-coated AFM tips were used, and the quenching evidently overwhelms field enhancement even at very short tip-sample separation distances. The complete lack of observable signal enhancement for metal-coated tips with pyramidal geometry has also been observed in previous work [18, 20, 21, 24].

Note that the approach curve shown in Fig. 4.2(a) corresponding to axis a′ to the left side of the sphere exhibits partial recovery in the fluorescence signal. If Fig. 4.2(a) had been obtained in isolation, it would be tempting to attribute the partial recovery to a more favorable balance between field enhancement and fluorescence quenching. However, after several tens of measurements at this illumination wavelength (543

nm), such a partial recovery has never been observed when the approach curve is measured along an axis directly above the geometric center of the sphere, e.g., panel (b) corresponding to axis b′. Thus, we attribute the partial recovery in this case to the particular location with respect to the detailed shape of the tip-sample coupling map at which this approach curve was acquired. Specifically, at this location the sample is quenched to a lesser extent so that the fluorescence signal begins approaching the far-field background rate as the tip is lowered to the glass surface. On the other hand, Fig. 4.3 shows approach curve data obtained using an excitation wavelength of 633 nm. In that case, the partial recovery in the fluorescence rate *is* due to a more favorable balance between enhancement and quenching. This more favorable balance is expected at longer wavelengths given the elongated tip geometry, as discussed above.

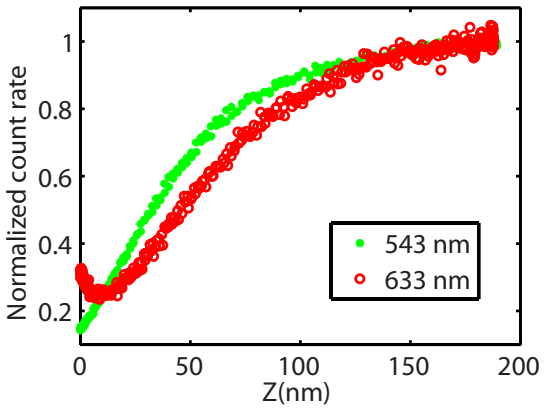

Figure 4.3. Comparison of approach curves at two different wavelengths, 543 nm (solid green circles) and 633 nm (open red circles). Both curves were obtained using gold-coated AFM tips on dye-doped latex spheres of nominally the same size (20 nm) with vertically-polarized evanescent illumination. Although these data were acquired by freezing the lateral motion of the tip (to improve photon statistics), the shape of each curve agrees with those extracted from a full three-dimensional data set. Clearly the competition between field enhancement and fluorescence quenching tilts more toward enhancement at 633 nm. However, the monotonic decrease in observed fluorescence rate at 543 nm for decreasing tip-sample separations does not indicate a complete lack of field enhancement, rather that quenching overwhelms enhancement at all length scales.

The optical interference pattern generated by the superposition of the direct excitation light and that scattered from the tip also contributes to the three-dimensional structure of the image. In Fig. 4.2, this interference pattern manifests itself as the bright region to the left of the sphere position, which arises from the constructive interference between the evanescent wave and the light scattered off the tip when it is downstream of the sphere. For these data, focused-TIRF illumination was used (Fig. 4.1 - annular wedge beam mask) yielding a vertically polarized evanescent field at the glass-air interface traveling from right to left. Such interference features have been observed in previous work when similar illumination conditions were used [12, 16–18]. As shown in the supplementary material, when the polarization of the evanescent field is horizontal (perpendicular to the tip axis) these long-range features are strongly suppressed and only the primary dark halo is visible [17]. This is reasonable since the effective dipole moment of the tip should be predominantly along the tip axis, so light scattering should be weaker for horizontal polarization.

Note that the dark halo shown in Fig. 4.2 is not spherically symmetric and is skewed to the left. This asymmetry is independent of both the propagation direction of the evanescent field and the sample scan direction (see Fig. 4.4), but does depend somewhat on the particular tip used. Thus, the asymmetry of the halo is evidently a tip-specific effect. Although a detailed explanation of this effect would require more extensive investigation, it is likely that the redirection of fluorescence emission caused by an antenna-like coupling between the tip and the fluorophores in the sphere plays a role. This type of coupling has been demonstrated previously [6], and would contribute to the observed reduction of the fluorescence signal by biasing the emission pattern toward the tip, and thus away from the collection solid angle of the microscope objective. Within this context, the observed skew in the dark halo is likely caused by a tilt in the effective antenna axis of the gold tip or by an asymmetric shape. In this case, this effect is subtle since the sample is composed of a large number of fluorescent molecules with random dipole orientations, and only due to the extremely high precision of our technique is it visible at all.

SP-NFT can generate two-dimensional planar sections with arbitrary orientation

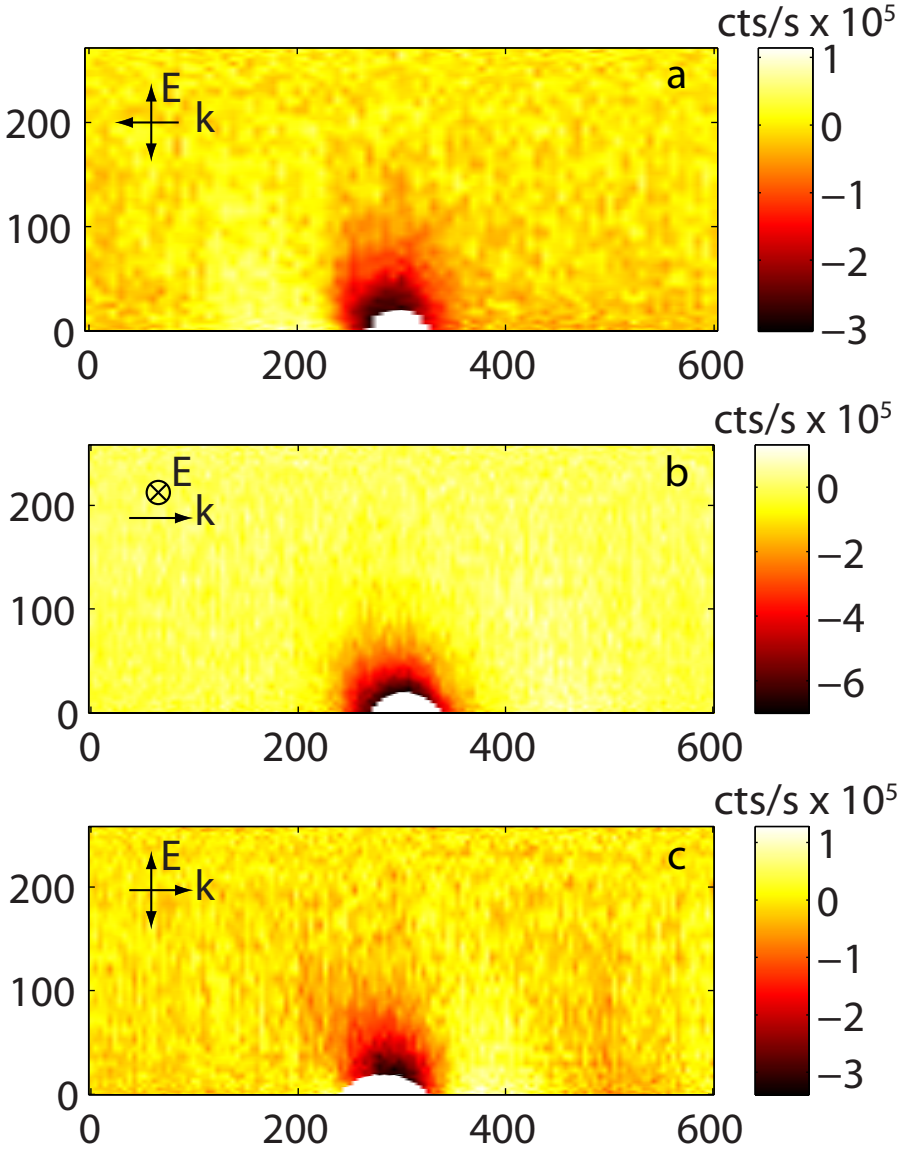

Figure 4.4. Comparison of different illumination and scan conditions from Fig. 4.2. All images are obtained with evanescent illumination at 543 nm excitation and gold-coated AFM tips and have been far-field subtracted. Distances on both vertical and horizontal axis are in nm. The AFM topography can be seen in white. Notice the leftward skew of the central dark halo in all images. Retrace of Fig. 4.2 is shown in (a). Panel (b) shows that the bright spot due to interference is drastically reduced for s-polarized wedge illumination. Panel (c) corresponds to vertically polarized light incident from the left instead of the right. The same tip was used for both (b) and (c).

and position. To illustrate this ability, Fig. 4.5 shows the intersection of an X-Z and a Y-Z plane on top of an X-Y plane ($z \sim 0$) for a 20-nm diameter fluorescent sphere. In this image, strong enhancement in the fluorescence signal is clearly visible only when the tip is directly above the sphere and within ∼10 nm of its surface. These data were taken using a silicon tip with radial polarization, and the fluorescence enhancement is attributed to the lightning-rod effect in agreement with previous observations [3,12,13,27,28,31]. The *signal* enhancement factor ($S_{z\sim 0}/S_{z\sim\infty}-1$) under these conditions has been measured to be as large as ∼8. Since the enhanced-field volume is much smaller than volume of the fluorescent sphere, however, the *field* enhancement factor is significantly larger [27, 31].

The interference pattern generated by the superposition of the excitation light and that scattered from the tip is clearly visible in Fig. 4.5 as the three-dimensional

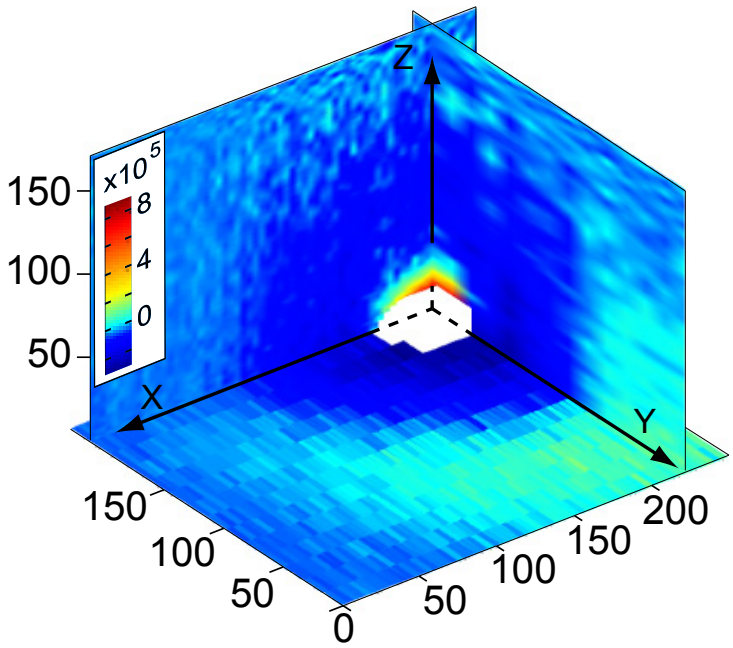

Figure 4.5. Three-dimensional tomographic reconstruction of a 20-nm diameter fluorescent sphere using a silicon tip. The intersection of two vertical planes, X-Z and Y-Z, that cut through the topographical center of the sphere is shown on top of a $z \sim 0$ plane. The local far-field fluorescence rate has been subtracted from these data as described above. Note, the colorbar has been chosen to emphasize the spatial extent of the enhancement and the surrounding dark halo.

halo of fluorescence suppression that surrounds the sphere and a bright halo beyond that. In this case, the radial polarization beam mask was used, so the interference pattern is fairly symmetric around the sphere. The three-dimensional symmetry of the halo would be very difficult to deduce from one- or two-dimensional measurements. Evidently, short tip-sample separation distances correspond to destructive interference, presumably due to a 180° phase shift upon scattering from the tip, irrespective of whether the tip is silicon or gold. The resulting dark halo surrounding the tightly confined enhanced near-field region extends ∼120 nm away from the tip. These three-dimensional renderings clearly show that the length scale for tip-induced interference is much longer than field enhancement, but comparable to quenching. For silicon tips the interference pattern is not obscured by quenching at short tip-sample separations. For gold tips, however, it is difficult to fully separate the contributions of these two effects without performing lifetime measurements.

Another important aspect of the single-photon analysis method described here is the potential to increase contrast in tip-enhanced images. This will be particularly important for complex samples composed of closely spaced fluorophores, such as biological samples, where the background fluorescence signal will be large [31]. One way to increase contrast is to demodulate the fluorescence signal at the tip oscillation frequency [13, 27–29, 31], which can be done by directing the output pulses from the APD into a commercial lock-in amplifier, along with a reference wave from the cantilever oscillation signal [28, 31] (Fig. 4.1). In the context of our single photon counting technique, each photon can be considered a unit vector in phase space whose angle is given by its phase delay relative to the preceding tip-oscillation time stamp. Computationally, a lock-in algorithm is essentially equivalent to performing a *vector* rather than a scalar sum of the photon signal. Thus, photons arising from tip-induced field enhancement cluster around the particular phase corresponding to tip-sample contact, while background photons are distributed uniformly in phase space. By the same token, tip-induced fluorescence suppression (e.g., quenching), results in a relative lack of photons at the tip-sample contact phase, and thus the net lock-in phase tends toward the value corresponding to maximum tip-sample separation. Note that

the offline lock-in analysis described here generally yields better performance than a commercial lock-in amplifier because the fidelity of each photon is preserved perfectly. In addition, averaging windows and spectral filters can be made arbitrarily sharp.

Figure 4.6 shows a detailed comparison between near-field images of a 20-nm diameter fluorescent sphere generated by sectioning the data into X-Y planes (a - c) and the offline lock-in algorithm described above (e - g). These data were obtained using radial polarization and a silicon tip. Although difficult to display on a two-dimensional page, SP-NFT can easily generate a stack of two-dimensional images to elucidate the full three-dimensional symmetry of the tip-sample interaction (see supplementary material). Panels (a) and (b) of Fig. 4.6 show two such X-Y sections corresponding to two different ranges of tip height, $z \geq 200$ nm (a) and $z \leq 1$ nm (b). Panel (c) is the difference between the two panels (b - a), and thus provides a graphical representation of the tip-sample coupling at $z \sim 0$. In panel (e), the value of each lateral pixel is the magnitude of the vector photon sum normalized to the pixel acquisition time, while panel (g) shows the phase angle of this resultant vector. Panel (f) shows the vector photon sum after the application of a phase filter that eliminates photons which do not contribute to the near-field signal, as described below.

Note that it is not possible to determine if a particular commercial lock-in signal corresponds to an increase or decrease in the fluorescence signal at tip-sample contact. However, since the offline lock-in analysis is derived from the same dataset used to generate the X-Y sections, it is trivial to perform this correlation with our system. Furthermore, a lock-in amplifier essentially reports the *net* change in fluorescence signal as the tip-sample distance is modulated during an oscillation cycle. As such, a lock-in analysis cannot reveal nonmonotonic variations in the fluorescence signal as a function of tip-sample separation distance. In contrast, such variations are preserved through SP-NFT. For instance, Fig. 4.5 shows both a decrease and increase in the fluorescence signal for decreasing tip-sample distance for lateral positions directly above the sphere. These nonmonotonic signal variations are also present in the data corresponding to Fig. 4.6, but are not visible in the lock-in image. These observations demonstrate another way in which SP-NFT outperforms a commercial lock-in ampli-

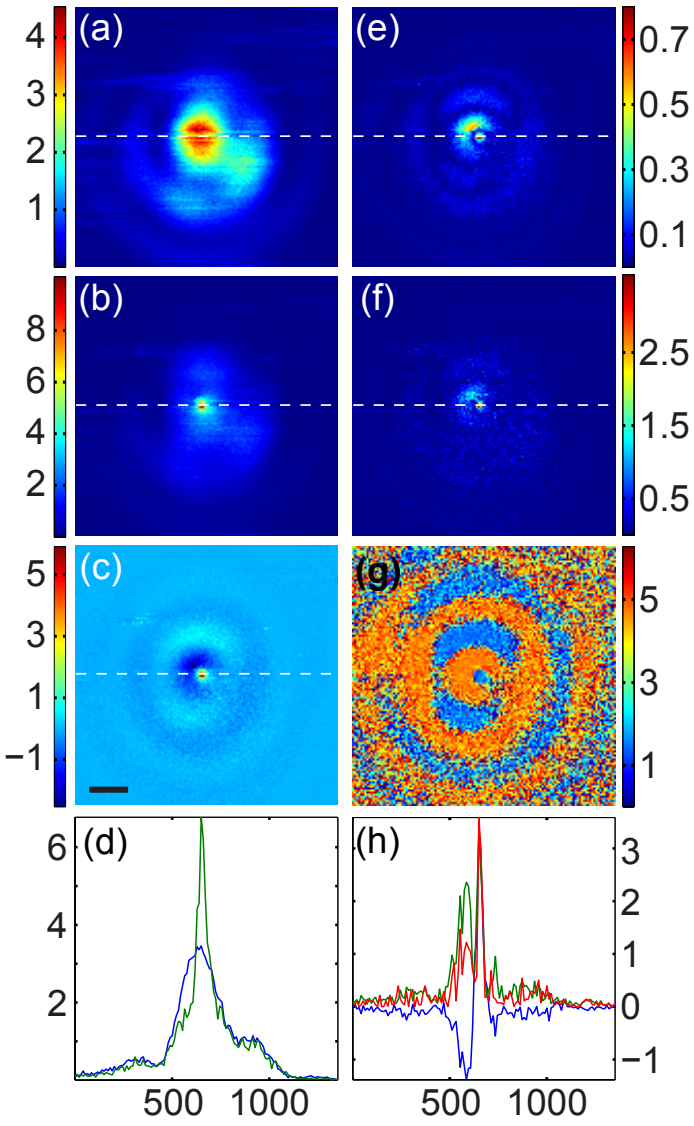

Figure 4.6. Comparison of tomographical and lock-in analyses. All colorbars represent count rates $\times 10^5$ counts per second. Panel (a) shows an X-Y section corresponding to the *scalar* count rate of photons when the tip is far from the sample ($z \geq 200$ nm), panel (b) corresponds to $z \leq 1$ nm, and panel (c) is their difference (b - a). The signal profiles in panel (d) are taken along the dotted line, and include the count rate from panel (a) in blue, and the count rate from panel (b) in green. Panel (e) shows the magnitude of the *vector* sum of all detected photons within each pixel, which is essentially equivalent to lock-in amplification. Panel (f) shows a phase-filtered lock-in algorithm generated from the vector sum of photons within narrow phase windows. Panel (g) shows the phase of the resultant vector from (e). The signal profiles in panel (h) include the count rate from panel (e) in green, the count rate from panel (f) in red, and count rate from panel (c) in blue. The data in panels (e) and (f) and their corresponding signal profiles have been normalized to the peak value in panel (c).

fier when demodulating near-field images. Furthermore, this performance is achieved at a fraction of the cost of a commercial instrument [28, 31].

The lock-in image pattern in panel (e) of Fig. 4.6 is similar to the far-field subtracted image in panel (c), with a sharp central maximum due to tip-induced field enhancement, surrounded by a diffuse ring corresponding to the interference effect discussed above. For imaging purposes, the interference pattern is artifactual, as it will reduce contrast particularly for dense samples. One way to suppress such artifacts is to apply a phase filter to the data before performing the vector sum, as shown in Fig. 4.6(f). Here the phase filter was chosen to eliminate all photons from the data set except those within a narrow phase window centered at tip-sample contact ($z \sim 0$). To help offset the far-field contribution within this window, photons within an equal-width phase window centered 180° from tip-sample contact ($z \sim \infty$) are also included in the vector sum [13, 27]. This algorithm eliminates photons corresponding to features with long length scales in the vertical (z) direction, without affecting those photons that contribute directly to the near-field signal [31]. This algorithm is globally applied photon by photon, and the signal cross-sections in Fig. 4.6(h) clearly demonstrate that the halo-like imaging artifact is suppressed, although not completely eliminated. It is crucial to note that there is no limit to the number and variety of analysis algorithms that can be implemented to optimize image contrast for any particular situation.

The tip-induced interference pattern is visible as the dark halo in Fig. 4.6(c), but is most clear in the lock-in phase image shown in panel (g). Under these conditions, the lock-in phase primarily adopts two values in the tip oscillation trajectory corresponding to tip-sample contact and maximum tip-sample separation, which very sensitively report an increase or decrease, respectively, in the fluorescence rate relative to the background. This binary distribution of the lock-in phase holds fairly rigorously even when the tip is relatively far from the fluorescent sphere. When this is the case, the sphere is illuminated by the periphery of the laser focal spot (e.g., Fig. 4.6(a)) where the intensity is quite low, while the tip is positioned near the center of the focus. Despite this, the lock-in phase is not strictly random, which

clearly highlights the spatial extent of the tip-induced optical interference pattern. A number of measurements using different tips, both silicon and gold, demonstrate that the symmetry of the interference pattern depends on *both* the detailed intensity pattern within the far-field focal spot *and* the particular tip geometry. For clarity, we have chosen a dataset with minimal asymmetry, but the pattern can become distorted when using tips with different geometries, or if the illumination conditions are altered significantly (e.g., focused-TIRF vs. radial). Figure 4.7 (originally in the supplementary material) compares a cross-section of the far-field Airy pattern with the near-field interference pattern to show that the two are distinct from each other.

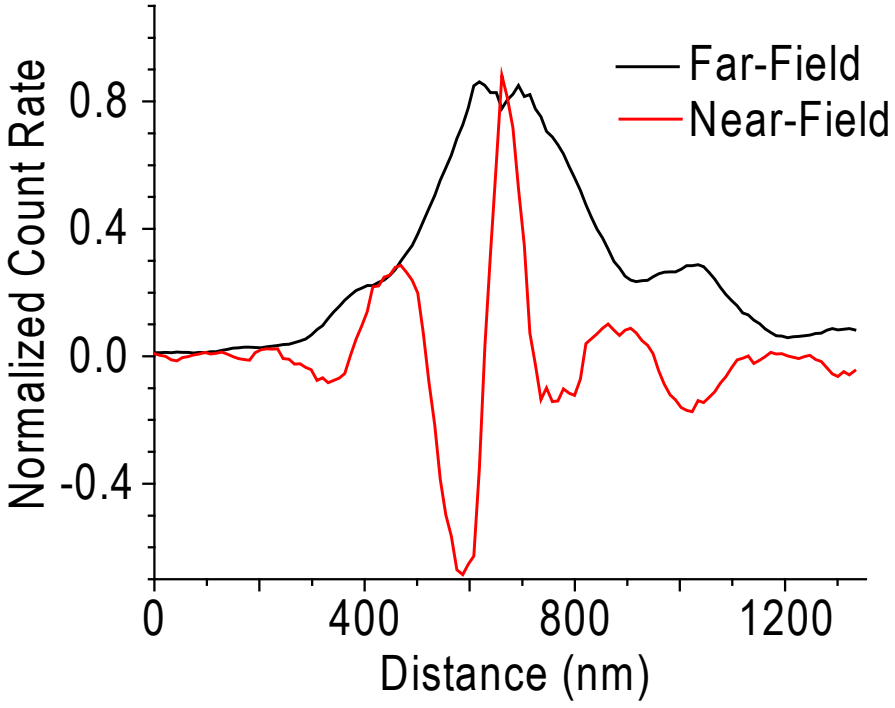

Figure 4.7. Comparison of cross-sections over the fluorescent bead taken from images found in Fig. 4.6 corresponding to panel (a) far-field and panel (c) near-field. The patterns shown indicate that the interference pattern from the tip (red) is distinct from the Airy pattern visible in the far-field (black).

4.5 Summary

In summary, we presented a single-photon counting technique for generating three-dimensional tomographical reconstructions of tip-sample interactions in tip-enhanced fluorescence microscopy. Our technique has a number of advantages compared to previous near-field tomographical measurements [33–35]. Most importantly, all three spatial dimensions of the fluorescence map are acquired simultaneously in a single measurement along with standard AFM channels (topography, oscillation amplitude, and phase). Thus, fluctuations in the fluorescence signal unrelated to tip-sample coupling can be easily detected and removed. Furthermore, uncertainties in the tip position relative to the sample are largely eliminated. The versatility of the technique was demonstrated by revealing a number of interesting three-dimensional features when imaging 20-nm diameter fluorescent spheres. In particular, the extremely high sensitivity and precision of this technique enabled the first measurement of the three-dimensional image pattern resulting from the complex interplay between field enhancement, fluorescence quenching, and tip-induced optical interference.

The ability of this technique to tomographically map the full three-dimensional dependence of the tip-sample interactions makes it quite powerful for developing and testing near-field models and we anticipate its extensive use in the future to aid in the study of a variety of nanophotonic phenomena and in the development of materials with increased functionality. It may be particularly useful in the design and development of novel nano-antenna geometries based on plasmon resonances, a topic which has gained considerable attention in recent years. Furthermore, this technique can be applied to study the near-field interactions between any two particles, provided one of them can be attached to an AFM tip. For example, it is now being used to study energy transfer between various fluorophore species (quantum dots, organic polymers, etc.) and carbon nanotubes attached to the tip, with the ultimate goal of designing nanotube-based photovoltaic materials. Finally, the technique can be used to improve image contrast in tip-enhanced fluorescence microscopy, as demonstrated by applying a number of phase-sensitive analysis algorithms.

4.6 Acknowledgement

This work was supported by a Cottrell Scholar Award from the Research Corporation for Science Advancement and by an NSF CAREER Award number DBI-0845193.

4.7 References

[1] B. Mangum, E. Shafran, C. Mu, and J. Gerton, Nano Letters **9**, 3440 (2009).

[2] L. Novotny, Applied Physics Letters **69**, 3806 (1996).

[3] J. L. Bohn, D. J. Nesbitt, and A. Gallagher, Journal of the Optical Society of America A **18**, 2998 (2001).

[4] P. Mhlschlegel, H. J. Eisler, O. J. F. Martin, B. Hecht, and D. W. Pohl, Science **308**, 1607 (2005).

[5] J. N. Farahani, D. W. Pohl, H. J. Eisler, and B. Hecht, Physical Review Letters **95**, 4 (2005).

[6] T. H. Taminiau, F. D. Stefani, F. B. Segerink, and N. F. Van Hulst, Nature Photonics **2**, 234 (2008).

[7] M. Fleischmann, P. J. Hendra, and A. J. McQuillan, Chemical Physics Letters **26**, 163 (1974).

[8] D. L. Jeanmaire and R. P. VanDuyne, Journal of Electroanalytical Chemistry **84**, 1 (1977).

[9] M. G. Albrecht and J. A. Creighton, Journal of the American Chemical Society **99**, 5215 (1977).

[10] K. Kneipp et al., Physical Review Letters **78**, 1667 (1997).

[11] H. G. Frey, S. Witt, K. Felderer, and R. Guckenberger, Physical Review Letters **93** (2004).

[12] V. V. Protasenko, A. Gallagher, and D. J. Nesbitt, Optics Communications **233**, 45 (2004).

[13] Z. Y. Ma, J. M. Gerton, L. A. Wade, and S. R. Quake, Physical Review Letters **97** (2006).

[14] L. Novotny and B. Hecht, *Principles of Nano-Optics*, Cambridge University Press, Cambridge, 2006.

[15] J. T. Krug, E. J. Sanchez, and X. S. Xie, Journal of Chemical Physics **116**, 10895 (2002).

[16] C. Girard, O. Martin, and A. Dereux, Physical Review Letters **75**, 3098 (1995).

[17] F. H'Dhili, R. Bachelot, A. Rumyantseva, G. Lerondel, and P. Royer, Journal of Microscopy **209**, 214 (2003).

[18] S. Kuhn, U. Hakanson, L. Rogobete, and V. Sandoghdar, Physical Review Letters **97** (2006).

[19] S. Link and M. A. El-Sayed, Journal of Physical Chemistry B **103**, 4212 (1999).

[20] T. J. Yang, G. A. Lessard, and S. R. Quake, Applied Physics Letters **76**, 378 (2000).

[21] W. Trabesinger, A. Kramer, M. Kreiter, B. Hecht, and U. P. Wild, Applied Physics Letters **81**, 2118 (2002).

[22] C. Neacsu, G. Steudle, and M. Raschke, Applied Physics B **80**, 295 (2005).

[23] P. Anger, P. Bharadwaj, and L. Novotny, Physical Review Letters **96** (2006).

[24] S. Kühn, U. Håkanson, L. Rogobete, and V. Sandoghdar, Physical Review Letters **97**, 017402 (2006).

[25] P. Bharadwaj and L. Novotny, Optics Express **15**, 14266 (2007).

[26] L. Novotny and S. J. Stranick, Annual Review of Physical Chemistry **57**, 303 (2006).

[27] J. M. Gerton, L. A. Wade, G. A. Lessard, Z. Ma, and S. R. Quake, Physical Review Letters **93** (2004).

[28] C. A. Xie, C. Mu, J. R. Cox, and J. M. Gerton, Applied Physics Letters **89** (2006).

[29] C. Hppener, R. Beams, and L. Novotny, Nano Letters **9**, 903 (2009).

[30] C. Mu, B. D. Mangum, C. Xie, and J. M. Gerton, IEEE Journal of Selected Topics in Quantum Electronics **14**, 206 (2008).

[31] B. D. Mangum, C. Mu, and J. M. Gerton, Optics Express **16**, 6183 (2008).

[32] N. A. Issa and R. Guckenberger, Optics Express **15**, 12131 (2007).

[33] T. Grosges and D. Barchiesi, Optics Letters **31**, 3435 (2006).

[34] D. Barchiesi, Applied Optics **45**, 7597 (2006).

[35] H. G. Frey, F. Keilmann, A. Kriele, and R. Guckenberger, Applied Physics Letters **81**, 5030 (2002).

CHAPTER 5

THE EFFECTS OF INTRINSIC QUANTUM YIELD ON THE NEAR-FIELD INTERACTIONS

The near-field interactions between a single emitter and a sharp probe are highly sensitive to the intrinsic quantum yield of the emitter. The exact effects of the quantum yield on the interactions have been difficult to study experimentally because of the challenge of changing the quantum yield while keeping all the other parameters similar. Quantum dots (QDs) are perfect for such study because their intrinsic quantum yield fluctuates dynamically in time. This property of QDs enables us to isolate the near-field interactions for different intrinsic quantum yields. Although this work was intended to mainly study near-field interactions between a QD and a sharp tip, it also explains some previous results of QDs embedded on rough metal films.

This work was published in Physical Review Letters under the following title "Using the near-field interactions to tune the fluorescence emission fluctuations during blinking of a quantum dot." Section headings inserted here are not present in the original publication. The supplementary information is added as an additional section.

5.1 Abstract

We demonstrate that the cycling between internal states of quantum dots during fluorescence blinking can be used to tune the near-field coupling with a sharp tip. In particular, the fluorescence emission from states with high quantum yield is quenched

due to energy transfer, while that from low-yield states is elevated due to field enhancement. Thus, as a quantum dot blinks, its emission fluctuations are progressively suppressed upon approach of a tip.

5.2 Introduction

The near-field interaction between a dipole emitter and a nanoscale structure is an intriguing problem that is important for a number of applications, including tip-enhanced microscopy and surface-enhanced spectroscopy. The field enhancement generated near sharp edges and tips via the electrostatic lightning-rod effect [2–6] and/or surface plasmon resonances [7–10], leads to an increase in an emitter's photoexcitation rate for separation distances below $\sim$10 nm. On the other hand, the nanostructure can also reduce the fluorescence signal by providing external nonradiative relaxation channels to which the emitter can couple directly [11–14], by modifying the local density of optical states as in the Purcell effect [15], or by altering the radiation pattern of the emitter [16]. The net optical signal can thus be quite convoluted and difficult to interpret, except when one effect is dominant, or when the field enhancement can be reliably calculated, as is the case for metal nanospheres [12–14]; deconvolution can be difficult for nanostructures with arbitrary geometry.

The intrinsic quantum yield (q_0) of an emitter plays a central role in moderating its interaction with the environment. In particular, when q_0 is large, internal nonradiative relaxation processes are slow relative to radiative emission, so even weak quenching will noticeably decrease the fluorescence signal. On the other hand, when q_0 is small, internal relaxation is fast, making the fluorophore relatively insensitive to quenching and thus more sensitive to field enhancement. Some experiments have shown that larger signal enhancement factors are obtained for lower values of q_0 [3, 17]. Here we demonstrate how different q_0 values, corresponding to different internal relaxation rates of an emitter, can be used to modify its interaction with a sharp tip by tuning the balance between quenching and enhancement. Large variations in the net fluorescence signal are observed, including a clear contrast reversal for gold tips. A simple analytical model is used to deconvolute the enhancement and quenching

portions of the signal, revealing that gold tips exhibit both strong quenching and enhancement, while silicon tips exhibit nearly as strong enhancement but very weak quenching [2–6], and carbon nanotube (CNT) tips exhibit very strong quenching and no enhancement [18]. Finally, our measurements demonstrate explicitly that fast energy transfer suppresses emission fluctuations associated with blinking from emitters near metal surfaces, in agreement with recent observations of quantum dots on metal surfaces [19], nanoparticle films [20] and ITO [21].

To investigate how q_0 affects near-field interactions, we utilize the well-known phenomenon of fluorescence intermittency (blinking) in single semiconductor nanocrystal quantum dots (QDs) [22], Fig. 5.1(b). Single-photon counting experiments have revealed a correlation between a decrease in emission intensity and a decrease in the fluorescence lifetime [23–26], leading to the conclusion that a single QD can have many different internal states [25]. These studies in combination with extinction coefficient measurements showing similar absorption cross-sections for low and high emissive states [27] suggest that the emission fluctuations are due to variations in

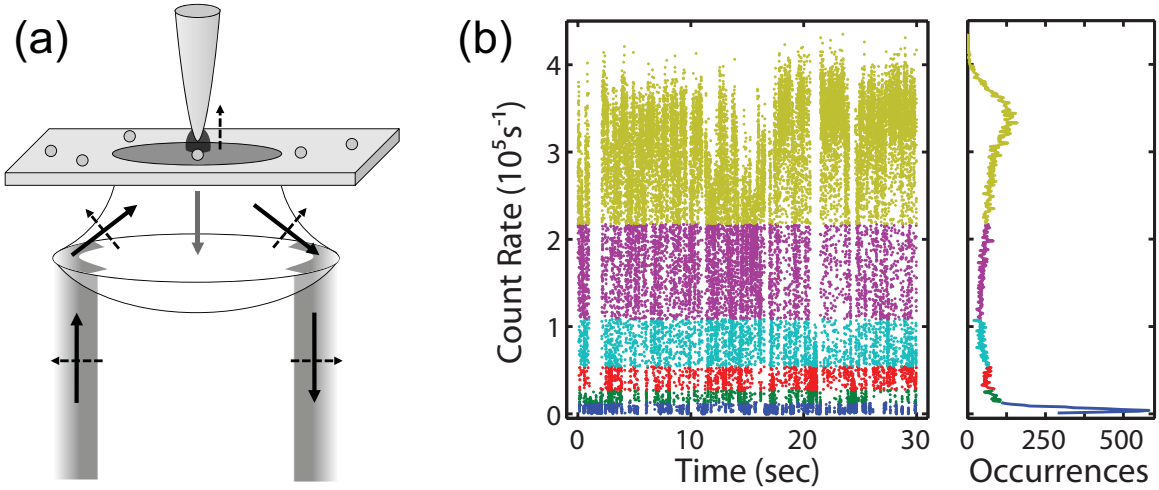

Figure 5.1. Experimental scheme. (a) Excitation light is incident on the sample above the critical angle, creating an evanescent field above the sample with polarization along the axis of the tip. Fluorescence data are collected as the tip oscillates vertically above an isolated QD. (b) Photoluminescence trajectory from a single QD. The different colors illustrate the threshold levels in Fig. 5.2(a,b).

q_0 corresponding to a relatively large number ($\sim$10) of states. We leverage these dynamic fluctuations in individual QDs to tune the near-field interactions via the value of q_0. In particular, we use a novel photon counting technique [6] to capture interaction curves as a function of both q_0 and the spatial separation between a sharp atomic force microscope (AFM) tip and an individual QD.

When an AFM tip approaches the QD from above, the fluorescence signal will increase or decrease due to the various mechanisms described. Assuming the optical transition is not saturated, the far-field normalized fluorescence signal is then given by,

$$S_{\mathrm{norm}}(z) = \frac{q(z)}{q_0}\kappa(z)\eta(z) = \frac{\Gamma_r + \Gamma'_r(z)}{\Gamma_0 + \Gamma'(z)}\frac{\kappa(z)\eta(z)}{q_0}, \tag{5.1}$$

where $q(z)$ is the effective quantum yield including modifications induced by the tip at height z above the QD, $\Gamma_0 = \Gamma_{\mathrm{r}} + \Gamma_{\mathrm{nr}}$ is the intrinsic fluorescence rate including radiative (Γ_{r}) and nonradiative (Γ_{nr}) relaxation channels, and $\Gamma'(z) = \Gamma'_{\mathrm{r}}(z) + \Gamma_{\mathrm{et}}(z)$ is the *tip-induced* relaxation rate. $\Gamma'_{\mathrm{r}}(z)$ can be negative corresponding to a tip-induced suppression of the radiative rate and $\Gamma_{\mathrm{et}}(z)$ is the energy transfer rate from QD to tip. Finally, $\kappa(z) = I(z)/I_0$ is the far-field normalized excitation intensity at the QD, which includes tip-induced near-field effects, and $\eta(z) = C(z)/C_0$ is the ratio of the geometric collection efficiency in the presence, $C(z)$, and absence, C_0, of the tip. Equation (5.1) can be re-parameterized as:

$$S_{\mathrm{norm}}(z) = \frac{\alpha}{1 + q_0\beta}, \tag{5.2}$$

where $\alpha(z) \equiv \kappa(z)\eta(z)\left[1 + \Gamma'_r(z)/\Gamma_r\right]$ characterizes tip-induced changes to the local excitation intensity, the geometric collection efficiency, and the radiative rate, while $\beta(z) \equiv \Gamma'(z)/\Gamma_r$ characterizes the strength of the near-field coupling. The shape of a vertical approach curve measurement, $S_{\mathrm{norm}}(z)$, for a particular value of q_0 reflects the dynamic balance between α and β. The values of α and β are extracted from measurements of S_{norm} for different values of q_0, as demonstrated below.

For light polarized along the z-axis, the intensity at the tip apex should be enhanced due to the lightning-rod effect and/or surface plasmons. Furthermore, at short tip-sample distances z, the radiative rate of the fluorophore can be enhanced

(i.e. $\Gamma_r' > 0$) due to the Purcell effect. These two mechanisms will increase α leading to signal enhancement. On the other hand, superposition of direct and tip-scattered excitation light at the QD can lead to a decrease in $\kappa(z)$ on a wavelength scale [6,13]. Furthermore, redirection of fluorescence emission toward the tip can modify η by no more than 50% for small tip-sample separations [11,28]. Nevertheless, α is typically dominated by near-field enhancement for $z < 50$ nm. The larger the product, $q_0\beta$, the stronger the reduction in S_{norm}, so clearly a decrease in q_0 makes S_{norm} less sensitive to tip-sample coupling (quenching), and thus more sensitive to signal enhancement.

5.3 Methods

Data were obtained using a tip-enhanced fluorescence microscope (TEFM), which utilizes an AFM sitting atop a custom optical setup [6]. A continuous wave helium-neon laser ($\lambda = 543$ nm) is used as the excitation source. A small wedge of super-critical rays are allowed into the back aperture of a microscope objective (NA=1.4) such that QDs are illuminated with a z-polarized evanescent field of intensity $\sim$350 W/cm^2, Fig. 5.1(a). Using the measured extinction coefficient provided by the QD manufacturer (Invitrogen), the excitation rate is estimated to be a factor of 20 below saturation. The emitted photons are collected by the same objective and are focused onto an avalanche photodiode. The tip is aligned into the center of the focus spot and the sample is raster scanned. The AFM is operated in tapping mode with typical oscillation frequencies of 60-80 kHz and peak-to-peak amplitudes of 200-250 nm, depending on the specific probe. Several silicon, gold-coated, and home-made carbon nanotube (CNT) [29, 30] AFM probes were used for the measurements described below. The sample consisted of elongated ($4\,\text{nm} \times 9\,\text{nm}$) CdSe/ZnS QDs emitting at 605 nm, diluted in toluene and dried onto a glass coverslip. All data were taken at room temperature.

To extract vertical approach-curve measurements, $S_{\text{norm}}(z)$, the lateral sample scan is halted when the tip is directly above a QD for the duration of a measurement ($\sim$30 s), and every detected fluorescence photon is then time stamped. Each signal photon is then correlated with the instantaneous height of the tip above the QD [2,6].

The photoluminescence trajectory from an individual QD is constructed using 1 ms time bins (Fig. 5.1(b)), and each photon is assigned a far-field count-rate value corresponding to its particular bin. Three important parameters are thus encoded with each signal photon: time of emission, tip height at the time of emission, and far-field count-rate value at that point in the fluorescence trajectory. The background signal is calibrated by moving the sample to an area with no QDs, and is subsequently subtracted carefully from the data. The count-rate uncertainty (1 kHz) associated with the 1 ms time bins is of minimal significance in the analysis: it is $\sim$2 times smaller than the typical background rate and $3-5$ times smaller than the average count rate within the lowest threshold range used to differentiate between states of different q_0.

5.4 Results and discussion

Our data acquisition technique enables tip-sample approach curves to be reconstructed for different values of q_0. Figure 5.2 shows the un-normalized (a, c) and normalized (b, d) QD fluorescence signal as a function of the tip-sample distance for a gold-coated (a, b) and silicon (c, d) tip. For each tip, the various approach curves shown were extracted from a single 30-s measurement on a single QD: the photon data were first separated into several emission intensity thresholds, as illustrated in Fig. 5.1(b), and the z-dependent fluorescence signal was then reconstructed for each. The threshold ranges differ successively by a factor of two, which emphasizes the differences between the corresponding values of q_0.

For the gold-coated tip, Fig. 5.2(a, b), the bright states of the QD are strongly quenched as fast energy transfer to the tip outcompetes relatively slow intrinsic relaxation. In contrast, the darkest states are strongly enhanced as fast intrinsic relaxation outcompetes energy transfer, yielding more sensitivity to the enhanced field at the tip apex. The ratio of signal enhancement factors for the darkest state compared to the brightest one is $\sim 9/0.16 = 56$ at $z = 0$, as shown in Figs. 5.2(b) and 5.3(a) (note that a signal enhancement factor below unity indicates quenching). Thus, strong near-field coupling (large β) for gold tips amplifies changes in q_0 according to

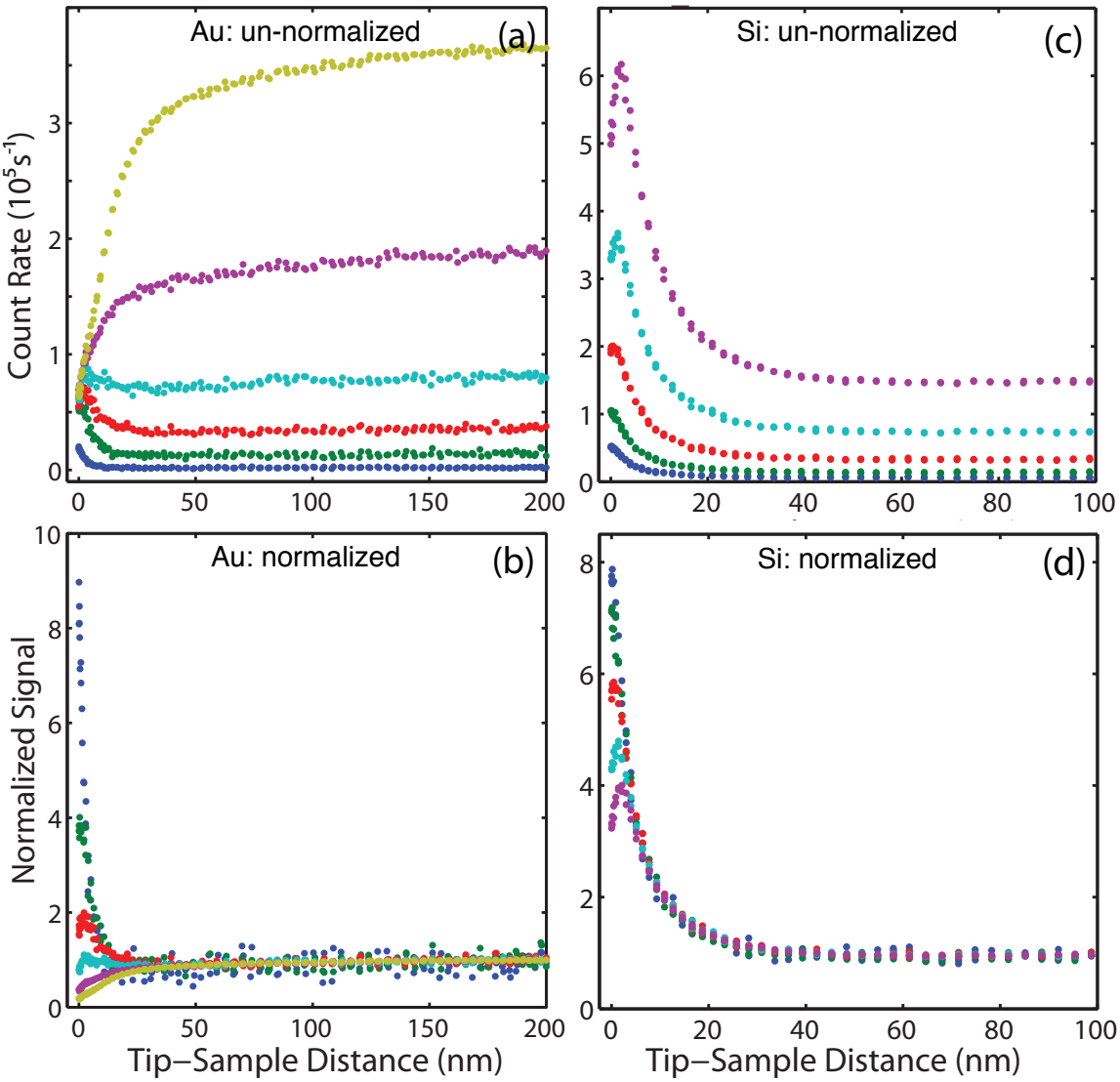

Figure 5.2. Vertical approach curves for different count-rate thresholds. Un-normalized (a, c) and normalized (b, d) fluorescence signals as a function of the tip height above a QD for gold-coated (a, b) and silicon (c, d) probes. The color-coding in (a, b) corresponds to the threshold values shown in Fig. 5.1(b). For each tip, the various approach curves were obtained from a single measurement as the QD cycled dynamically through different quantum yield states.

Eq. 5.2, leading to near-field contrast reversal for bright and dark states. Weak coupling between the silicon tip and QD imparts poor sensitivity to changes in q_0, as seen in Figs. 5.2(d) and 5.3(a). In this case, field enhancement is dominant for all values of q_0, although quenching does cause a minor decrease in signal at the smallest tip-sample separation distances. As q_0 becomes smaller, intrinsic relaxation of the QD outcompetes energy transfer at progressively smaller tip heights, until finally the signal increases monotonically as the tip approaches the QD.

Figure 5.3(a) plots S_{norm} at $z = 0$ as a function of q_0 for gold-coated, silicon, and CNT tips, where we have assumed that $q_0 = 1$ for the brightest state of a particular photoluminescence trajectory [24, 31]. For these data, the highest far-field threshold corresponded to $\geq 70\%$ of the maximum count, in agreement with previous observations [24]. The remainder of each trajectory was divided linearly into as many distinct ranges as possible, so as to allow for sufficient signal-to-noise ratio in each. If the number of internal states is sufficiently large ($\gtrsim$10), the system can be regarded as continuous and the results of the analysis will not be sensitive to the particular number of threshold ranges, N. This was verified by varying N between $\sim$12 and 30 for each measurement. The data for each trajectory in Fig. 5.3(a) were fit to Eq. 5.2; the fits (solid lines) for all three tips are excellent across more than 100-fold variation in q_0. The dashed line separates signal enhancement and quenching: the near-field signal is dominated by enhancement for silicon tips, quenching for CNT tips, and can be tuned via q_0 to either enhancement or quenching for gold-coated tips.

The analysis was repeated at each value of tip-QD separation, and the fitting parameters α and β were extracted, as shown in Fig. 5.3(c, d). The maximum value for α is larger for gold-coated tips compared to silicon, reflecting stronger field enhancement at this wavelength. Without the aid of simulations or a geometry-dependent analytical model, it is not possible to determine this difference unambiguously with any other method, since gold-coated tips also quench the signal strongly: $\beta_{\mathrm{Au}}/\beta_{\mathrm{Si}} \sim 37$ at $z = 0$. The CNT tip induces no significant enhancement at any value of q_0 or z ($\alpha_{\mathrm{CNT}} \sim 1$), but does quench the signal strongly indicating efficient energy transfer between the QD and CNT at short separations [18].

Importantly, these measurements expose the mechanism responsible for the suppressed emission fluctuations associated with blinking from quantum emitters adsorbed onto conducting surfaces [19–21]. Fig. 5.3(b) plots the un-normalized signal at $z = 0$ as a function of q_0, showing that the measured fluorescence rate is approximately constant down to $q_0 \sim 0.1$. Thus, in the case of a QD adsorbed onto a conducting surface ($z \sim 0$), the overall emission intensity is reduced due to quenching by the

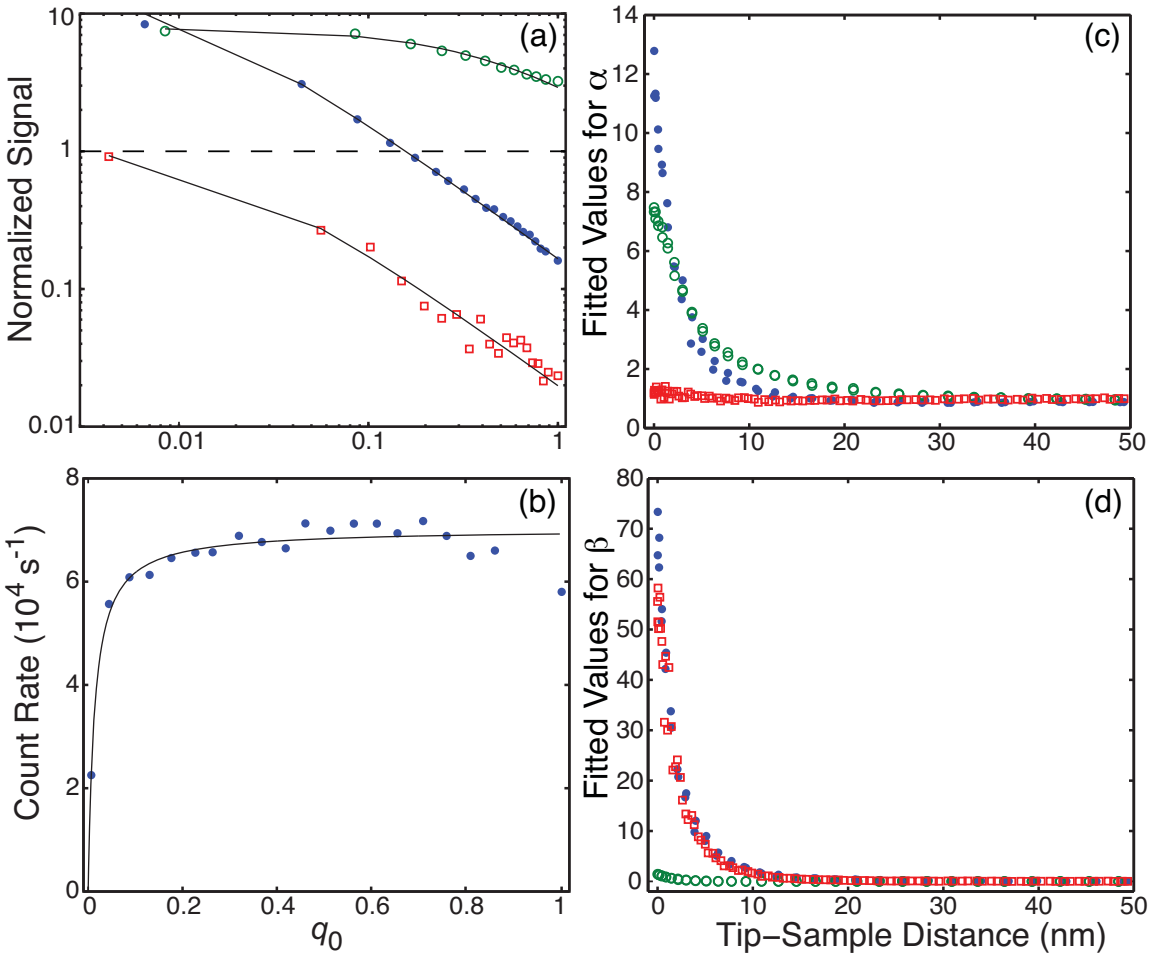

Figure 5.3. Separation of enhancement and quenching. (a) Normalized signal at $z = 0$ and corresponding fit to Eq. 5.2 for gold-coated (blue circles), silicon (green circles), and CNT (red squares) tips. The dashed line separates enhancement and quenching. (b) Un-normalized fluorescence signal at $z = 0$ for the gold-coated tip in (a); the solid line is the best fit to Eq. 5.3. Panels (a) and (c) show the fitted values for α and β for different tip-sample distances.

surface. As the QD blinks, it samples states with different q_0 values; however, the emission intensity is buffered by fast energy transfer from the QD to the surface. This is easily understood using our simple model: multiplying Eq. 5.2 by q_0 yields an expression that is proportional to the un-normalized fluorescence signal, $S(z)$:

$$S(z) \propto q_0 \, S_{\mathrm{norm}}(z) = \frac{q_0 \alpha}{1 + q_0 \beta}. \tag{5.3}$$

Thus, for large values of β, as for a gold-coated tip at $z = 0$, the product $q_0\beta \gg 1$ and until $q_0 \to 0$, the un-normalized signal will be independent of q_0: $S(z) \propto \alpha/\beta$. Importantly, the suppression of emission fluctuations is thus expected for any geometry or material for which β is large. The solid curve in Fig. 5.3(b) is the best fit line corresponding to Eq. 5.3, with $\alpha = 12.8$ and $\beta = 73.4$, as extracted from Fig. 5.3(c, d), and the proportionality factor as the only fitting parameter. When $q_0\beta \gg 1$, the fluorescence rate (relative to the far-field value) converges to α/β, which depends on the probe geometry and material. For gold-coated tips, $\alpha/\beta \sim 0.17$ at $z = 0$, so the fluorescence signal is nearly six-fold smaller than the maximum far-field value, and the lack of emission fluctuations are easily discerned. For CNT tips, $\alpha/\beta \sim 0.02$ so the fluorescence signal is suppressed by nearly a factor of 50, and it is difficult to detect the lack of fluctuations above the noise level.

5.5 Conclusion

In conclusion, the dynamic fluctuations in quantum yield that occur during QD blinking tune the balance between tip-induced enhancement and quenching, and make it possible to separate their contributions to the net fluorescence signal. Our measurements show that the near-field signal is dominated by enhancement for silicon tips, quenching for CNT tips, and can be tuned via q_0 to either enhancement or quenching for gold-coated tips. In addition, gold-coated tips strongly suppress the emission fluctuations associated with blinking, in agreement with previous observations of QDs adsorbed onto metal surfaces. Our measurements demonstrate explicitly that the lack of fluctuations is due to strong near-field coupling (large β) between the tip and emitter. In principle, the blinking fluctuations should also be suppressed if

the radiative rate becomes large, $\Gamma_r' \gg \Gamma_r$, which might occur in an optical cavity, photonic crystal, or near a plasmonic nanoantenna.

This work was supported in part by an NSF CAREER Award (DBI-0845193) and a Cottrell Scholar Award from the Research Corporation for Science Advancement.

5.6 Supplementary information

5.6.1 Polarization dependence

The parameter $\alpha(z) \equiv \kappa(z)\eta(z)\left[1 + \Gamma_r'(z)/\Gamma_r\right]$ characterizes tip-induced changes to the local excitation intensity, the geometric collection efficiency, and the radiative rate. Thus, it should have a strong polarization dependence, primarily via the intensity enhancement factor $\kappa = I(z)/I_0$. The value of κ should be much larger at short tip-sample separation distances for polarization along the tip axis (i.e., vertical polarization) compared to horizontal polarization. This is evident in Fig. 5.4, which shows the fitted values of α for a gold tip as a function of the vertical height z of the tip above the quantum dot for vertical and horizontal polarization. Vertical polarization yields a strong increase in α at small values of z due to the field enhancement effects discussed in the text, while horizontal polarization yields no enhancement in α, and even a slight decrease. Our measurements do not exhibit a strong polarization dependence for β (data not shown).

5.6.2 Suppression of emission fluctuations during blinking

The approach curves shown in Fig. 5.2(a) demonstrate that for gold tips, the various internal states of the quantum dot that contribute to fluorescence blinking (i.e., those with different q_0 values) yield similar fluorescence count rates near tip-sample contact ($z \to 0$). In particular, the un-normalized fluorescence signal is independent of q_0 when $q_0\beta \gg 1$. Thus, when $\beta \gg 1$, as for a gold tip near tip-sample contact, the emission fluctuations associated with blinking will be strongly suppressed and only those states with the smallest values of q_0 will result in a strong reduction of the fluorescence count rate. This can be seen directly in the fluorescence trajectories, as shown in Fig. 5.5. These data were analyzed by selecting those photons corresponding to $z < 3$ nm (red trajectory) and $z > 100$ nm (blue trajectory) and then computing

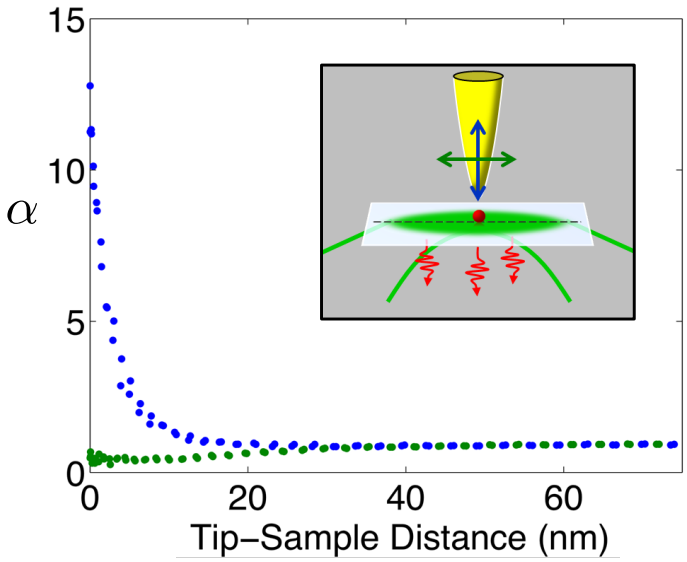

Figure 5.4. Polarization dependence of α. Fitted values for α are shown as a function of the height z of a gold tip above a quantum dot for both vertical (blue circles) and horizontal (green circles) polarization of the excitation field.

the count rate for each trajectory using a 2 ms bin time. It is important to note that the tip oscillation period for these experiments was $\sim$15 μs, so there are over 100 oscillations per time bin.

When the tip is far from the quantum dot, the emission intensity fluctuates between many states and therefore many count-rate values are possible, as shown by the broad histogram of count rates in the right panel of Fig. 5.5 for $z > 100$ nm (blue trace). When the tip is close to the quantum dot ($z < 3$ nm), most of the emission is centered around a particular count rate, and thus the count rate distribution exhibits a pronounced peak (red trace). Note, however, that both distributions also contain a peak at very low count rates: the q_0 values for these states are too small to ensure $q_0\beta \gg 1$ even though $\beta \gg 1$ when the tip is very close to the quantum dot. There are also a number of temporal regions where the two trajectories shown in the left two panels of Fig. 5.5 exhibit clear differences. For example, from $11 - 17$ seconds, the blue trajectory exhibits many fluctuations, while the red trajectory remains relatively constant. Similarly, the prolonged dark period in the blue trajectory from $\sim 21 - 22$ seconds is not mirrored in the red trajectory for most of this period. Note also that

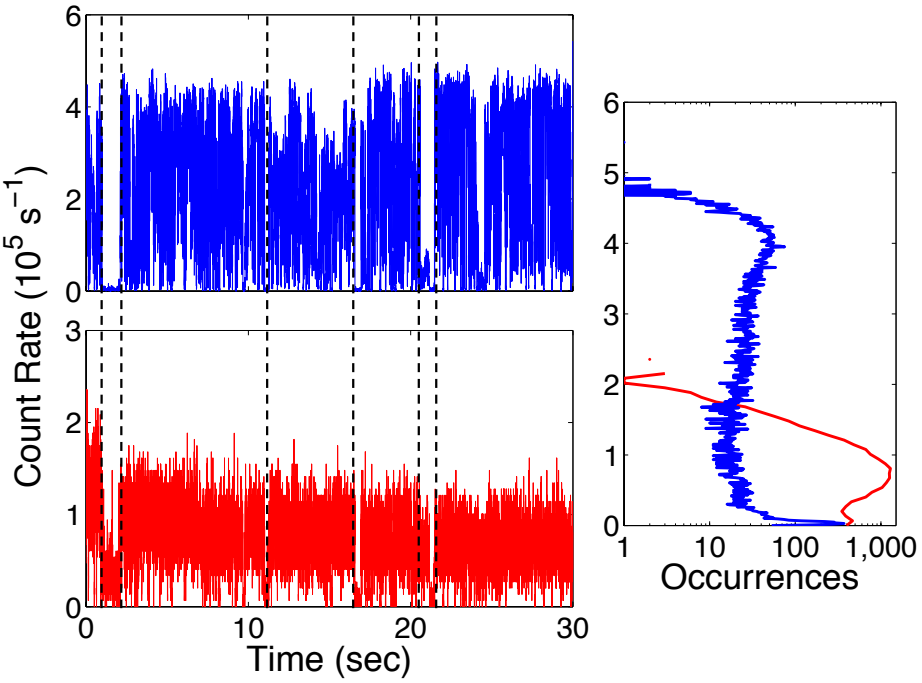

Figure 5.5. Suppression of fluorescence emission fluctuations during blinking. The two left panels show the fluorescence trajectories for $z < 3$ nm (red trace) and $z > 100$ nm (blue trace). The right panel shows the count-rate histogram for the corresponding trajectories on a logarithmic scale. Data were acquired using a gold tip and a bin time of 2 ms.

both trajectories show dark periods from $\sim 1-3$ seconds (and during several other periods), indicating very low emissive states such that $q_0\beta < 1$.

The data shown in Fig. 5.3(b) demonstrate explicitly how the emission fluctuations during blinking are suppressed for $q_0 \gtrsim 0.1$ when a gold tip is brought into (near) contact ($z \sim 0$) with a quantum dot. As the tip-sample distance increases, β decreases and the emission fluctuations will only be suppressed for states with larger q_0 values such that $q_0\beta \gg 1$. When the tip height is large, the tip-sample coupling will vanish ($\beta = 0$), and the fluctuations will no longer be suppressed. This is shown in Fig. 5.6, which plots the fluorescence count rate for several different ranges of z and thus β. Clearly, as z increases (β decreases) both the emission fluctuations and the peak count rate (at $q_0 \sim 1$) increase.

As for the data shown in Fig. 5.3(b), the values of α and β indicated in the caption of Fig. 5.6 were determined by plotting the normalized signal as a function

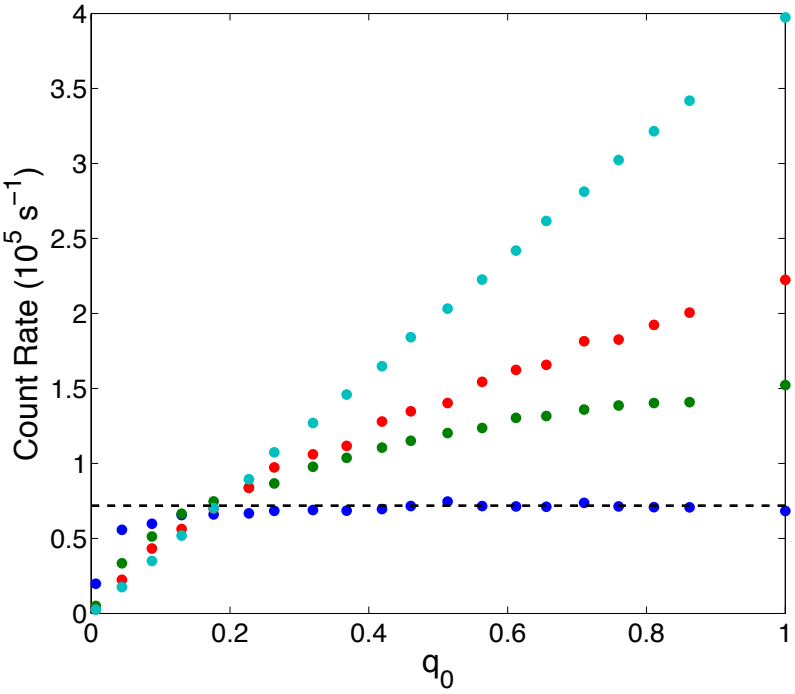

Figure 5.6. Dependence of emission fluctuations on tip-sample separation. The photon count rate is shown as a function of q_0 for four different z-ranges. The different curves correspond to the following z-ranges and (α, β) values: blue - $z < 1$ nm (10.10, 55.83); green - $5 < z < 10$ nm (1.95, 5.45); red - $10 < z < 15$ nm (1.14, 1.15); cyan - $z > 50$ nm (1, 0). The horizontal dotted line corresponds to the ratio α/β times the far-field count rate ($z > 50$ nm) at $q_0 = 1$: $(10.10/55.83)(4 \times 10^5) = 7.2 \times 10^4$ counts/s.

of q_0 for each range of z and then fitting to:

$$S_{\text{norm}} = \frac{\alpha}{1 + q_0\beta}. \tag{5.4}$$

The linear form of the data for $z > 50$ nm reflects the fact that the maximum far-field fluorescence signal is used to calibrate the values for q_0. In particular, the values of q_0 were determined first by selecting photon data from the trajectory with count rates $\geq$70% of the peak rate, and then computing the average count rate for the portion of the selected data corresponding to $z \sim 200$ nm, which is clearly in the far-field limit for these measurements. This average count rate was then set to $q_0 = 1$; all other count rates were assigned a q_0 value in proportion to this $q_0 = 1$ rate.

5.7 References

[1] E. Shafran, B. D. Mangum, and J. M. Gerton, Physical Review Letters **107**, 037403 (2011).

[2] J. M. Gerton, L. A. Wade, G. A. Lessard, Z. Ma, and S. R. Quake, Physical Review Letters **93** (2004).

[3] V. Protasenko, A. Gallagher, and D. Nesbitt, Opt. Commun. **233**, 45 (2004).

[4] V. Protasenko and A. Gallagher, Nano Letters **4**, 1329 (2004).

[5] E. Yoskovitz, D. Oron, I. Shweky, and U. Banin, J. Phys. Chem. C **112**, 16306 (2008).

[6] B. D. Mangum, E. Shafran, C. Mu, and J. M. Gerton, Nano Letters **9**, 3440 (2009).

[7] T. H. Taminiau, F. D. Stefani, F. B. Segerink, and N. F. V. Hulst, Nature Photonics **2**, 234 (2008).

[8] P. Muhlschlegel, H. Eisler, O. Martin, B. Hecht, and D. Pohl, Science **308**, 1607 (2005).

[9] J. Farahani, D. Pohl, H.-J. Eisler, and B. Hecht, Phys. Rev. Lett. **95**, 017402 (2005).

[10] L. Novotny, Phys. Rev. Lett. **98**, 266802 (2007).

[11] N. A. Issa and R. Guckenberger, Opt. Express **15**, 12131 (2007).

[12] P. Anger, P. Bharadwaj, and L. Novotny, Phys. Rev. Lett. **96**, 113002 (2006).

[13] S. Kühn, U. Håkanson, L. Rogobete, and V. Sandoghdar, Phys. Rev. Lett. **97**, 017402 (2006).

[14] R. Carminati, J. Greffet, C. Henkel, and J. Vigoureux, Opt. Commun. **261**, 368 (2006).

[15] E. Purcell, Phys. Rev. **69**, 681 (1946).

[16] H. Gersen et al., Phys. Rev. Lett. **85**, 5312 (2000).

[17] H. G. Frey, J. Paskarbeit, and D. Anselmetti, Applied Physics Letters **94**, 241116 (2009).

[18] E. Shafran, B. D. Mangum, and J. M. Gerton, Nano Letters **10**, 4049 (2010).

[19] Y. Ito, K. Matsuda, and Y. Kanemitsu, Physical Review B **75**, 033309 (2007).

[20] X. Ma, H. Tan, T. Kipp, and A. Mews, Nano Letters **10**, 4166 (2010).

[21] S. Jin, N. Song, and T. Lian, ACS Nano **4**, 1545 (2010).

[22] A. Efros and M. Rosen, Physical Review Letters **78**, 1110 (1997).

[23] G. Schlegel, J. Bohnenberger, I. Potapova, and A. Mews, Physical Review Letters **88**, 137401 (2002).

[24] B. Fisher, H. Eisler, N. Stott, and M. Bawendi, Journal of Physical Chemistry B **108**, 143 (2004).

[25] K. Zhang, H. Chang, A. Fu, A. Alivisatos, and H. Yang, Nano Letters **6**, 843 (2006).

[26] D. Montiel and H. Yang, Journal of Physical Chemistry A **112**, 9352 (2008).

[27] P. Kukura, M. Celebrano, A. Renn, and V. Sandoghdar, Nano Letters **9**, 926 (2009).

[28] T. H. Taminiau, F. D. Stefani, and N. F. Van Hulst, New Journal of Physics **10**, 105005 (2008).

[29] J. Hafner, C. Cheung, T. Oosterkamp, and C. Lieber, Journal of Physical Chemistry B **105**, 743 (2001).

[30] C. Mu, B. D. Mangum, C. Xie, and J. M. Gerton, IEEE Journal of Selected Topics in Quantum Electronics **14**, 206 (2008).

[31] X. Brokmann, L. Coolen, M. Dahan, and J. Hermier, Phys. Rev. Lett. **93**, 107403 (2004).

CHAPTER 6

ENERGY TRANSFER FROM AN INDIVIDUAL QUANTUM DOT TO A CARBON NANOTUBE

The scientific community has become increasingly interested in Carbon nanotubes over the last couple of decades due to their unique 1D properties. Atomic Force Microscopy (AFM) is one of the many applications where CNTs have made a significant impact. The ability to attach a CNT to an AFM probe also opened up the possibility to use them for near-field imaging as has been demonstrated previously in our lab [1]. Our improved data acquisition technique, along with the CNT probes, allows us to take precision measurements of the energy transfer from isolated QDs and a CNT tip. To the best of my knowledge, these were the first measurements of the energy transfer as a function of CNT-emitter distance.

This work was published in Nano Letters, volume 10, pages 4049-4054 (2010). The paper is presented in its entirety in this chapter. Section headings were inserted and the supplementary information was added as an additional section. Reprinted with permission from [2].

6.1 Abstract

Precision measurements of resonant energy transfer from isolated quantum dots (QDs) to individual carbon nanotubes (CNTs) exhibit unique features due to the one-dimensional nature of CNTs. In particular, excitons can be created at varying distances from the QD at different locations along the CNT length. This leads to large variations in energy transfer length scales for different QDs and a novel saturation of the energy transfer efficiency at $\sim$96%, seemingly independent of CNT chirality.

6.2 Introduction

A detailed understanding of energy transduction is crucial for achieving precise control of energy flow in complex, integrated systems. In this context, carbon nanotubes (CNTs) are intriguing model systems due to their rich, chirality-dependent electronic and optical properties. [3–5] Recently, hybrid materials composed of QDs attached to CNTs have been synthesized for a wide range of applications [6–11], including photovoltaics, nanotherapeutics, bioimaging, and photocatalysis. Each component has unique properties that make their combination highly desirable: QDs have broad absorption spectra and size-tunable emission spectra [12], while CNTs can be metallic with ballistic 1D charge transport, or semiconducting depending on the chiral angle of the underlying graphene lattice [3, 5]. The interfacial area in these materials should be extremely large due to the large surface to volume ratio of both QDs and CNTs, so interactions between them are very important for their overall behavior. In particular, the fluorescence emission from QDs is strongly suppressed when they are attached to CNTs, which indicates strong coupling between them. Heretofore, it has not been possible to unambiguously attribute the reduced fluorescence to either charge or energy transfer between the QDs and CNTs, nor to establish limits on the coupling efficiency. If QD-CNT composites are indeed to be pursued for various optoelectronic applications, it is clearly important to understand the energy transduction pathways in more detail.

6.3 Method

It is difficult to extract a detailed understanding of the underlying energy transduction mechanisms using ensembles of QDs attached to CNTs. Therefore, we adopt a single-particle approach whereby we measure the interaction between single QD-CNT pairs. CNTs are first attached to atomic force microscope (AFM) probes via the "pickup" technique [13], and are then brought into close proximity to isolated QDs illuminated with a laser beam of well-defined polarization (6.1(a)). In a typical experiment, the CNT tip is aligned into the center of the focal spot and the sample is raster-scanned until a QD is located topographically with the AFM. An optical

image is then acquired using a unique photon counting technique [14, 15] whereby each detected photon is correlated with the instantaneous vertical and lateral position of the CNT tip relative to the surface of the QD as the tip oscillates vertically in intermittent contact mode with a typical peak-peak amplitude of 40-100 nm. A histogram of photon count rates as a function of tip height, normalized to the rate measured at the far-point of the tip oscillation, is accumulated at each lateral position, producing a 3D data set. The 2D (x-z) fluorescence image in 6.1(b) demonstrates that CNTs attached to AFM probes can be used for nanometer-scale energy transfer microscopy [1]; QD-functionalized probes have been used in a similar manner previously [16]. 1D approach curves can also be extracted from the same 3D data set [15], or by halting the lateral scan when the CNT is centered above the QD (6.2(c)).

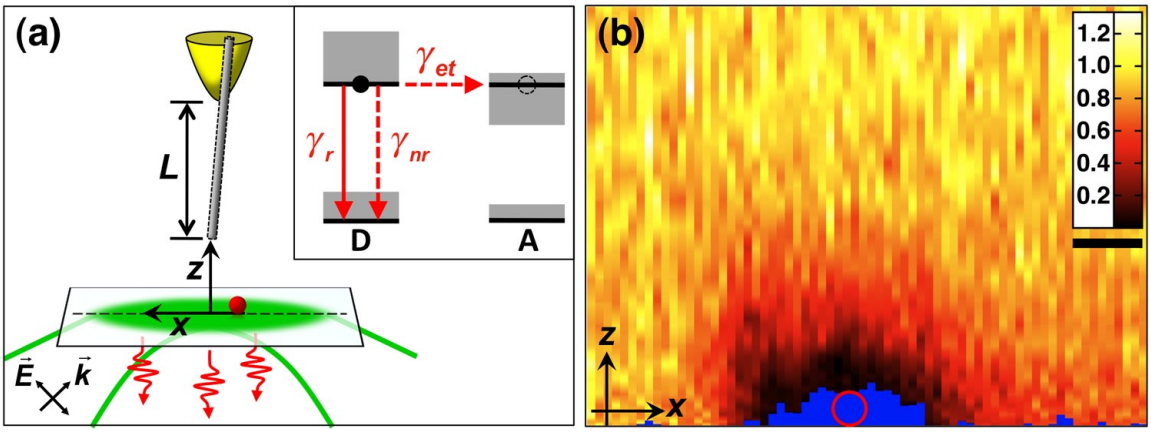

Figure 6.1. Experimental scheme. (a) A CNT protrudes a distance L beyond a gold-coated probe. The probe oscillates along z as an isolated QD is scanned along x. The sample is illuminated with an evanescent field via a focused laser beam whose wave-vector $\mathbf{k}$ is beyond the critical angle for total internal reflection. The polarization of the evanescent wave can be parallel (as shown) or perpendicular to the CNT axis depending on the incident field direction $\mathbf{E}$. A high numerical-aperture lens (not shown) focuses the laser beam and collects the QD emission through a glass coverslip. The inset shows a generic level scheme for energy transfer between a donor (D) and accepter (A): The energy transfer rate γ_{et} competes with the intrinsic relaxation of the QD, $\gamma_0 = \gamma_r + \gamma_{nr}$. (b) Combined topographical and fluorescence image in an x-z plane containing the QD. The CNT traces out the topographical signal indicated by the blue cutout; the red circle denotes the physical size of the QD. The fluorescence signal is normalized to that at the point of maximum CNT-QD separation, as given by the color scale. The scale bar corresponds to 10 nm.

6.4 Results

For this work, six CNTs with final protrusion lengths ranging from $L = 50$ nm to $L = 165$ nm were used for ∼110 high-precision measurements of CdSe/ZnS QD fluorescence as a function of the CNT-QD separation. The chemical vapor deposition growth recipe used to produce our CNT pickup substrates has been shown to produce almost exclusively single-walled CNTs [17]. Based on the expected distribution of CNT chiralities on the growth substrates, there should be both metallic and semiconducting varieties within our sample of picked up nanotubes [3, 18]. CNTs that are not oriented within ∼10 degrees of the vertical axis (i.e., along z in 6.1) tend to buckle under compression during intermittent contact [19] and are not useful for AFM imaging. Thus, it is safe to approximate the CNTs used in these experiments as being vertically oriented.

All six of the CNTs used for this work induce strong quenching of the QD fluorescence at small CNT-QD separations (<25 nm), an example of which is shown in 6.1(b). In addition, lower precision measurements obtained over the last several years using more than 50 CNTs uniformly exhibit similarly strong quenching (data not shown). Only two mechanisms can lead to the observed quenching: energy transfer and charge transfer. Energy transfer can occur when an exciton in the QD resonantly excites an excitation in the CNT via electromagnetic coupling, as in Förster (fluorescence) resonance energy transfer (FRET). In this case, there is no net exchange of charge, resulting in a neutral excitation such as an exciton or plasmon within the CNT. In charge transfer, an electron is exchanged and the resulting excitation within the CNT is associated with an electric current. There are two main signatures in the QD fluorescence signal that can be used to discriminate between these two mechanisms. First, a charged QD will exhibit a relatively low quantum-yield (dark state) until it is neutralized, since excitons within a charged QD undergo fast nonradiative relaxation via an Auger recombination process [20]. Our experiments are performed on glass substrates, so the neutralization time is likely to be a large fraction of the tip oscillation period (∼10 μs), and charging of the QD via electron transfer should produce a delay in the recovery of fluorescence following intermittent

contact of the CNT and QD. Only very rarely is this effect observed [1], and never for the data presented here. Secondly, fluorescence blinking in QDs is thought to be caused by charging of the core via the intermittent trapping of an exciton's electron or hole at the interface. Therefore, the fluorescence blinking dynamics for a charged QD should be altered substantially. An analysis of the blinking statistics of QDs in the presence and absence of CNTs reveals no significant difference in these two cases (Sec. 6.6.2). Thus, we conclude that the dominant quenching mechanism for these experiments is resonant energy transfer, in agreement with several previous studies of fluorescence quenching near nanostructures. [21–24]

Since energy transfer competes with the intrinsic radiative and non-radiative relaxation processes in the QD (6.1(a) inset), the normalized fluorescence signal (S) is generically described by:

$$S = \frac{Q\left(r\right)}{Q_0} = \frac{\gamma_0}{\gamma_0 + \gamma_{et}\left(r\right)} = \frac{1}{1 + \gamma_{et}/\gamma_0}, \tag{6.1}$$

where $Q\left(r\right) = \gamma_r/[\gamma_0 + \gamma_{et}\left(r\right)]$ is the quantum yield of the QD, which depends on the position, r, of the CNT terminus relative to the QD surface, γ_r is the intrinsic radiative relaxation rate of the QD, $\gamma_0 = \gamma_r + \gamma_{nr}$ is the far-field fluorescence rate, γ_{nr} is the intrinsic non-radiative relaxation rate, $\gamma_{et}\left(r\right)$ is the position-dependent energy transfer rate, and $Q_0 = \gamma_r/\gamma_0$ is the far-field quantum yield. The optical excitations within CNTs have been shown to be excitonic in nature [25–28], even for metallic CNTs due to reduced electron screening [29, 30]. Thus, the normalized energy transfer rate is given by the Förster theory for dipole-dipole coupling [31]:

$$\frac{\gamma_{et}}{\gamma_0} = Q_0 \frac{\gamma_{et}}{\gamma_r} = \left(\frac{R_0}{r}\right)^6, \tag{6.2}$$

where R_0 is the Förster radius, and r is the distance between two point dipoles, the donor and acceptor.

Previous work has suggested that the coupling between a dipole emitter and a nanotube or nanowire should result in a lower-order dependence of the energy transfer rate on distance (e.g., r^{-5}) [24]. This results from an integration of the coupling strength along the nanotube, and is appropriate if excitations can be created

anywhere along the length of the CNT with equal probability. Indeed, previous theoretical treatments only considered a geometry where the emitter was located near a (semi)infinite, defect-free CNT at a particular radial distance from its axis, in which case the assumption of uniformity is valid [21, 23, 24]. In our case, the emitter (QD) is located along the CNT axis very close to and beneath its terminus. This edge discontinuity disrupts the uniform excitation distribution, which invalidates an r^{-5} energy transfer dependence for our geometry. In the absence of an explicit model applicable to our unique situation, and with the knowledge that the dominant excitations within CNTs at optical frequencies are strongly localized excitons, we adopt a simple model whereby the energy transfer is a stochastic process that occurs between point dipoles with a probability derived from Eq. 6.2. As described in detail below, this model agrees remarkably well with measurements and allows for novel interpretation of the data.

R_0 depends on a number of factors, including the integrated overlap of donor-emission and acceptor-absorption spectra and the relative orientation of the donor and acceptor transition dipole moments. The explicit dependence on Q_0 given in Eq. 6.2 implies that even for a specific CNT, the position dependence of S will vary from one QD to another, and also for a particular QD during fluorescence blinking and/or oxidation-induced decay. It is important to recognize that for every photoexcitation cycle, the QD will relax either via intrinsic processes *or* via energy transfer to the CNT. Thus, the rates for intrinsic relaxation (γ_0) and energy transfer (γ_{et}) in Eq. 6.2 are averaged over many photoexcitation/energy transfer cycles. Furthermore, each time an energy transfer event occurs, one quantum of energy will be transferred to the CNT in the form of an exciton, which can be created anywhere along the length of the CNT. Therefore, even when the CNT and QD are in contact, the average separation between donor and acceptor dipoles will generally be nonzero due to the physical size of the QD, and the average distance above the CNT terminus at which an exciton is generated. For a vertically aligned CNT centered above a QD, the normalized signal should then be,

$$S = \left[1 + \left(\frac{R_0}{z + z_0}\right)^6\right]^{-1}, \tag{6.3}$$

where z is the vertical distance of the CNT terminus from the QD surface, and z_0 is the effective separation between the donor and acceptor dipoles at $z = 0$.

As the photon histograms are collected, a QD will undergo a series of rapid transitions from a strongly emissive (bright) state to a weakly emissive (dark) one [20, 32]. To simplify interpretation of the data, the photon signal is divided into temporal sections corresponding to bright and dark states using a simple threshold procedure, and separate approach curves are accumulated for each (Fig. 6.2). The dark-state signal shows weaker fluorescence suppression since energy transfer competes less effectively with rapid internal nonradiative decay. To avoid convoluting the analysis, only the bright-state data are compared with the modified Förster model.

The solid curve shown in Fig. 6.2(c) is the best fit to Eq. 6.3 for a particular measurement. The high quality of the fit is typical and Fig. 6.3(a) shows a summary of R_0 and z_0 values extracted from model fits for all six CNTs, where each (z_0, R_0) pair is color coded according to the CNT length, L. The fitted values for R_0 range from 12 nm to ∼40 nm, which are much larger than those for molecular fluorophores in fluorescence resonance energy transfer (FRET) experiments. This indicates strong coupling between the QD and CNT, which requires strong absorption by the CNT at $\lambda \sim 600$ nm [4], the emission wavelength for our QDs.

The measured correlation between z_0 and R_0 evident in Fig. 6.3(a) is a direct result of the 1D nature of CNTs. In particular, the measured signal at each value of z corresponds to many photoexcitation/energy transfer cycles (see Supplementary Material), each of which can result in the creation of an exciton at a different position along the length of the CNT. Stronger coupling between the QD and CNT results in a larger value of R_0, which increases the probability for generating an exciton further up the tube. The values of z_0 extracted from the model fits are clearly much larger than the sum of the QD radius (∼2 nm) and the exciton radius in the CNT (expected to be 1-4 nm depending on the CNT diameter). Thus, although the exciton is most likely to be created near the CNT terminus where the energy transfer efficiency from

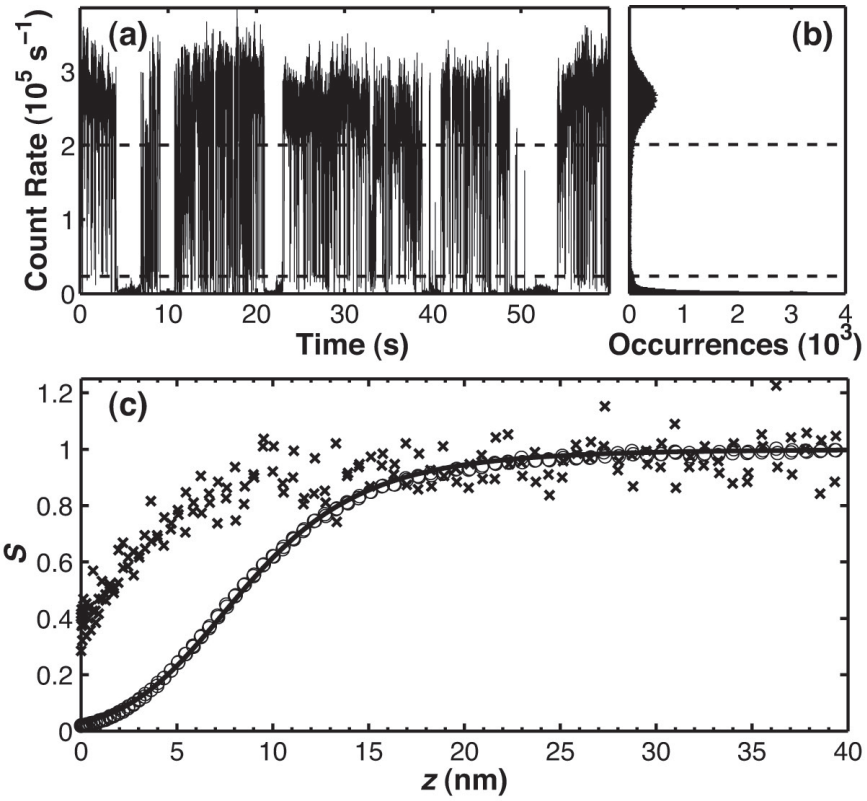

Figure 6.2. Typical approach curves for bright and dark states of a QD. (a) 60-second fluorescence trajectory of a QD demonstrating intermittent changes in its quantum yield. (b) Histogram of count rates using 1 ms time bins. The upper and lower horizontal dashed lines delineate thresholds for the bright and dark states, respectively. (c) Vertical approach curves corresponding to the bright (open circles) and dark (cross) states. The solid line corresponds to a fit to Eq. 6.3 with $R_0 = 19.1$ nm and $z_0 = 10.6$ nm.

the QD is largest, on average it can be created much further up the tube depending on R_0.

A simple estimate of the average position along the CNT at which the exciton is produced can be obtained by calculating the expectation value,

$$\langle \zeta \rangle = \frac{\int_z^\infty \zeta \cdot E\left(\zeta, R_0\right) d\zeta}{\int_z^\infty E\left(\zeta, R_0\right) d\zeta} \tag{6.4}$$

where $E\left(\zeta, R_0\right) = \left[1 + \left(\zeta / R_0\right)^6\right]^{-1}$ is the Förster energy transfer efficiency between point dipoles separated by a distance ζ, and z and R_0 are as defined above. In this context, E is the probability for an energy transfer event between a donor dipole (an exciton within the QD) and an acceptor dipole (an exciton within the CNT) per

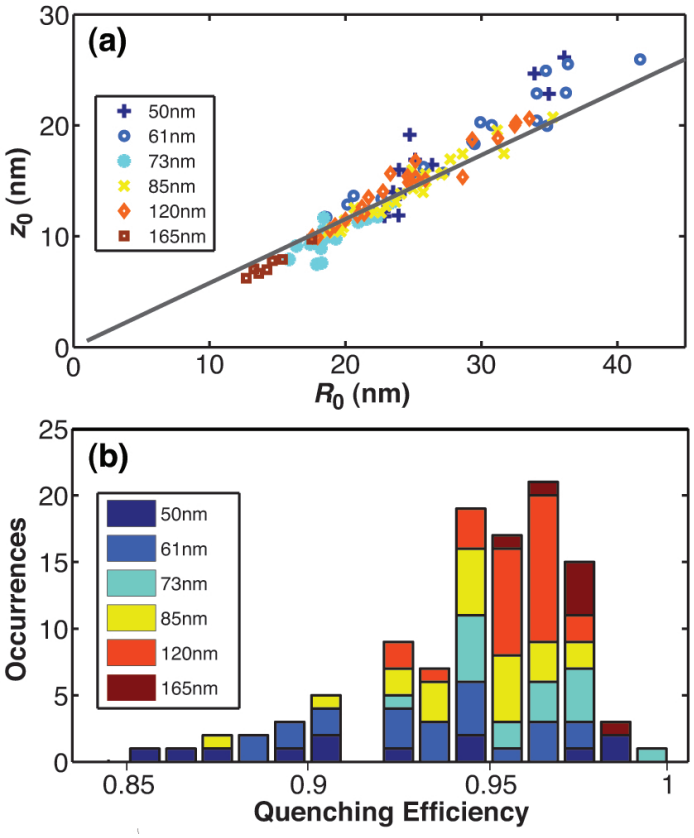

Figure 6.3. Summary of energy transfer measurements for six CNTs of different lengths. (a) Each point gives the value of R_0 and z_0 for a particular measurement extracted from a fit to the Förster model. The points are color-coded according to CNT length. The solid line corresponds to $R_0/\sqrt{3}$, as described in the text. (b) Histogram of the measured quenching efficiencies at QD-CNT contact ($z = 0$). These data comprise 110 measurements on 50 different QDs. Most QDs were measured once or twice; a few were measured over five times with a maximum of 14 times (Fig. 6.4).

photon absorbed by the QD. Evaluating Eq. 6.4 at $z = 0$ gives $z_0 \sim \langle\zeta\rangle_{z=0} = R_0/\sqrt{3}$, which is plotted as the solid line in Fig. 6.3(a). The strong agreement between this simple calculation and the measurements lends confidence to our interpretation of the data.

Interestingly, despite the strength of the QD-CNT coupling, the correlation between R_0 and z_0 causes the energy transfer efficiency to saturate at $z = 0$, in contrast to the FRET efficiency between two point dipoles, which diverge at zero separation. In fact, the simple analysis above predicts that the energy transfer efficiency, $1 - S_{z=0}$, should saturate at a value of $(1 + 3^{-3})^{-1} \cong 0.96$, independent of R_0. Figure 6.3(b) shows a stacked histogram for the *measured* values of the energy transfer efficiency at $z = 0$ for each CNT. There is no obvious dependence of these measurements on CNT length and importantly, the peak energy transfer efficiency for every CNT is consistent with the predicted value of 0.96. Despite the large dynamic range in R_0, which reflects variations in QD-CNT coupling strength, the peak energy transfer efficiency is tightly constrained. An important consequence of this self-limiting behavior is that the peak energy transfer efficiency should be largely independent of CNT chirality, QD-CNT spectral overlap, and the precise alignment of the QD and CNT transition dipole moments. Since it is still very difficult to selectively grow or separate CNTs based on their chiralities, this point may be crucial in terms of using QD-CNT composites for light-harvesting applications.

It is important to recognize that each CNT in Fig. 6.3 was used to measure several individual QDs, each of which likely had a different intrinsic quantum yield, Q_0. Such differences should cause R_0 to vary in proportion to $\sqrt[6]{Q_0}$ (Eq. 6.2), while R_0 is not sensitive to disparities in the absorption cross section from one QD to another since the fluorescence data are normalized in a self-consistent manner. In addition to variations between QDs, oxidative damage can decrease Q_0 for a particular QD as it ages under ambient conditions [33]. Figure 6.4(a) shows a sample of four approach curves for a particular QD as it ages over a period of ∼20 minutes during which a constant illumination intensity was maintained. Also shown in Fig. 6.4(b) are the values of R_0 extracted from all the measurements during this time as a function of

the far-field photon count rate, C_0, and a solid line that is proportional to $\sqrt[6]{C_0}$. A reduction in the absorption cross-section [34] for long aging times (i.e., small values of C_0) would tend to push the data to the left of this line, in agreement with the measurements.

Despite the strong correlation between R_0 and C_0, the energy transfer efficiency saturates at ∼0.96; indeed these data are a subset of those plotted in 6.3. The inset in Fig. 6.4(a) plots the ratio $\gamma_{et}/\gamma_0 = 1/S - 1$, which is very sensitive to minute variations when S becomes small (i.e., near $z = 0$). The remarkable consistency of the saturation value leads to the important conclusion that as γ_0 increases during aging (due to an increase in γ_{nr}), the peak energy transfer rate $\gamma_{et}(z = 0)$ increases proportionally. In FRET experiments between two point dipoles, a smaller value of R_0 indicates weaker coupling between the donor and acceptor, generally implying a smaller energy transfer rate. Here, however, the one-dimensional nature of the CNT leads to a different interpretation: *smaller* values of R_0 yield *higher* average energy transfer rates upon repeated excitation cycles. This occurs because when R_0 is small, the effective center of mass of the exciton distribution within the CNT, $\langle\zeta\rangle$, is *closer* to the end of the CNT and thus closer to the QD, which elevates the *average* energy transfer rate. Within this context, the maximum possible energy transfer rate should occur in the limit that all acceptor excitons are created as close to the QD as possible; i.e., at the tip of the CNT. This corresponds to a minimum dipole-dipole separation $z_{min} \geq 3$ nm: 2 nm for the radius of the QD and ≥1 nm for the exciton radius in the CNT. When R_0 becomes smaller than about $\sqrt{3} \cdot z_{min}$, then the exciton center of mass cannot adjust toward the CNT tip any further. Beyond this point, the energy transfer rate cannot become any larger and the energy transfer efficiency will decrease. Evidently, the slow degradation in Q_0 for the QD in 6.4 is not sufficient to achieve these conditions and the energy transfer efficiency maintains a saturation value of 0.96. Dark states that occur during blinking can have sufficiently small values of Q_0, however, leading to reduced energy transfer efficiency (e.g., Fig. 6.2(c))

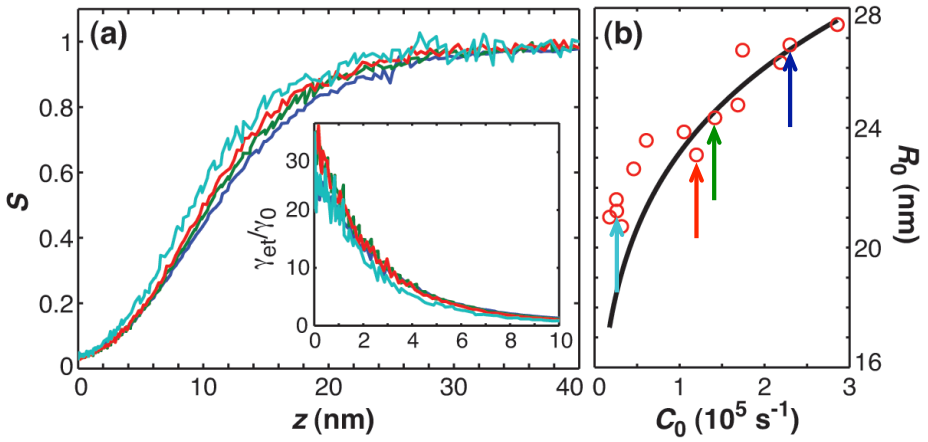

Figure 6.4. Energy transfer measurements during QD aging. (a) Sample of four approach curves showing a continual decrease in R_0 as Q_0 degrades. The inset shows $\gamma_{et}/\gamma_0 = 1/S - 1$ for the corresponding approach curves, where the horizontal axis units are nm. (b) Fitted values of R_0 as a function of the far-field photon count rate, C_0, where the data points highlighted by arrows correspond to the approach curves in (a). As the QD ages over a period of ∼20 minutes, C_0 decreases monotonically by a factor of ∼10, so the data were acquired in order from right to left. Each of the 14 data points in (b) and each separate curve in (a) corresponds to a measurement of ∼1 min in duration. Between each measurement, the CNT is recentered onto the QD, which takes up to 30 s. Thus it takes ∼20 min to complete the 14 measurements.

6.5 Summary

In conclusion, we have made high-precision measurements of energy transfer from QDs to CNTs and have developed a simple model based on dipole-dipole coupling between excitons to explain the observed behavior. Due to the one-dimensional nature of the CNT, the data exhibit novel features that depart from classical Förster theory for energy transfer between point dipoles. In particular, we observe a strong correlation between the measured length scale (R_0) for efficient energy transfer and the average position of the exciton generated within the CNT (z_0). This leads to a narrow distribution of the peak energy transfer efficiency and a counterintuitive increase in the energy transfer rate for smaller values of R_0. Finally, both the model and measurements suggest that the peak energy transfer efficiency should be independent of CNT chirality, which has important implications with regard to the development of QD-CNT composite materials for light-harvesting applications.

6.6 Supplementary information

6.6.1 Experimental details

CNTs are grown on oxidized silicon substrates using methane-based chemical vapor deposition (CVD) and ferric nitrate catalyst nanoparticles. The growth recipe adopted has been shown to produce mostly single-wall CNTs of both semiconducting and metallic chiralities [13, 17], although this has not been independently verified for the current work. Following growth, CNT substrates are imaged with a commercial AFM (Asylum Research, MFP-3D) using gold-coated probes (BudgetSensors, Multi75-GB), and vertically oriented CNT whiskers can be lifted off the substrate by adhering to the sidewalls of the AFM probe. The mechanistic details of the pickup process are not fully understood, although experimental and theoretical studies suggest that relatively large diameter CNTs (3 - 5 nm) are more likely to attach due to the increased CNT-probe interfacial area [17, 19].

Following pickup, the CNT length is measured by pressing the CNT against a smooth Si substrate while measuring the deflection of the AFM cantilever (force curve). When the distal end of the CNT touches the substrate, the cantilever initially begins to deflect. As more force is applied, the CNT will elastically buckle and the cantilever deflection relaxes somewhat resulting in a kink in the approach curve. Depending on its length, a number of additional kinks are possible until finally the apex of the AFM probe comes into contact with the substrate after which a linear deflection of the cantilever is observed as the tip is further pressed into the substrate. The measured distance between the first kink and the linear onset gives the CNT length. When initially attached, CNTs are generally too long to possess sufficient axial stiffness for use in AFM imaging and thus they must be shortened to $<$200 nm. This is achieved by application of short ($\sim$10 μs) voltage pulses of 10 V amplitude between the AFM probe and a doped Si substrate. These pulses induce electrochemical etching of the distal end of the CNT, which leads to shortening in quasi-controllable steps of 10-15 nm and removes any fullerene or catalyst cap. In these experiments, no attempt was made to successively shorten a particular CNT between fluorescence measurements. Rather, each CNT was used for a series of measurements until it was

irreversibly damaged or lost. The lengths of the CNTs utilized extended from 50 to 165 nm, which is approximately the usable range for these types of measurements.

The experimental setup is described in more detail elsewhere [15]. Briefly, the AFM is coupled to a homebuilt inverted optical microscope, which features a 1.4 NA oil-immersion objective, a single-photon counting avalanche photodiode (APD) module (Perkin Elmer, SPCM-AQR14), and a green He-Ne laser (λ = 543 nm). A key element in the setup is a laser beam mask whose transmission profile is a 60° annular section. The inner diameter of the annular section blocks all subcritical rays, resulting in a purely evanescent field at the sample interface within an elongated (1.5 $\times$ 0.5 μm^2) focal area. By rotating the linear polarization of the laser beam, the polarization of the evanescent field can be adjusted to be either vertical (i.e., along the CNT axis) or horizontal (i.e., in the plane of the sample). The QDs employed are nominally 4 nm in diameter and 9 nm long and have an emission maximum at a wavelength of $\sim$605 nm (Invitrogen, QDOT605 ITK). After diluting in toluene to a concentration of $\sim 10^{-9}$ M, 50 μl of the QD solution was then pipetted onto a cleaned and etched glass coverslip and left to dry in a laminar flow hood. The final surface density of QDs on the coverslip was $<$0.1 μm^{-2}. With such a low QD surface density, it is easy to locate isolated QDs using the AFM topography.

Approach curve data were acquired in two related modes: about 30% using tomography mode and 70% using histogram mode. In tomography mode, the sample was raster scanned under the oscillating tip and those pixels corresponding to the top of the QD were isolated in the postexperiment analysis using a height-threshold on the simultaneously acquired AFM topographical data [15]. Vertical approach curves were extracted only from the isolated pixels, following a second filter to reject pixels during which the QD was in a low quantum yield state. Typically, the scan area is 150 nm on a side and consists of 64 or 128 lines acquired at a rate of 0.2-0.8 lines/s. In the postexperiment photon analysis, each raster line was divided into 1,024 lateral pixels, and the height-threshold + quantum yield filter typically yielded between 500 and 1,500 pixels, depending on whether the QD was bright or not, which were averaged to produce an approach curve with 80 vertical bins. In histogram mode, the lateral

raster scan was halted when the CNT was directly above the QD (as determined by the AFM scan) and optical data were accumulated for 60 s. For the histograms, the number of vertical bins was ∼125. For both tomography and histogram modes, the phase sensitive photon counting technique described previously [15] was used to map the accumulated histograms of photon phases to the instantaneous height, z, of the CNT terminus. The uncertainty in z is below 10% based on repeated calibration measurements of the tip oscillation amplitude. Careful comparison revealed no systematic differences between approach curves derived from tomography or histogram modes, aside from better photon statistics for histogram-derived data.

The average far-field ($z \to \infty$) photon count rate for all the experiments was $\sim 250 \times 10^3$ s^{-1}, and the AFM cantilever oscillation frequency was 60-80 kHz. In histogram mode, the data are accumulated for 60 s, so each vertical bin corresponds to a maximum duration of ∼0.5 s, depending on the fraction of time that the QD is in a high quantum yield state during blinking. Thus, a far-field bin in an approach curve (e.g., Fig. 6.2) corresponds to a maximum of $\sim 120 \times 10^3$ photo-counts, and more typically half this value. The number of photoexcitation/energy transfer cycles at any value of z can thus be estimated from the corresponding approach curve by multiplying the quenching efficiency, $1 - S(z)$ by the number of far-field photo-counts. In tomography mode, the estimate requires knowledge of the number of pixels contributing to the approach curve, which can vary substantially as described above.

6.6.2 Evidence against charge transfer

When a QD becomes charged, its quantum yield is reduced significantly because subsequently excited excitons can be non-radiatively quenched via an Auger recombination process [20]. This is, in fact, related to the probable mechanism for QD blinking [32]: an exciton's electron or hole can become trapped in a localized defect state (e.g., dangling bonds) at the surface, leaving a residual charge in the core [20]. In blinking, the quantum yield will remain low (off) until the trapped charge recombines in the core, upon which it returns to a high (on) value. Histograms of the persistence times for both the "on" and "off" states will typically exhibit a power-law dependence

on time, with an exponent of ~ -1.5. Thus, if a charge transfer event between the QD and an approaching CNT occurred, the blinking statistics should be altered inasmuch as the neutralization time is slower than the bin time (inverse sample rate). Figure 6.5 shows a comparison between the on and off persistence times for a particular QD when a CNT is oscillating directly above it during an energy transfer measurement, and when the CNT is not present. To facilitate comparison of the histograms, the CNT data have been multiplied by an appropriate factor, which vertically shifts the data on the log-log scale: no discernible difference between the power-law distributions is observed. The tip oscillation period in this case is $\sim$15 μs, so there are many tip oscillations per 1 ms time bin. Thus, there is no evidence for charge transfer in these measurements, assuming the neutralization time is longer than the 1 ms.

The symmetric shape of the approach curves provides additional evidence against charge transfer. As described in the text and in previous work [14,15], these approach curves are acquired while the CNT-tip oscillates above the QD with a frequency of $\sim$70 kHz. The detected photons are time-tagged and initially correlated with the

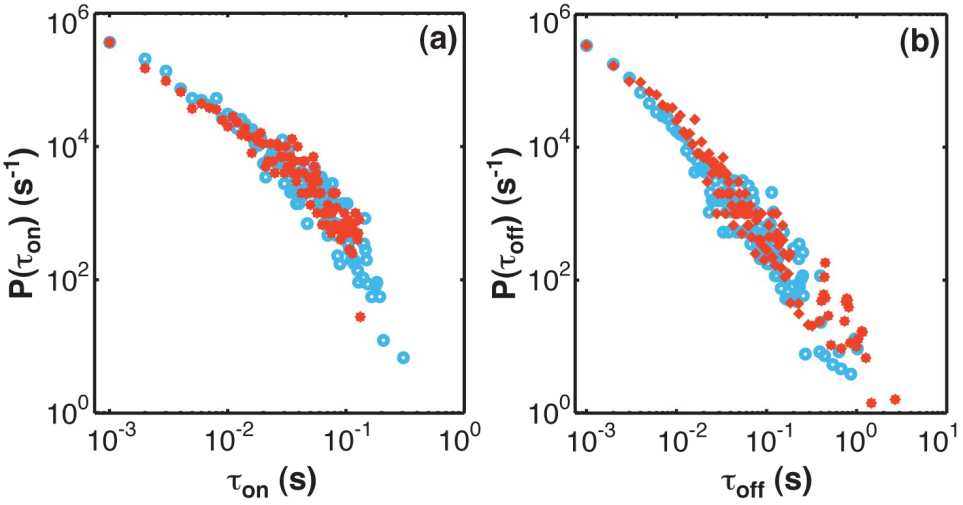

Figure 6.5. Comparison of quantum dot blinking statistics with and without a carbon nanotube. (a) Histogram of persistence times for the "on" state. (b) Histogram of persistence times for the "off" state. In both panels, the open blue circles represent measurements made with the CNT oscillating above the QD during acquisition of an approach curve and the solid red circles are without the CNT present. The vertical axis is the "on" or "off" persistence probability density [35].

instantaneous tip oscillation phase, and these phases are subsequently mapped to the instantaneous height of the tip using the calibrated tip oscillation amplitude. Thus, the measured approach curves contain information on both the approach and retraction of the CNT tip towards and away from the sample surface. If a charge transfer event occurred as a CNT approached the QD, the QD would go dark for some period until the QD charge was neutralized, leading to an asymmetric shape of the approach curve. Note that large asymmetries in some approach curves are sometimes observed (e.g., see Sec. 6.6.6), but we interpret these as resulting from CNT buckling. Either way, none of the data analyzed exhibited such asymmetry, so we conclude that there is no charge transfer if the neutralization time is longer than the tip-oscillation period, or $\sim$8 μs. Since our QDs sit atop a nonconductive glass substrate, and since the experiments are performed in a relatively low humidity environment ($<$10%), neutralization times shorter than this are not expected.

6.6.3 Possible systematic effects

To enhance our interpretation of the measurements, a number of possible systematic effects were investigated. First, our data acquisition procedure rules out the possibility that the observed saturation value of $\sim$0.96 is due to systematic factors such as stray light and noise. In particular, the background signal is measured immediately after acquiring each data set, and is then subtracted from the approach curve data. Typical far-field count rates are $\sim 250 \times 10^3$ s^{-1} and typical background count rates are 10^3 s^{-1}. Thus, the maximally quenched signal ($0.04 \times 250 \times 10^3 = 10^4$ s^{-1}) is still about 10 times higher than the background. Furthermore, we have successfully measured peak quenching efficiencies of $\gtrsim$0.99 using this same procedure with metallic tips, which also rules out other systematic limitations on the measurements such as lateral and vertical binning. An example for the strong quenching can be observed in Fig. 6.6 for horizontal polarization. Second, under these conditions, gold-coated tips decrease the local illumination intensity when they are between $\sim$30 and $\sim$200 nm above the sample [15, 36]. To account for this, intensity profiles were measured using bare gold-coated tips, and proper normalization functions for the data were

generated (Fig. 6.6). This normalization procedure yields a larger uncertainty for shorter CNTs, resulting in a broader distribution of measured quenching efficiencies, as shown in Figure 3(b). At very short range, a gold-coated tip can increase the local illumination intensity (for vertical polarization), and can also quench the fluorescence emission directly, but since the shortest CNT in our study is 50 nm long, these effects can be neglected. Optical scattering from the CNT itself might also modify the illumination intensity and/or the QD radiative rate γ_r, particularly for vertically polarized illumination. No dependence of the measurements on polarization direction is observed (Sec. 6.6.5), and indeed the data summarized in Figure 3 contain many measurements using each polarization. This demonstrates that any CNT-induced modification to the illumination intensity or γ_r is either too weak or too confined near the CNT terminus to be detected at the QD core, and also that the emission dipole moment of the QD is not correlated with the excitation polarization. Finally, it is possible for a CNT to buckle under a compressive axial load, such as applied during AFM imaging. Indeed, buckling events lead to easily detectable asymmetry in the shape of measured approach curves, since these contain information corresponding to both the approach and retraction of the CNT during its oscillation cycle (Sec. 6.6.6), and also correlate strongly with poor AFM performance. None of the measurements

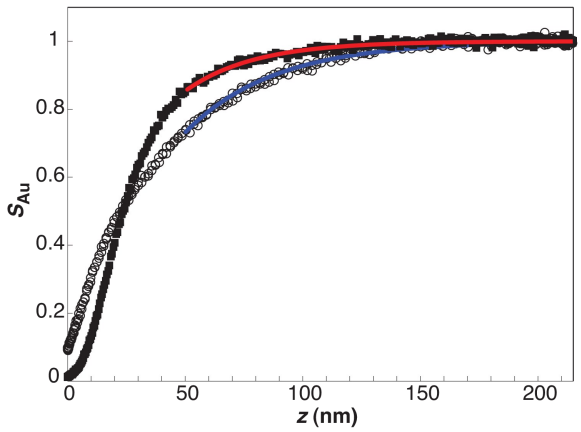

Figure 6.6. Approach curves for a bare gold tip. The open circles correspond to illumination with vertical polarization and the solid squares are for horizontal polarization. The solid lines are fits to an exponential decay function of the form, $S_{Au}(z) = 1 - A\exp(z/z_d)$ in the range $z > 50$ nm.

summarized in Figure 6.3 exhibit the signatures of buckling. The normalization procedure, polarization measurements, and nanotube buckling measurements are described in more detail below.

6.6.4 Normalization procedure

The modified Förster model developed in the text predicts a signal of the form,

$$S = \left[1 + \left[R_0/\left(z + z_0\right)\right]^6\right]^{-1}, \tag{6.5}$$

which assumes that the fluorescence signal is properly normalized to the far-field value (i.e., $z \to \infty$), and that the detected signal is due purely to an interaction between the QD and CNT. However, it has been shown that metal tips can also quench fluorescence at short distances and can also modify the local optical intensity at the QD for distances up to ∼200 nm [15]. Since the shortest CNT used in our study was 50 nm long, we are only interested in the long-range effects and can neglect quenching. In particular, as it approaches the QD, the gold tip to which a CNT is attached suppresses the fluorescence signal, as seen in Fig. 6.6. Due to the long length scale for this effect, we believe it results from a reduction in the local intensity at the QD caused by interference between the excitation light and the light scattered off the tip, rather than from energy transfer from the QD to the gold tip. The scattering from the tip is expected to be stronger for vertically polarized light compared to horizontal polarization, which leads to the longer decay length seen in Fig. 6.6.

The approach curves in Fig. 6.6 for both vertical and horizontal polarization are described well by an exponential decay function, $S_{Au}(z) = 1 - A\exp(z/z_d)$, for $z > 50$ nm. Thus, to account for the gold-induced intensity suppression, the approach-curve data for CNT tips was first fit to $S_{Au}(z + L)$, where L is the measured length of the specific CNT, and the parameters A and z_d are extracted from the fit. Only data in the range $z > 25$ nm are used in the fit, since in this range the contribution from the CNT is smaller than that from the gold. The measured signal is then normalized by the contribution of the gold for the entire range of the measurement: $S(z) = S_{CNT}(z)/S_{Au}(z + L)$.

6.6.5 Dependence on illumination polarization

There are two primary possibilities that could lead to a polarization dependence in the CNT approach curve measurements. First, direct scattering of the excitation light by the CNT should lead to field enhancement at the CNT terminus via the lightning-rod effect when the polarization is parallel to the CNT axis. For transverse polarization, no field enhancement should result and in fact a reduction in excitation intensity might occur. Secondly, if the emission dipole orientation of the QD is correlated with its absorption dipole, then R_0 should depend on the excitation polarization direction via the dipole-dipole orientation overlap factor. The data presented in the manuscript were composed of many measurements with both axial and transverse polarization directions and no systematic difference was observed. To demonstrate this, Fig. 6.7 shows the measured values of peak quenching efficiency (at $z = 0$) and the quenching decay length for each CNT and both polarization directions. The decay length is the measured tip-sample separation at half the peak quenching efficiency.

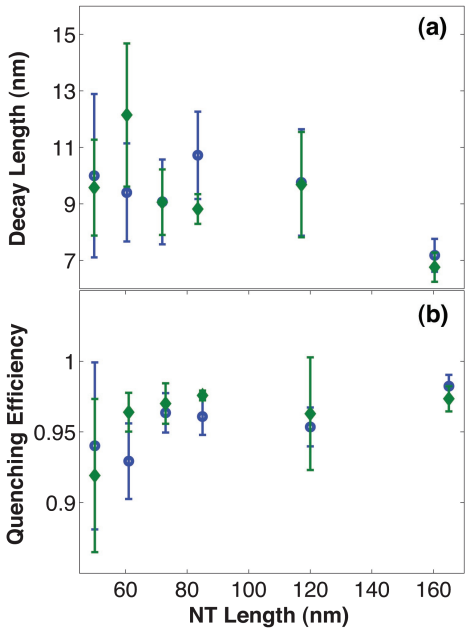

Figure 6.7. Polarization dependence of energy transfer measurements. (a) Decay length, and (b) peak quenching efficiency for both axial (green diamonds) and transverse (blue circles) excitation polarization. The error bars represent the standard deviation of the measurements for each CNT length.

6.6.6 Nanotube buckling

Occasionally, we observe obvious asymmetry in the shape of an approach curve, as shown in Fig. 6.8. In addition, asymmetric approach curves correlate strongly with poor AFM performance across the entire sample, not just above a QD. Thus, we interpret such data as resulting from buckling of the CNT while the cantilever oscillates during intermittent contact mode AFM imaging. It is important to recall that all the measurements are obtained in this mode and that the approach curves are acquired by correlating the arrival times of the detected photons with the instantaneous phase of the tip oscillation. Thus, if the CNT buckles as the cantilever swings through its downward trajectory (i.e., toward the sample surface), then upon retraction, it will elastically unbuckle at some point and lift away from the surface. As is often observed for normal AFM tips, the CNT is likely to adhere to the surface upon retraction, until the cantilever spring constant overwhelms the adhesion forces, at which point the CNT will release from the surface. This causes an asymmetry in the phase histogram and associated approach curve: the approach side of the curve exhibits a smooth decay in the fluorescence with a shape characteristic of a normal (nonbuckled) measurement, while the retraction side of the curve is more steep. In addition, there is a flat bottom to the approach curve corresponding to the duration of time during which the CNT is in a buckled state, and apparently some portion of the CNT is in direct contact with the QD. Occasionally the flat portion of the approach curve exhibits more complicated features, which presumably correspond to the CNT tip sliding away from the QD location. In addition, we observe a higher rate of buckling with larger tip-oscillation amplitudes and harder tapping (lower set point for the oscillation amplitude relative to the free amplitude), and a corresponding increase in the width of the flat portion of the approach curve.

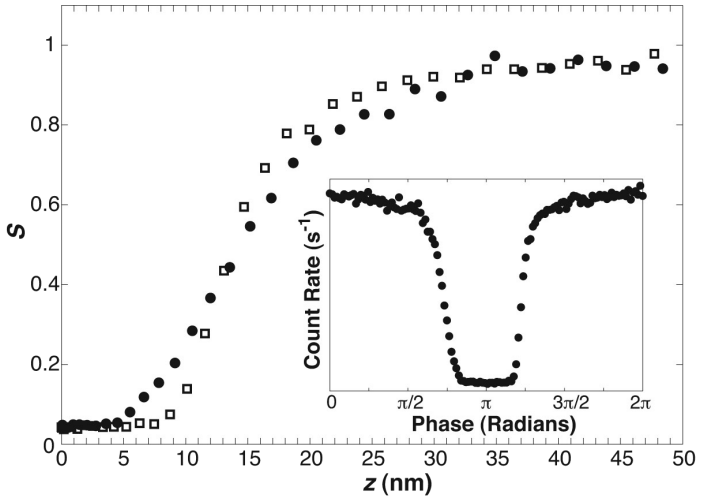

Figure 6.8. Buckling of a CNT during an approach curve measurement. The closed circles correspond to approach of the CNT toward the QD, while the open squares correspond to its retraction. The precise location of QD-CNT contact is difficult to determine in this case. The inset is the phase histogram generated during the measurement from which the approach curves are extracted. This phase histogram is generated by correlating the arrival times of detected photons with the instantaneous phase of the tip oscillation.

6.7 References

[1] C. Mu, B. D. Mangum, C. Xie, and J. M. Gerton, IEEE Journal of Selected Topics in Quantum Electronics **14**, 206 (2008).

[2] E. Shafran, B. D. Mangum, and J. M. Gerton, Nano Letters **10**, 4049 (2010).

[3] R. Saito, G. Dresselhaus, and M. S. Dresselhaus, *Physical Properties of Carbon Nanotubes*, Imperial College Press, London, 1998.

[4] S. Bachilo et al., Science **298**, 2361 (2002).

[5] P. Avouris, M. Freitag, and V. Perebeinos, Nature Photonics **2**, 341 (2008).

[6] V. Biju, T. Itoh, Y. Baba, and M. Ishikawa, Journal of Physical Chemistry B **110**, 26068 (2006).

[7] M. Grzelczak et al., Advanced Materials **18**, 415 (2006).

[8] J. M. Haremza, M. A. Hahn, and T. D. Krauss, Nano Letters **2**, 1253 (2002).

[9] M. Olek, T. Busgen, M. Hilgendorff, and M. Giersig, Journal of Physical Chemistry B **110**, 12901 (2006).

[10] F. Li, D. I. Son, S. H. Cho, W. T. Kim, and T. W. Kim, Nanotechnology **20** (2009).

[11] X. Peng, J. Chen, J. A. Misewich, and S. S. Wong, Chemical Society Reviews **38**, 1076 (2009).

[12] D. Norris and M. Bawendi, Physical Review B **53**, 16338 (1996).

[13] J. H. Hafner, C. Cheung, T. H. Oosterkamp, and C. M. Lieber, The Journal of Physical Chemistry B **105**, 743 (2001).

[14] J. M. Gerton, L. A. Wade, G. A. Lessard, Z. Ma, and S. R. Quake, Physical Review Letters **93** (2004).

[15] B. Mangum, E. Shafran, C. Mu, and J. Gerton, Nano Letters **9**, 3440 (2009).

[16] Y. Ebenstein, T. Mokari, and U. Banin, Journal of Physical Chemistry B **108**, 93 (2004).

[17] L. Wade, I. Shapiro, Z. Ma, S. Quake, and C. P. Collier, Nano Letters **4**, 725 (2004).

[18] Y. Narui, D. M. Ceres, J. Chen, K. P. Giapis, and C. P. Collier, Journal of Physical Chemistry C **113**, 6815 (2009).

[19] S. Solares, Y. Matsuda, and W. Goddard, The Journal of Physical Chemistry B **109**, 16658 (2005).

[20] D. E. Gomez, M. Califano, and P. Mulvaney, Physical Chemistry Chemical Physics **8**, 4989 (2006).

[21] I. Bondarev, G. Slepyan, and S. Maksimenko, Physical Review Letters **89** (2002).

[22] E. Yoskovitz, D. Oron, I. Shweky, and U. Banin, The Journal of Physical Chemistry C **112**, 16306 (2008).

[23] P. L. Hernandez-Martinez and A. O. Govorov, Physical Review B **78** (2008).

[24] R. S. Swathi and K. L. Sebastian, Journal of Chemical Physics **132** (2010).

[25] O. J. Korovyanko, C. X. Sheng, Z. V. Vardeny, A. B. Dalton, and R. H. Baughman, Physical Review Letters **92** (2004).

[26] F. Wang, G. Dukovic, L. E. Brus, and T. F. Heinz, Science **308**, 838 (2005).

[27] T. Ando, Journal of the Physical Society of Japan **66**, 1066 (1997).

[28] H. B. Zhao and S. Mazumdar, Physical Review Letters **93** (2004).

[29] F. Wang et al., Physical Review Letters **99** (2007).

[30] H. Zeng, H. Zhao, F.-C. Zhang, and X. Cui, Physical Review Letters **102** (2009).

[31] J. R. Lakowicz, *Principles of Fluorescence Spectroscopy*, Kluwer Academic/Plenum Publishers, New York, 1999.

[32] M. Nirmal et al., Nature **383**, 802 (1996).

[33] W. van Sark et al., Journal of Physical Chemistry B **105**, 8281 (2001).

[34] P. Kukura, M. Celebrano, A. Renn, and V. Sandoghdar, Nano Letters **9**, 926 (2009).

[35] J. J. Peterson and D. J. Nesbitt, Nano Letters **9**, 338 (2009).

[36] F. H'dhili, R. Bachelot, A. Rumyantseva, G. Lerondel, and P. Royer, J. Microsc-Oxford **209**, 214 (2003).

CHAPTER 7

CONTROLLING ANGULAR EMISSION OF QUANTUM DOTS WITH SHARP TIPS

In previous chapters we have seen that a near-field probe can focus light to a subdiffraction volume and modify the excitation and emission rates of a single molecule. Moreover, the angular emission from single molecules can be influenced by coupling to the near-field probe [1, 2]. Taminiau et al. showed that when an optical antenna is brought in proximity to a single emitter, the emitter couples to resonance modes in the antenna, which in turn emits the radiation along a well defined direction [2]. Therefore, the resulting angular emission is predominantly determined by the antenna and not the properties of the emitter. An alternative approach to alter angular emission is to fabricate a plasmonic metallic structure on the sample surface and place it in the focal spot of a microscope objective. This also enables redirection of single molecule emission via coupling to plasmonic modes [3,4] and even wavelength sorting [5] but is typically restricted to ensemble measurements. Recently, Curto et al. [6] demonstrated that by driving an optical Yagi-Uda antenna with single QDs, it is possible to achieve unidirectional emission.

Within the class of quantum emitters, QDs are of particular importance due to their size dependent optical properties [7]. Furthermore, their large absorption cross-section, narrow emission peak, high quantum yield and good photostability makes them attractive for biological applications [8,9]. For near-field experiments, QDs have an additional advantage over single molecules; while QDs are passivated with a few atomic layers of an inorganic material of a higher band gap to insure high quantum yield and photostability, single molecules are typically dispersed in a few nm of a "protective" polymer (e.g., PMMA). Therefore, the minimal tip-emitter distance in

the case of a single molecule sample is fairly large in comparison to QDs and any short range phenomena might seem weak or even go completely undetected. Here, we study the effects of a near-field probe on the angular emission of individual QDs. Our unique data acquisition technique allows us to observe changes as a function of tip-QD distance down to tip-QD contact. We primarily focus on the reorientation of the angular emission as a function of the vertical distance from gold coated tips. To get a better understanding of the origin of the redirection, we compare the results for gold tips with those of silicon and carbon nanotubes (CNT) tips. Our results suggest that we see reorientation of the angular emission due to a dielectric effect. In previous work, we showed that gold tips can suppress the emission fluctuations from QDs when placed within a few nm of the QD [10]. Here, we show that at small tip-QD distance, the emission properties of the QD resemble those of a linear transition dipole.

7.1 Introduction

The optical transition rate for a quantum emitter is proportional to $|\mathbf{p}\cdot\mathbf{E}|^2$, where $\mathbf{p}$ is the transition dipole and $\mathbf{E}$ is the excitation or emission electric field. The transition dipole of single molecules is typically oriented along a specific axis, creating a linear transition dipole both in excitation and emission. On the other hand, spherical (or almost spherical) QDs have unique absorption and emission properties; the excitation transition dipole when exciting near the band edge is spherically degenerate [11] while the emission dipole is 2D degenerate [12–14]. The excitation polarization is decoupled from the emission polarization and changes in the excitation polarization lead to no observable change in the emission [12]. The emission dipole is usually characterized by a "dark axis" (c-axis) with no emission along that axis, and a "bright plane," with degenerate transition dipoles. However, several experiments have demonstrated that by changing the shape of the nanocrystal or the environment, the angular emission properties of the nanocrystals can be changed. For example, when the core of the nanocrystal is elongated, theory predicts energy level crossing, which results in polarized emission along the elongated axis [15]. A similar effect was also observed for nanocrystals with spherical cores and an elongated shell [16]. For QDs embedded

on a rough metal film, the 2D emission degeneracy is converted into linearly polarized emission [17], which is believed to arise primarily from the electric dipole polarization of the metal that couples to the radiation of the QDs.

In order to investigate the emission polarization state of an emitter, the collected emission can be recorded as it passes through a rotating linear polarizer. The changes in the signal due to the polarizer arise from the projection of the transition dipole on the x-y plane. A linear dipole oriented along the z-axis will have a radiation pattern with azimuthal symmetry (with respect to the z-axis), and no modulation in the intensity will be observed as the polarizer is rotated. In contrast, a dipole oriented in the x-axis will predominantly emit light along the y-axis with polarization along the x-axis, and the modulation in the signal will follow $\cos^2\theta$, where θ is angle between the dipole and the polarizer axis. One can define the degree of polarization (DOP) by

$$\mathrm{DOP} = \frac{I_{\max} - I_{\min}}{I_{\max} + I_{\min}} \tag{7.1}$$

where $I_{\max}$ and $I_{\min}$ are the maximum and minimum emission intensities. For linear emission dipoles oriented along either the x- or y- axis, $I_{\min} = 0$ and DOP is unity. For molecules oriented more towards the z-axis or with higher symmetry, the modulation in the signal is less pronounced due to the existence of a dipole component in both x and y axis of the sample plane.

Figure 7.1 illustrates the hexagonal structure of a CdSe nanocrystal and its emission properties. The "dark axis" lies along the slightly elongated direction of the nanocrystal, whereas the "bright plane" is perpendicular to the elongated axis (Fig. 7.1a). The projection of the "bright plane" on the sample plane appears as an ellipsoid (Fig. 7.1b), where the ratio between the long and the short axes depends on the angle between the c-axis and the z-axis (depicted as ϕ). Figure 7.1c illustrates the emission intensity modulation as a function of a rotating polarizer placed in the emission path. For spherical QDs, the degree of polarization value can be 0 if the "dark axis" is oriented along the z-axis, and can be as large as DOP ~ 0.5, when the "dark axis" is in the horizontal plane [12].

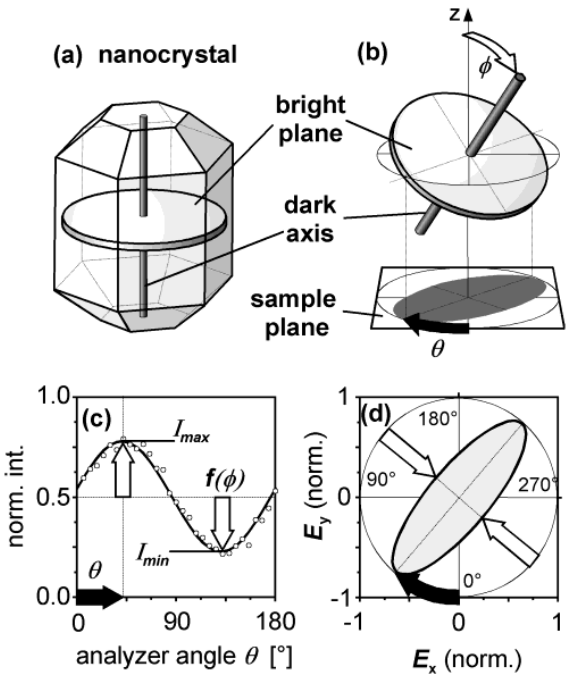

Figure 7.1. Structure and emission properties of CdSe nanocrystal. (a) Hexagonal structure of CdSe nanocrystals. The "dark axis" (c-axis) is aligned along the elongated direction of the nanocrystal, whereas the "bright plane" is perpedicular to it. (b) An example of a nanocrystal with angle ϕ between the c-axis and the z-axis. The projection of the "bright plane" takes an ellipsiod shape. (c) Modulation in the emission intensity as a function of polarization angle θ. (d) Enlarged view of the projection of the "bright plane" on the sample plane. Reprinted with permission from [14]. Copyright 2003 American Chemical Society.

7.2 Experimental details

The experimental setup is similar to that described in Sec. 3.1. The sample is illuminated with evanescent illumination (Sec. 3.2) at $\lambda_{\text{exc}} = 543$ nm and the excitation polarization is vertical with respect to the tip for all the data shown here. To acquire the DOP, a polarization beam splitter was placed in the emission pathway, and the signal was split into two orthogonal polarizations. Each polarization was then recorded by a separate APD and the two photon channels were time stamped as described in Sec. 3.4. In such a setup, the emission is split into orthogonal polarizations, but not necessarily into I_{max} and I_{min}. Equation 7.1 needs to be modified as follows:

$$\text{DOP} = \left| \frac{I_1 - I_2}{I_1 + I_2} \right| \tag{7.2}$$

where I_1 and I_2 denote APD 1 and 2, respectively.

We use two different types of data acquisition modes in this experiment: approach curves and SP-NFT. These have been described in details in Sec. 3.4.1 and Sec. 3.4.2 respectively. The samples were prepared by diluting CdSe/ZnS (invitrogen) in toluene and dispersing them on a glass slide. The emission peak of the QDs is at 605 nm.

7.3 Results

Figure 7.2 displays the measured DOP values of a QD as a function of the distance from a gold tip. We utilize the fluorescence blinking events of a QD to separate the data into high emissive and low emissive internal states [10]. The intrinsic quantum yield of the low state is about 30 times lower than the high quantum yield state as determined from the far-field values. Figure 7.2a-b shows the measured signal for the high emissive (Fig. 7.2a) and the low emissive (Fig. 7.2b) states, where APD 1 is represented by blue and APD 2 by green. The DOP as a function of tip-QD distance can be computed by inserting the approach curves from Fig. 7.2a-b into Eq. 7.2. The results are summarized in Fig. 7.2d, where the blue circles represent the high emissive state and red line represents the low emissive state. Although the near-field signal looks very different for the two states, the high quantum yield state is dominated by quenching (Fig. 7.2a) whereas in the low quantum yield state signal enhancement

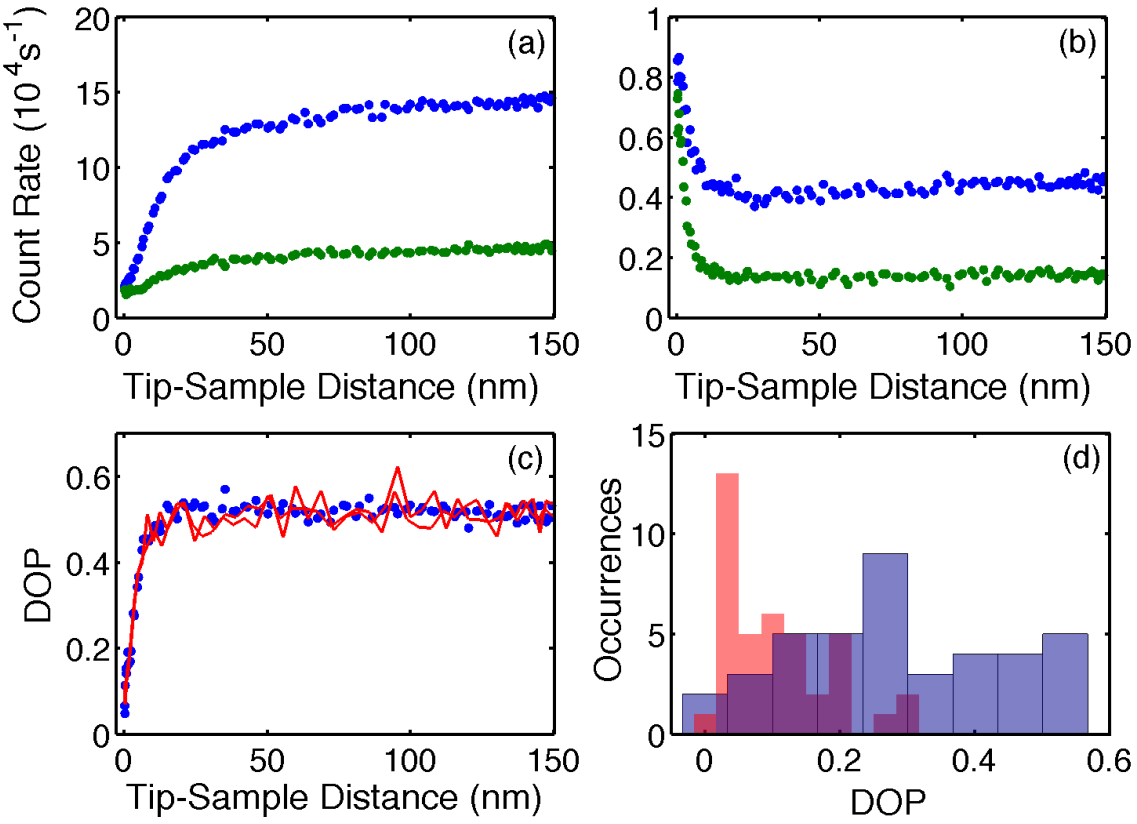

Figure 7.2. Polarization changes due to gold tip. Approach curve for the high emissive (a) and the low emissive states (b). The signals recorded on APD 1 and APD 2 are depicted by blue and green circles, respectively. The approach curves from the different channels are converted into DOP values using Eq. 7.2. Panel (c) shows the DOP results for the high emissive state (blue circles) and the low emissive state (dotted red line). Histogram of near-field (red) and far-field (blue) DOP values from 40 measurements are summarized in panel (d).

outweighs quenching (Fig. 7.2b), the DOP curve looks similar in both cases except for increased noise in the low emissive state, which is due to worse photon statistics. In both cases, as the tip gets closer to the QD, the DOP value approaches 0, which is a signature of a linear dipole oriented along the z direction. In order to insure the changes in the emission polarization are reproducible, we compared the the near-field DOP ($z < 2$ nm) with the far-field DOP ($z > 50$ nm), from 40 different measurements. A histogram of the near-field and far-field values is plotted in Fig. 7.2d. It is clearly evident that the far-field (blue) values have a much larger distribution, whereas the near-field values have a narrow distribution with DOP ~ 0.05 as the most frequently occurring value.

We performed similar measurements using silicon and CNT tips. While silicon, in contrast to gold, does not support plasmon resonance effects in the optical spectrum, the dielectric function of silicon is much larger than that of the CdSe/ZnS and should result is a large dielectric mismatch at the QDs boundary. In addition, silicon tips have relatively weak near-field coupling with QDs [10]. On the other hand, CNT tips have a much smaller size in comparison to silicon and gold probes, and should not give rise to a large dielectric mismatch. The results in those two cases are shown in Fig. 7.3. For silicon, the tip leads to changes in the DOP value, with DOP value of DOP ~ 0.2 at $z = 0$. Although there is an effect, the modification is not as dramatic as compared to the gold probes (Fig. 7.2c). The CNT tip does not modify the DOP value (Fig. 7.3d). Despite the fact that CNT strongly couple to the QD [18], as is apparent from the strong quenching shown is Fig. 7.3b, the changes in the two channels are proportional to each other and therefore the DOP value stays the same.

Figure 7.4 is an x-z slice of the tip-QD interaction. The sum of the signal from the two polarization channels (i.e., $I_1 + I_2$) is plotted in Fig. 7.4a. The intensity was normalized to the far-field value as explained in Sec. 3.4.2. The DOP values can be seen in Fig. 7.4b. In this case, the far-field DOP of the QD is DOP ~ 0.3. When the tip is oriented to the side of the QD, the degree of polarization changes from the far-field value to about $P \sim 0.4$. On top of the QD, $P \sim 0.1$ in a similar way to the data shown in Fig. 7.2. The far-field DOP ($z > 50$ nm) and the near-field DOP

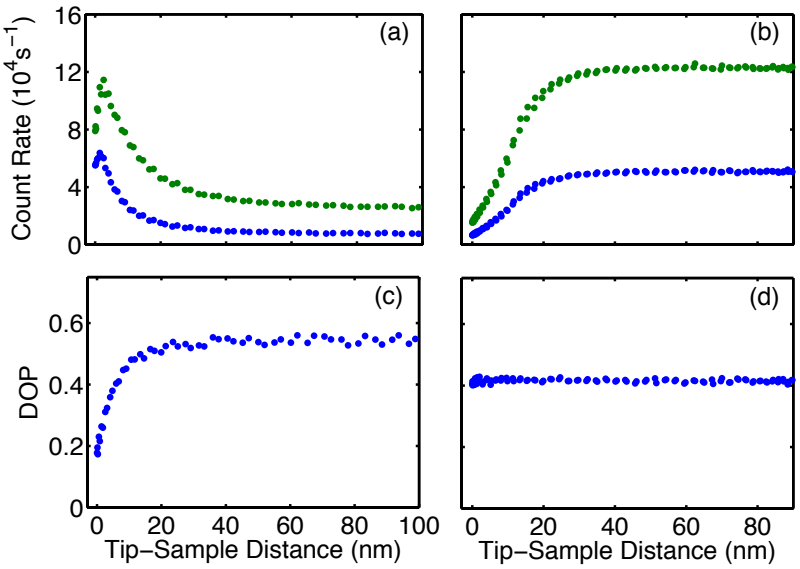

Figure 7.3. Polarization changes due to silicon and CNT tips. The approach curves for silicon (a) and CNT (b) tips. Blue and green circles represent the signal recorded on APD 1 and APD 2, respectively. The DOP values in the presence of the silicon tip (c) are decreasing in a similar way to those in the presence of the gold tip, yet the effect does not seem as strong. For the CNT tip, the DOP does not change (d).

($z < 2$ nm) are extracted from Fig. 7.4b and plotted in Fig. 7.4c as a function of x. There is a significant change in the near-field DOP (blue curve), which depends on the exact position of the tip with respect to the QD. The far-field DOP (green curve) is plotted for comparison.

Figure 7.5 compares the near-field signal (green curve) extracted from Fig. 7.4a with the near-field DOP (blue curve) extracted from Fig. 7.4b. It is obvious that the changes to the DOP do not correlate with changes in the near-field signal.

7.4 Discussion

The gold coated tips used in this experiment do not support a particular plasmon resonance mode. Therefore, it is not likely that the modification of the angular emission shown here is due to an antenna effect. On top of that, when the QD is in a low intrinsic quantum yield state, the strong intrinsic nonradiative decay should compete with the coupling efficiency to the antenna. Such behavior should lead to

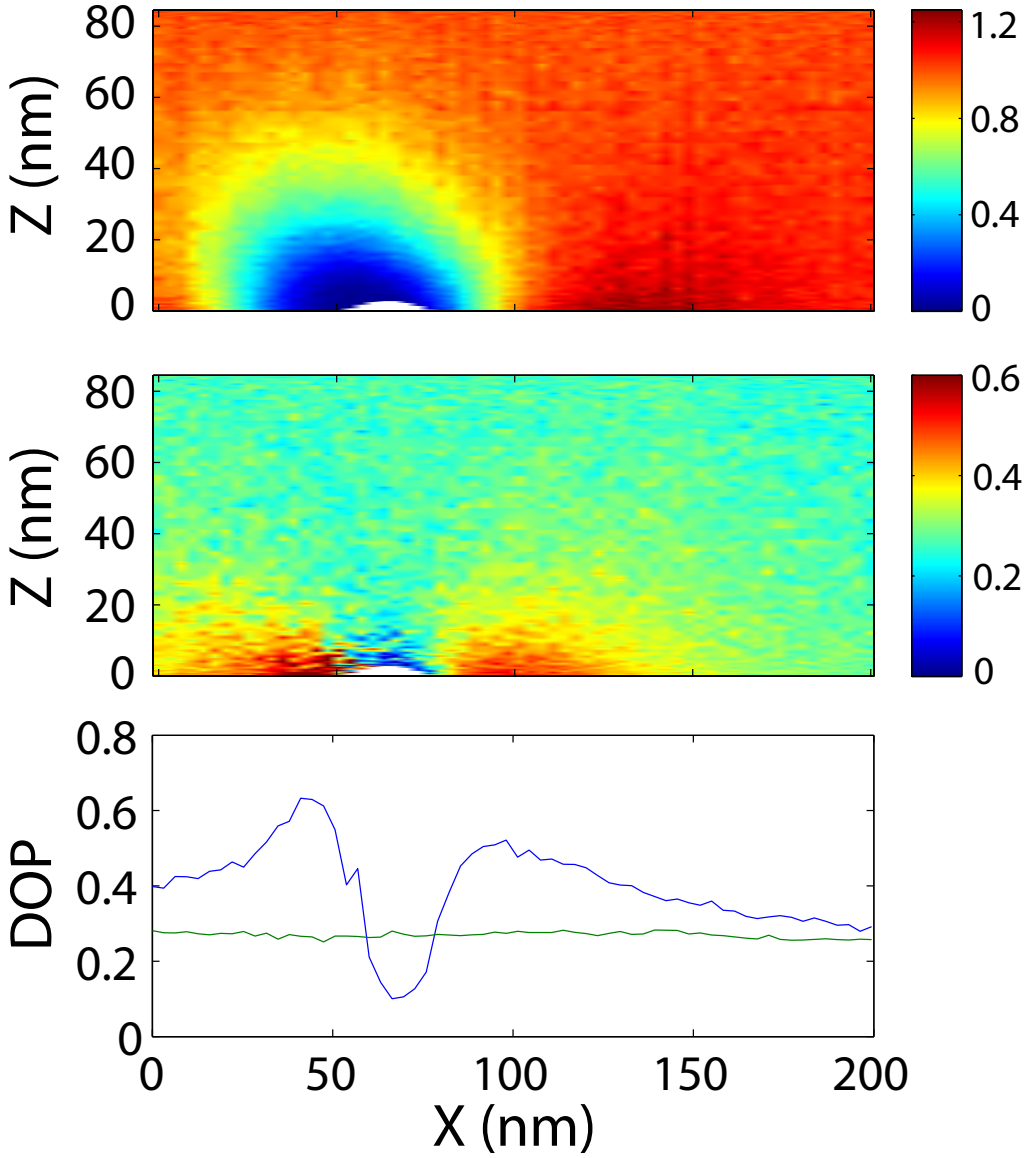

Figure 7.4. X-Z slice using gold tip. (a) The sum of the signal from the two different polarization channels normalized to the far-field. The color scale represents the value of the normalized signal.(b) The DOP values show strong dependency on the exact tip position with respect to the QD. In this case, the color scale represent the DOP value. For both panels (a) and (b) the AFM topography is depicted in white. (c) The near-field ($z < 2$ nm) and far-field DOPs value are extracted from panel (b) and plotted in blue and green, respectively, as a function of x, the horizontal position of the tip relative to the QD.

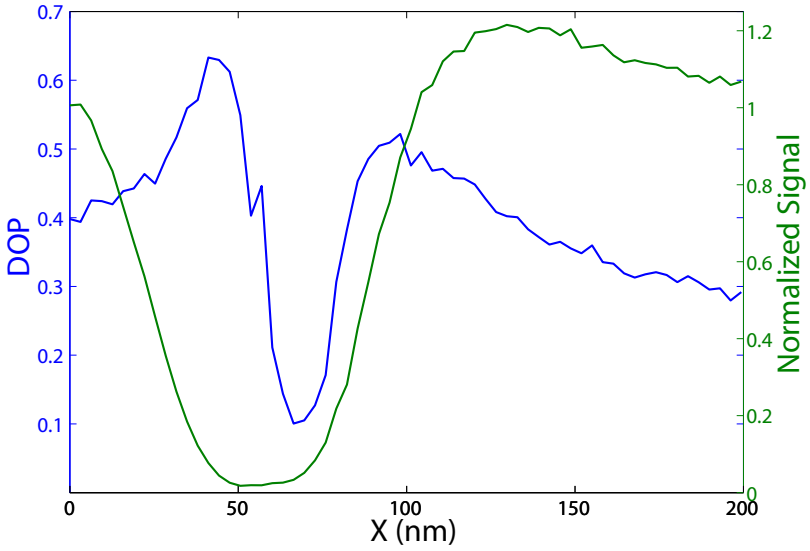

Figure 7.5. Comparison of near-field signal with near-field DOP. The near-field signal (green curve) and near-field DOP (blue curve) do not correlate with each other.

DOP values which depend on the internal state of the QD. As shown in Fig. 7.2, this is not the case. Also, the CNT tip has strong coupling but no change in DOP. We believe that the change in the angular emission is caused by the change of the dielectric environment near the QD as the tip approaches. This is consistent with our observations - gold and silicon result in a large dielectric mismatch and therefore alter the angular emission, while the CNTs are too small to create any significant change.

Another interesting aspect of this effect is the very small vertical tip-QD separation distance at which the reorientation occurs. The changes in DOP values only begin to appear at separation distances of $z \sim 15$ nm for both the gold and the silicon tips. This is a much shorter length scale than previously observed for a metal disk placed above single molecules [19]. The resulting DOP of the QDs also depends on the location of the tip with respect to the QD. For gold tips, when the tip is placed above the QD, the DOP value approaches 0. On the other hand, when the tip is placed on the side of the QD, the DOP value is DOP ~ 0.4. The effect on the polarization when the tip is placed to the side of the QD extends much further than when the tip is approaching from above. Even at lateral separation distance of $x = 50$ nm, the

DOP value still seems to be modified above the far-field DOP (Fig. 7.4b). The peak to the left of the QD in Fig. 7.4 is reproducible and might have to do with a slight asymmetry of the AFM probes.

The CNTs do not modify the angular emission properties. This is an indication that CNT tips can be used as local environment probes with minimal perturbation to the properties of the system. This property of CNTs was already utilized for scattering-NSOM applications [20] and might also be valubale for future sensing applications.

An interesting question which cannot be answered by our data is whether the induced changes are simply a result of placing a dielectric material in the proximity of a single emitter or whether the internal properties of the QD are changed. One possible signature of the latter would be a shift in the emission energy as the tip approaches the QD due to the anisotropic perturbation induced by the tip [16, 21]. The fact that the emission polarization is modified even when the tip is as far as 50 nm to the side of the QD suggests that the internal properties of the QD are not the cause of the effect.

7.5 Conclusion and outlook

We observe a change in the polarization distribution in proximity to near-field probes. This phenomenon strongly depends on the tip-QD distance and position as well as the geometry and composition of the tip. The reorientation effect is reversible and reproducible for all QDs tested. This work, along with previous work, demonstrates easy manipulation of QDs emission properties by using a gold NSOM probe near the QD.

A better understanding of the emission properties of single emitters in the proximity of near-field probes can be achieved by means of 3D numerical simulations. In particular, one can study the changes to the emission intensity and polarization properties of a single dipole emitter placed next to a gold or silicon near-field probe.

7.6 References

[1] H. Gersen et al., Physical Review Letters **85**, 5312 (2000).

[2] T. H. Taminiau, F. D. Stefani, F. B. Segerink, and N. F. van Hulst, Nature Photonics **2**, 234 (2008).

[3] Y. C. Jun, R. Pala, and M. L. Brongersma, Journal of Physical Chemistry C **114**, 7269 (2010).

[4] N. Livneh et al., Nano Letters **11**, 1630 (2011).

[5] H. Aouani et al., Nano Letters **11**, 2400 (2011).

[6] A. G. Curto et al., Science (New York, NY) **329**, 930 (2010).

[7] D. E. Gomez, M. Califano, and P. Mulvaney, Physical Chemistry Chemical Physics **8**, 4989 (2006).

[8] I. L. Medintz, H. T. Uyeda, E. R. Goldman, and H. Mattoussi, Nature Materials **4**, 435 (2005).

[9] X. Michalet, Science (New York, NY) **307**, 538 (2005).

[10] E. Shafran, B. D. Mangum, and J. M. Gerton, Physical Review Letters **107**, 037403 (2011).

[11] A. I. Chizhik, A. M. Chizhik, D. Khoptyar, S. Bär, and A. J. Meixner, Nano Letters **11**, 1131 (2011).

[12] S. A. Empedocles, R. Neuhauser, and M. G. Bawendi, Nature **399**, 126 (1999).

[13] I. Chung, K. Shimizu, and M. Bawendi, Proceedings of The National Academy of Sciences of The United States of America **100**, 405 (2003).

[14] F. Koberling et al., The Journal of Physical Chemistry B **107**, 7463 (2003).

[15] J. Hu et al., Science (New York, NY) **292**, 2060 (2001).

[16] D. V. Talapin et al., Nano Letters **3**, 1677 (2003).

[17] K. Shimizu, W. Woo, B. Fisher, H. Eisler, and M. Bawendi, Physical Review Letters **89**, 117401 (2002).

[18] E. Shafran, B. D. Mangum, and J. M. Gerton, Nano Letters **10**, 4049 (2010).

[19] R. J. Moerland, T. H. Taminiau, L. Novotny, N. F. van Hulst, and L. Kuipers, Nano Letters **8**, 606 (2008).

[20] R. Hillenbrand, F. Keilmann, P. Hanarp, D. Sutherland, and J. Aizpurua, Applied Physics Letters **83**, 368 (2003).

[21] A. Efros and A. Rodina, Physical Review B **47**, 10005 (1993).

APPENDIX A

LIFETIME MEASUREMENTS

Our setup allows us to measure the lifetime as a function of tip-sample distance. The technique is described in details in Sec. 3.4.3. The acquired data can also be constructed into an approach curve (3.4.1). It is useful to normalize the lifetime curve to the far-field lifetime (i.e., τ/τ_0) and compare it to the normalized approach curve (i.e., S_{norm}). The results can than be compared to Eq. 2.39.

We have taken some preliminary data using a 405 nm pulsed laser. Figure A.1 shows the measured approach curve and the normalized lifetime curve for a CNT tip. In this case, the two curves are almost identical. This means that $\kappa(r)\,(1+\Gamma_r'/\Gamma_r) \sim 1$ and therefore, Eq. 2.39 reduces to $S_{\text{norm}} = \tau/\tau_0$. Furthermore, this means that the CNT does not result in any field enhancement (i.e., $\kappa = 1$) and does not modify the radiative rate (i.e., $\Gamma_r' = 0$).

Figure A.2 shows the results for a silicon tip. The lifetime of the QD becomes shorter as the tip gets closer to the QD. The emission intensity still becomes larger as the tip gets closer even though the lifetime decreases. Therefore, $\kappa(r)\,(1+\Gamma_r'/\Gamma_r)$ is monotonically increasing at a faster rate than τ/τ_0 decreases at. The relatively small changes to the lifetime indicate small amount of quenching by the silicon tip.

The results for gold tips are shown in Fig. A.3. The lifetime changes substantially due to strong quenching as the tip gets closer to the QD. Gold does not lead to strong field enhancement at $\lambda_{\text{exc}} = 405$ nm. Therefore, the intensity signal is dominated by the strong quenching. At very short tip-sample distances (< 5 nm), the intensity curve is slightly above the lifetime curve, which means that $\kappa(r)\,(1+\Gamma_r'/\Gamma_r) > 1$.

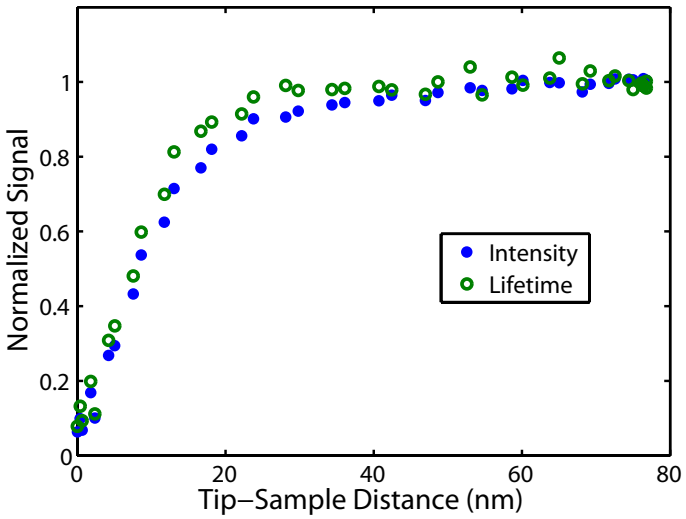

Figure A.1. Emission intensity and lifetime as a function of tip-sample distance for a CNT tip.

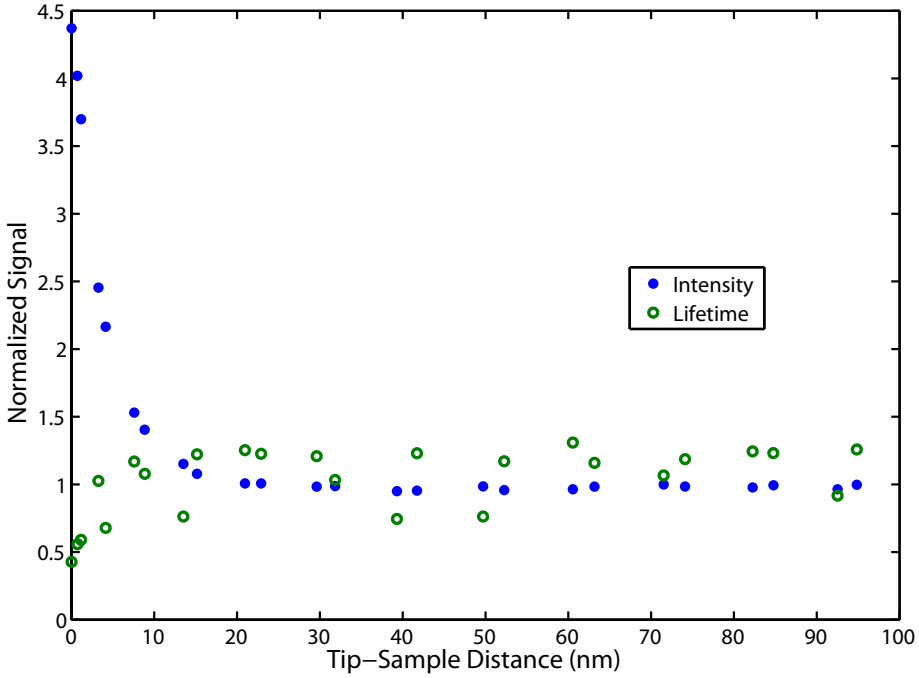

Figure A.2. Emission intensity and lifetime as a function of tip-sample distance for a silicon tip.

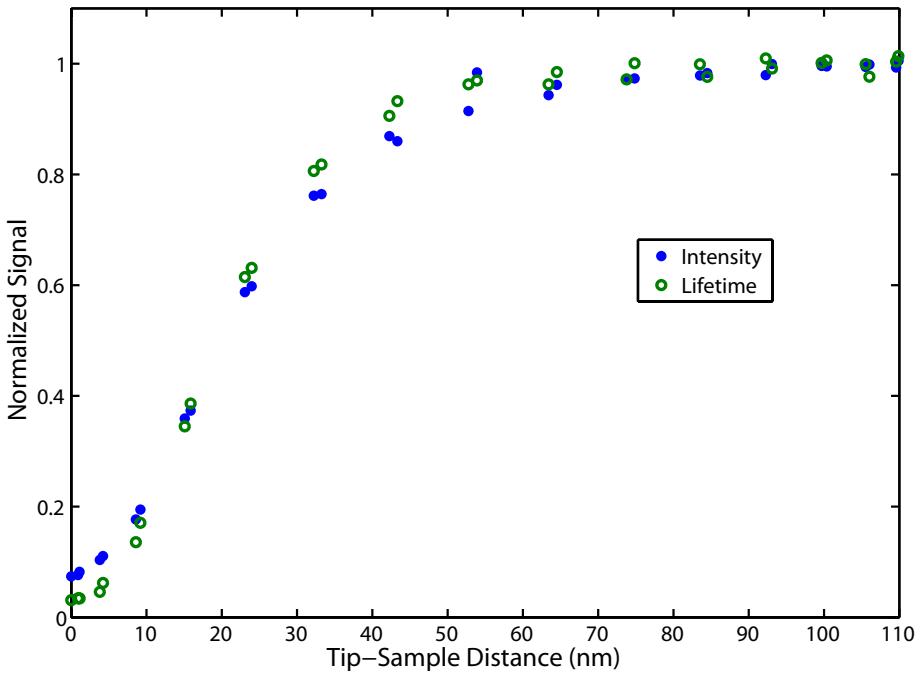

Figure A.3. Emission intensity and lifetime as a function of tip-sample distance for a gold tip.

APPENDIX B

MEASURED DIELECTRIC FUNCTIONS

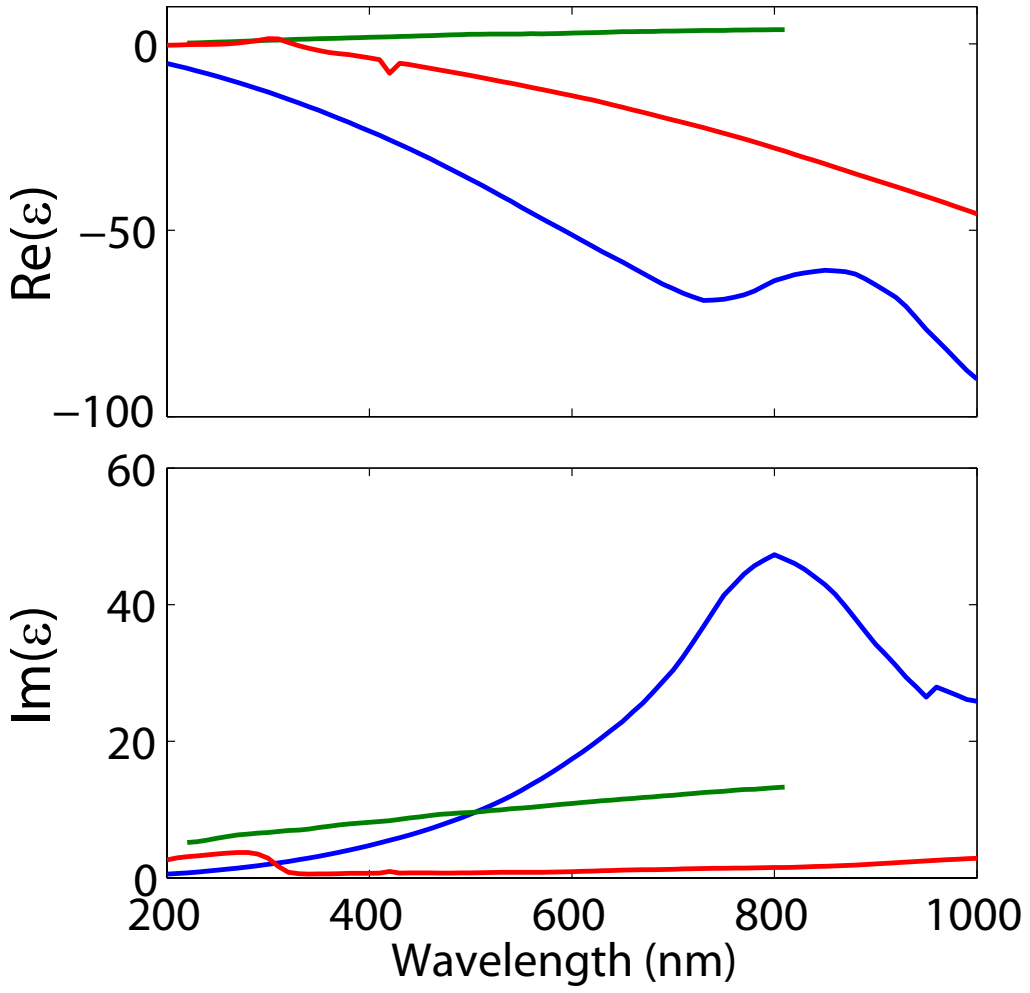

Figure B.1. Dielectric function of metals. Real and imaginary permittivities plotted for aluminum (blue), silver (red), and tungsten (green). Permittivity values are found in the following references: Al and Ag [1], W [2].

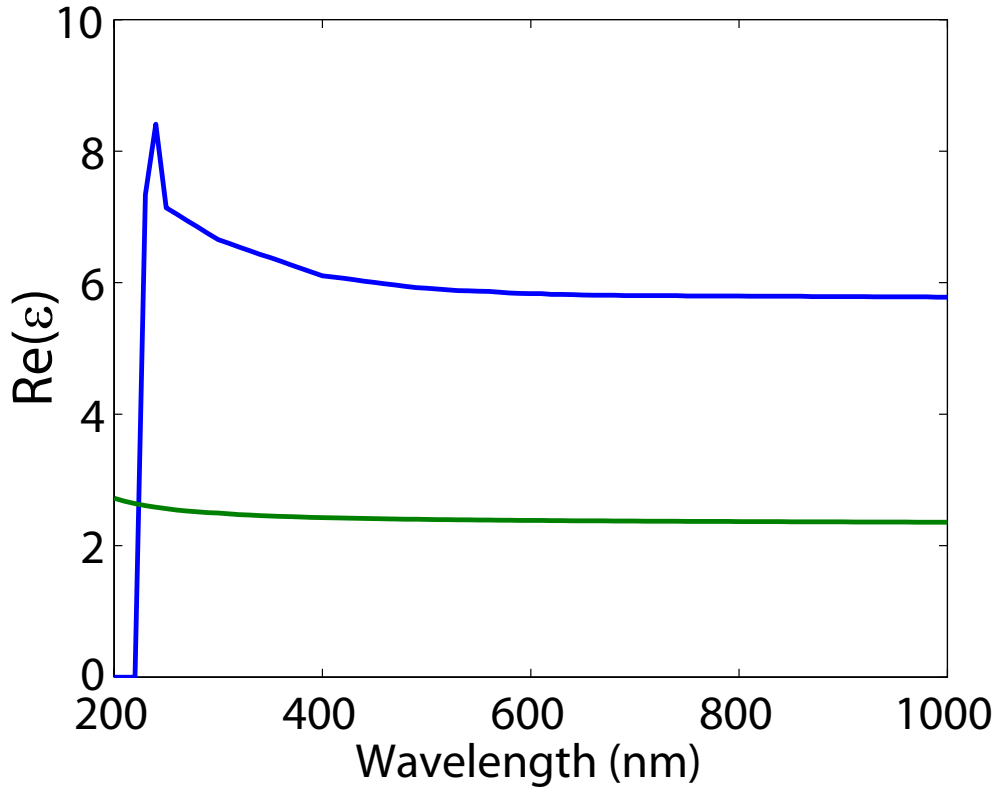

Figure B.2. Dielectric function of dielectric material. Real permittivities plotted for diamond (blue) and S_iO_2 (green). Permittivity values are found in the following references: Diamond [3] and S_iO_2 [1]. The imaginary part for both diamond and S_iO_2 is 0 in the plotted range.

B.1 Refrences

[1] E. D. Palik, *Handbook of Optical Constants of Solids*, Academic Press, Orlando, 1985.

[2] D. Davazoglou, G. Pallis, V. Psycharis, M. Gioti, and S. Logothetidis, Journal of Applied Physics **77**, 6070 (1995).

[3] D. F. Edwards and E. Ochoa, Journal of the Optical Society of America **71**, 607 (1981).

APPENDIX C

SURFACE PLASMONS POLARITONS

Surface plasmons polaritons (SPP) are collective electron oscillations created by coupling the electrons to an electromagnetic wave. Surface plasmons can only occur at the interface between two materials with permittivities ϵ_1 and ϵ_2 that simultaneously satisfy

$$\epsilon_1(\omega) \cdot \epsilon_2(\omega) < 0 \tag{C.1}$$

$$\epsilon_1(\omega) + \epsilon_2(\omega) < 0 \tag{C.2}$$

As discussed in Sec. 2.1, metals typically possess a large negative dielectric function at optical frequencies. Therefore, the conditions to create a SPP from equations C.1 and C.2 are typically satisfied for a dielectric-metal interface. Only an incident wave that is p-polarized and which conserves the momentum at the interface can be converted to SPP. For s-polarized light, there is no force to drive the electrons in the direction of the interface and therefore SPP cannot be created [1]. Let's consider a p-polarized plane wave incident upon a dielectric-metal interface (at z=0) which satisfies the conditions for a SPP. The wavevector of the incident light has components in the x and z directions. The solution to Maxwell equations after matching the appropriate boundary conditions at the interface result in the following wavevectors:

$$k_x^2 = \frac{\epsilon_1 \epsilon_2}{\epsilon_1 + \epsilon_2} k^2 \tag{C.3}$$

$$k_{i,z}^2 = \frac{\epsilon_i^2}{\epsilon_1 + \epsilon_2} k^2 \tag{C.4}$$

where k_x is the wavevector of the SPP along x and $k_{i,z}$ is the wavevector along z with i denoting the medium. The wavevector in the z-axis is always imaginary, and

therefore, the coupled field at the interface results in an exponentially decaying field away from the interface with a stronger confinement in the metallic medium. The prorogation distance of the plasmon on the surface depends on the imaginary part of the metal's dielectric function. For gold at 633 nm, the prorogation of the SPP is $\sim 10\mu$m [1]. The field intensity at the interface may be enhanced by more than an order of magnitude in comparison to the incident field [2].

The requirement for momentum conservation makes it difficult to excite an SPP. There are a few possible configurations to achieve momentum matching. One possibility is to place a single molecule close enough to a dielectric-metal interface. The near-field emission of the molecule can then excite a SPP. It this context, it has also been suggested by numerical simulations that a single molecule's emission can be converted to a SPP on the surface of an AFM tip [3].

Plasmons and surface plasmons have been studied extensively and more details can be found in a variety of sources [1, 2, 4–7].

C.1 References

[1] L. Novotny and B. Hecht, *Principles of Nano-Optics*, Cambridge University Press, Cambridge, 2006.

[2] A. V. Zayats and I. I. Smolyaninov, Journal of Optics A-Pure and Applied Optics **5** (2003).

[3] N. A. Issa and R. Guckenberger, Optics Express **15**, 12131 (2007).

[4] J. D. Jackson, *Classical Electrodynamics*, John Wiley and Sons, Hoboken, third edition, 1999.

[5] C. Kittel, *Introduction to Solid State Physics*, John Wiley & Sons, Hoboken, N.J., eigth edition, 2005.

[6] W. L. Barnes, A. Dereux, and T. W. Ebbesen, Nature **424**, 824 (2003).

[7] S. A. Maier and H. A. Atwater, Journal of Applied Physics **98** (2005).

APPENDIX D

ELECTRIC FIELD AT THE FOCUS

The field components at the focus of a microscope objective can be calculated for radially and azimuthally polarized incident light using Ref. [1]. Figure D.1 is a summary of the results. For these calculations, it is assumed that the beam waist perfectly fills the back aperture of the objective, NA = 1.4, n = 1.518 and $\lambda = 543$nm. The upper three images are the x, y and z components for radially polarized light. The gray scale is the same for all three. The vertical component is about 3.26 times larger than the x and y components. The bottom three images are for azimuthally polarized light. There is no vertical components in this case and therefore the bottom right panel represents the total intensity.

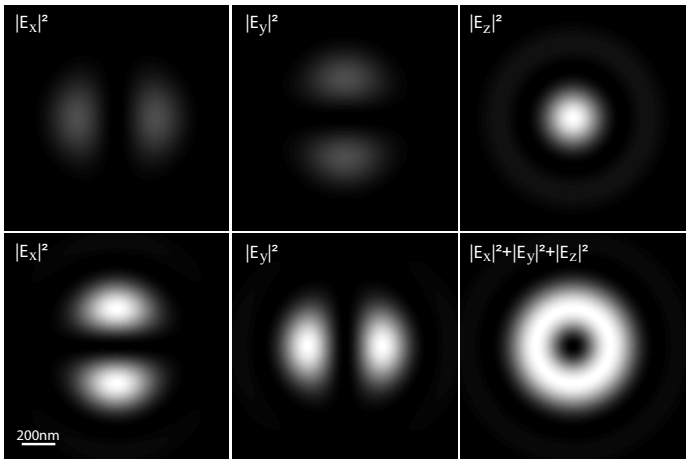

Figure D.1. The electric field components at the focus of a microscope objective. Top three panels are for radially polarized incidence light. The vertical component is 3.26 times greater than the x and y components. The bottom three panels display the results for an azimuthally polarized incidence light. In this case there is no vertical component.

D.1 References

[1] L. Novotny and B. Hecht, *Principles of Nano-Optics*, University Press, Cambridge, 2006.

APPENDIX E

DEFLECTION SIGNAL

To sense the forces on the AFM cantilever, a laser is reflected off the back of the cantilever and is then detected by a quadrant photodiode. The quadrant photodiode is divided into four independent segments (A,B,C and D in Fig. E.1). Each segment outputs a voltage signal that is proportional to the detected light intensity. As the cantilever bends, the laser spot moves on the quad photodiode and the ratio between the signals on the different segments is changed. This process is illustrated in Fig. E.1.

The deflection signal measures the difference between the upper and bottom halves of the photodiode and is defined as

$$V_{\mathrm{Def}} = (V_A + V_B) - (V_C + V_D) \tag{E.1}$$

Any vertical movement of the tip will result in a change in the deflection signal

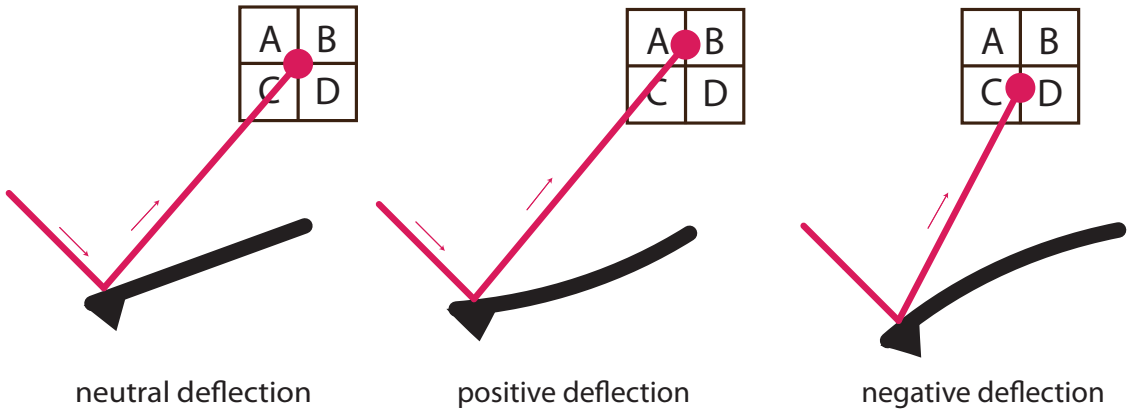

Figure E.1. Illustration of the AFM deflection signal.

and therefore this is the most important AFM signal. It is used as the error signal in the Z feedback loop and is also used to synchronize the AFMs height with the photon signal in NSOM.

When the tip is operating in tapping mode, the deflection signal varies sinusoidally. The deflection signal is then put into the AFM control box where a lock-in is used to find its amplitude and phase shift. The measured lock-in amplitude is proportional to the cantilever's actual oscillation amplitude. It is possible to convert the amplitude of the deflection signal from voltage to spatial amplitude units (nm). This calibration procedure is called InvOLS; details are explained in the AFM manual.

It is also possible to measure the lateral movement of the tip using

$$V_{\text{Lateral}} = (V_A + V_C) - (V_B + V_D) \tag{E.2}$$

Usually the tip will only experience a measurable lateral shift when dragging the tip on a surface (i.e., contact mode imaging). In AC mode, the contact between the sample and the tip are only intermittent and the lateral forces on the tip are negligible.

APPENDIX F

TIME STAMPING CIRCUIT

The AFM's deflection signal is calculated by the difference between the upper and lower part of the quad detector. Therefore, it reflects the actual vertical motion of the tip. The signal itself is an analog signal and needs to be converted to a TTL signal in order to be compatible for time stamping with a data acquisition card (NI USB-6210 or PCIe-6341). Notice that this is the best method if the tips motion is harmonic. When imaging in air, the motion is almost perfectly harmonic. However, in liquid the tip oscillation deviates quite a lot from a harmonic motion. For non-sinusoidal operating conditions, the analog deflection signal can be recorded with a ADC.

There are a few steps which are important in the circuit:

1. The sine wave is amplified in three stages using AD8002 op amps.This is done to account for the large variations in sine-wave amplitude that can be used in the system: the output is saturated at 5 volts regardless of the input signal.

2. The amplified signal is converted to a square wave using a fast discriminator (AD8561).

3. A transistor is used to elevate the output voltage to the desired value.

4. The final output must be buffered so that it is not pulled down. This is done with a $25 - \Omega$ octal buffer/driver (SN6425244NT).

The complete circuit diagram is shown in Figure F.1

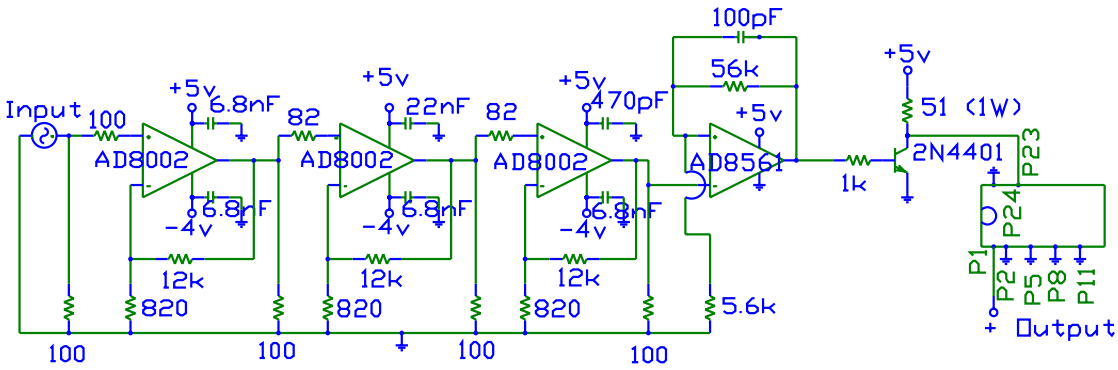

Figure F.1. Time stamping circuit diagram for tip-oscillations. The circuit converts a sinusoidal deflection signal into a 0-5 V square wave. Note: place 1nF capacitors between +5V supplies and ground.

APPENDIX G

CNT GROWTH

This is the protocol used to grow nanotubes:

G.1 Si Wafer Treatment

1. Cut Si wafer into four 9x13 mm + one 6x6 mm rectangles.
2. Use nitrogen to blow off any large dust particles.
3. Number the wafer (the 6x6 wafer should be I).
4. Place in shallow glass dish and treat with piranha.
    - Piranha: pour 30 mL H_2SO_4 into dish with wafers. Add 10 mL H_2O_2 and cover with a larger glass dish. Let sit for 1 hour.
5. Rinse wafers 2x in ultra-pure H_2O.
6. Sonicate wafers in ultra-pure H_2O for 20 minutes.

G.2 Catalyst

1. Sonicate both catalyst bottles with ultra-pure H_2O for 20+ minutes.
2. Rinse with electronic-grade isopropanol.
3. Ferric nitrate: measure out 250 mg and dissolve completely in 25 ml IPA.
4. Dilution: 25 μL of mother solution into 25 mL IPA.
5. Spin coat the four 9x13 mm wafers: 4 sets of 4 drops (50 μL each set) at 3000 rpm.
6. Coat the 6x6 wafer with catalyst solution (1 drop) but do not spin-dry.

G.3 Baking

1. Clean quartz tube with micro-90 and acetone. Dry with heat gun.
2. Clean nanotube holder with acetone
3. Clean thermocouple with acetone.
4. Load wafers into holder with 6x6 wafer furthest upstream (lying flat). The four larger wafers should be vertically placed in slots, all facing downstream.
5. Assemble gas-flow system. Set the flow meter:
   - Argon: 100 (440 mL/min).
   - Hydrogen: 50 (125 mL/min).
   - Methane: 42 (1080 mL/min).
6. Stuff furnace ends with Fiberflax insulation. Use fans to protect o-rings.
7. Flush system with aragon for 15 minutes.
8. Add hydrogen and heat furnace to 900 °C using "Set Point" dial.
9. Hold at desired temperature (control and read TCs should read $\sim$ 922-923 °C) for 15 minutes with the same flow rates.
10. Turn off hydrogen and flush with argon for 5 minutes.
11. Turn on methane and hydrogen simultaneously and then immediately turn off argon flow. Growth time 7 minutes (growth time may vary between 30 seconds and 10 minutes).
12. When growth is complete, turn argon on and methane off simultaneously.
13. Flush system with argon and hydrogen for 5 minutes, holding temperature constant.

14. Cooldown: dial “Set point” to zero. Unplug controller. Remove insulation from both ends of the furnace. Blow cool air from right end of furnace until both thermocouples read <150 °C. Turn off hydrogen.